

## ABSTRACT

Title of Dissertation:           **CONFINED PHOTOTHERMAL HEATING  
OF NANOPARTICLE DISPLAYED  
BIOMATERIALS**

David Hastman, Doctor of Philosophy, 2021

Dissertation directed by:       **Dr. Igor L. Medintz, U.S. Naval Research  
Laboratory**

Professor Helim Aranda-Espinoza, Fischell  
Department of Bioengineering

Controlling the temperature of biological systems has long been utilized as a tool for regulating their subsequent biological activity. Recently, photothermal heating of gold nanoparticles (AuNPs) has emerged as an efficient and remote method to heat proximal biological materials. Moreover, this technique has tremendous potential for controlling biological systems at the subcellular level, as specific components within the system can be heated while the larger system remains unaffected. While the utility of photothermal heating has significantly advanced through the optimization of AuNP size, shape, and composition, the choice of incident light source has largely been unexplored. One of the more interesting excitation sources is a femtosecond (fs) pulsed laser, as the subsequent temperature increase lasts for only a few nanoseconds and is confined to the nanoscale. However, it is not yet clear how biological materials respond to these nanoscale spatiotemporal temperature increases. In this dissertation, we utilize

fs laser pulse excitation to locally heat biological materials displayed on the surface of AuNPs in order to understand the corresponding heating profiles and, in turn, interpret how this can be used to modulate biological activity. Due to its unique temperature sensitive hybridization properties, we exploit double-stranded deoxyribonucleic acid (dsDNA) as our prototypical biological material and demonstrate precise control over the rate of dsDNA denaturation by controlling the laser pulse radiant exposure, dsDNA melting temperature, and the distance between the dsDNA and AuNP surface. The rate of dsDNA denaturation was well fit by a modified dissociation equation from which a “sensed” temperature value was obtained. Evaluating this sensed temperature in the context of the theoretical temperatures revealed that the ultra-high temperatures near the AuNP surface play a significant role in denaturation. Additionally, we evaluate this technique as a means to enhance enzyme activity and report that enhancement is governed by the laser repetition rate, pulse width, and the enzyme’s inherent turnover number. Overall, we demonstrate that the confined and nanosecond duration temperature increase achievable around AuNPs with fs laser pulse excitation can be used to precisely control biological function and establish important design considerations for coupling this technique to more complex biological systems.

CONFINED PHOTOTHERMAL HEATING OF NANOPARTICLE DISPLAYED  
BIOMATERIALS

by

David Hastman

Dissertation submitted to the Faculty of the Graduate School of the  
University of Maryland, College Park, in partial fulfillment  
of the requirements for the degree of  
Doctorate of Philosophy  
2021

Advisory Committee:

Dr. Igor L. Medintz, Co-chair

Dr. Helim Aranda-Espinoza, Co-chair

Dr. Sebastián A. Díaz

Dr. Huang-Chiao Huang

Dr. Giuliano Scarcelli

Dr. Paul J. Paukstelis, Dean's Representative

© Copyright by  
David Hastman  
2021

## Table of Contents

Table of Contents .....	ii
List of Tables .....	iv
List of Figures .....	v
Chapter 1: Introduction .....	1
1.1 Optical heating of AuNPs .....	3
1.1.1 Introduction.....	3
1.1.2 Types of illumination for optical heating of AuNPs.....	5
1.1.3 Fs laser pulse optical heating of AuNPs .....	7
1.1.4 Biological response to fs laser pulse optical heating of AuNPs .....	12
1.2 Overview of dissertation .....	13
Chapter 2: Using ultrashort laser pulses to release oligonucleotides from the surface of gold nanoparticles° .....	18
2.1 Introduction.....	18
2.2 DNA-AuNP conjugates .....	20
2.2.1 DNA composition and structure .....	20
2.2.2 DNA modification for AuNP attachment .....	22
2.2.3 Mechanisms of DNA photothermal release on the surface of AuNPs.....	24
2.3 Ultrashort laser pulse excitation of dsDNA-AuNP conjugates.....	26
2.3.1 Fs laser pulse excitation of dsDNA-AuNP conjugates .....	26
2.3.2 Ns laser pulse excitation of dsDNA-AuNP conjugates .....	30
2.4 Conclusions .....	32
Chapter 3: Femtosecond Laser Pulse Excitation of DNA-Labeled Gold Nanoparticles: Establishing a Quantitative Local Nanothermometer for Biological Applications* ...	34
3.1 Introduction.....	34
3.2 Results and discussion .....	37
3.2.1 System design and characterization .....	37
3.2.2 Determination of DNA denaturation profiles using bulk solution heating	43
3.2.3 Femtosecond laser pulse heating for DNA release .....	45
3.2.4 Quantification of locally sensed temperature .....	57
3.3 Conclusions.....	65
3.4 Materials and methods .....	67
Chapter 4: Mechanistic Understanding of DNA Denaturation in Nanoscale Thermal Gradients Created by Femtosecond Excitation of Gold Nanoparticles# .....	72
4.2 Results and discussion .....	75
4.2.1 System design and local temperature evaluation .....	75
4.2.2 dsDNA denaturation during fs-laser pulse heating of AuNPs .....	81
4.2.3 Molecular dynamics simulations of dsDNA denaturation.....	87
4.2.4 Discussion .....	93

4.3 Conclusions .....	95
4.4 Materials and methods .....	97
Chapter 5: Understanding Femtosecond Pulse Excitation of Gold Nanoparticles for the Potential Thermal Enhancement of Surface Bound Enzymes .....	102
5.1 Introduction .....	102
5.2 Fs laser pulse excitation of AuNPs for AP enhancement .....	105
5.2.1 System design and characterization .....	105
5.2.2 Fs laser pulse irradiation of AP-AuNP .....	109
5.2.3 Fs laser pulse irradiation of AP displayed on gold nanorods.....	112
5.3 Expected enzyme enhancement during fs laser pulse heating of AuNPs .....	114
5.4 Conclusions .....	119
Chapter 6: Peptide nucleic acids as a selective and highly efficient alternative for conjugating quantum dots to DNA nanostructures* .....	121
6.1 Introduction .....	121
6.2 Results and discussion .....	124
6.2.1 Peptide-PNAs and QD conjugation .....	124
6.2.2 QD-peptide-PNA binding to DNA origami .....	129
6.3 Conclusions .....	139
6.4 Materials and methods .....	140
Chapter 7: Conclusions .....	147
Permissions .....	151
Bibliography .....	172

## List of Tables

<b>Table 2.1:</b> Examples of ultrashort laser pulse excitation of AuNPs for DNA release.	30
<b>Table 3.1:</b> Physicochemical properties of the DNA strands	39
<b>Table 3.2:</b> Probe DNA release rates	55
<b>Table 3.3:</b> Parameters used for data fitting with the modified DNA dissociation equation.	62
<b>Table 3.4:</b> 5Quantification of local temperature around AuNP after photothermal heating event at different laser pulse radiant exposures	64
<b>Table 4.1:</b> DNA sequence information and dsDNA domain locations.	76
<b>Table 4.2:</b> Quantification of local temperature around dsDNA after femtosecond-laser pulse excitation	84
<b>Table 6.1:</b> Peptide-PNA and Peptide-DNA properties.	126
<b>Table 6.2:</b> DLS and zeta potential of QD:peptide-PNA conjugates.	129

## List of Figures

<b>Figure 1.1:</b> Absorbance spectra and transmission electron microscopy images of of various diameter AuNPs .....	4
<b>Figure 1.2:</b> AuNP light absorption and sequence of events that lead to local environment heating.....	8
<b>Figure 1.3:</b> Temperature profile of a 50 nm diameter AuNP under cw illumination or after a single fs pluse.....	12
<b>Figure 2.1:</b> DNA structure and melting temperature .....	21
<b>Figure 2.2:</b> Schematic of a dsDNA-AuNP conjugate and photothermal release mechanisms.....	24
<b>Figure 2.3:</b> Transient bleaching of DNA-modified AuNPs. ....	27
<b>Figure 2.4:</b> DNA photothermal release on the surface of AuNS .....	28
<b>Figure 3.1:</b> Schematic and component characterization of AuNP-dsDNA nanothermometer. ....	36
<b>Figure 3.2:</b> Temperature dependence of OG488 fluorescence .....	40
<b>Figure 3.3:</b> Standardization curves converting the fluorescence of OG488 labeled probe DNA to concentration of probe DNA.....	42
<b>Figure 3.4:</b> dsDNA denaturation in solution and on AuNP from bulk heating assays .....	44
<b>Figure 3.5:</b> Bulk solution temperatures measured during irradiation at a 14.1 J/m <sup>2</sup> pulse radiant exposure.....	47
<b>Figure 3.6:</b> Absorbance of 13 pM dsDNA-AuNP conjugate (with Probe55) before and after irradiation at 14.1 J/m <sup>2</sup> for 100 seconds. ....	48
<b>Figure 3.7:</b> Probe65 release profile at 14.1 J/m <sup>2</sup> .....	49
<b>Figure 3.8:</b> Release profile for ATTO550 template strand at 14.1 J/m <sup>2</sup> .....	50
<b>Figure 3.9:</b> : Probe DNA release profiles at 14.1 J/m <sup>2</sup> .....	52



<b>Figure 3.10:</b> Probe DNA release as a function of pulse number and pulse radiant exposure. ....	54
<b>Figure 3.11:</b> Probe DNA release at varying bath temperatures .....	56
<b>Figure 3.12:</b> Curve fitting of Probe DNA release and average temperature determination .....	61
<b>Figure 4.1:</b> Schematic of fs-laser pulse excitation of dsDNA-AuNP .....	74
<b>Figure 4.2:</b> dsDNA melting curves for spacer strands .....	77
<b>Figure 4.3:</b> Representative temperature profiles and 5 ns average temperature determinations .....	80
<b>Figure 4.4:</b> Probe DNA release and sensed temperature comparisons .....	83
<b>Figure 4.5:</b> Delta temperature and average temperature relative variance .....	86
<b>Figure 4.6:</b> Molecular dynamics simulations of dsDNA attached to the gold surface and exposed to pulse heating and continuous heating .....	90
<b>Figure 5.1:</b> Schematic of ns laser pulse inactivation of $\alpha$ -chymotrypsin .....	104
<b>Figure 5.2:</b> Schematic of a 55 nm diameter AuNP displaying AP .....	106
<b>Figure 5.3:</b> Kinetic analysis of AP .....	108
<b>Figure 5.4:</b> Irradiation of AP-AuNP .....	111
<b>Figure 5.5:</b> : Irradiation of AP-AuNR.....	113
<b>Figure 5.6:</b> Percent increase in product formation during ultrafast laser pulse photothermal heating of AuNPs.....	117
<b>Figure 6.1:</b> Peptide-PNA conjugation to QDs .....	125
<b>Figure 6.2:</b> Effects of conjugation on physical properties of QDs.....	128
<b>Figure 6.3:</b> DNA breadboard design and QD immobilization .....	130
<b>Figure 6.4:</b> Capture of a single QD4 on the DNA breadboard .....	132
<b>Figure 6.5:</b> Effects of QD to capture site ratio on capture efficiency .....	133
<b>Figure 6.6:</b> Capture of a single QD8 on the DNA breadboard. ....	134

<b>Figure 6.7:</b> Effects of peptide charge on capture efficiency of QD8 .....	136
<b>Figure 6.8:</b> Peptide-DNA immobilization of QDs on a DNA breadboard with four capture sites.....	138
<b>Figure 6.9:</b> Selective immobilization of QD4 and QD8 on the DNA breadboard...	139

## Chapter 1: Introduction

Coupling colloidal nanoparticles (NPs) to biological materials has emerged as a powerful tool that has enabled researchers to probe and modulate biological systems like never before. This is primarily due to two reasons: 1) the small size of NPs (< 100 nm in at least one dimension) makes them an ideal candidate for interacting with biological materials such as proteins or oligonucleotides, and 2) many NPs possess unique physicochemical properties that are not found in the same material of a larger size. While the properties unique to NPs primarily arise from quantum confinement effects and high surface to volume ratios, the diversity of NPs and their subsequent properties are vast.<sup>1</sup> Depending on the material type, NPs can manifest distinct optical, magnetic, electronic, mechanical and chemical properties. Some of the more prominent NPs are semiconductor quantum dots (QDs) which have size-tunable photoluminescence,<sup>2</sup> noble metal NPs that have localized surface plasmon resonances,<sup>3</sup> and iron oxide NPs displaying superparamagnetism,<sup>4</sup> yet there are copious examples and the list continues to grow. Combining NPs with biological materials allows researchers to make hybrid bionanomaterials, novel materials that make use of the properties of both the NP and biological material. Typically this is done for one of two purposes, to probe/sense biological activity or to modulate/control biological activity. For example, QDs have been utilized in QD-dopamine conjugates as a fluorescent reporter for intercellular pH sensing<sup>5</sup>(probe/sense) and they have also been used as a scaffold to display enzymes in order to provide a catalytic rate enhancement (modulate/control).<sup>6</sup>

One of the more interesting and popular classes of bionanomaterials is the assembly of biological materials on to the surface of a NP.<sup>7</sup> In many cases this is done to provide the NP with additional functionality, *e.g.*, peptides for adhesion to the cellular membrane,<sup>8</sup> DNA for crosslinking with other NPs and forming NP superstructures,<sup>9</sup> and proteins for increased biocompatibility.<sup>10</sup> In contrast, many bionanomaterials utilize the NP properties to provide an additional functionality to the biological material, *e.g.*, QDs for fluorescent tracking/reporting,<sup>11</sup> noble metal NPs for photothermal release,<sup>12</sup> and superparamagnetic iron oxide NPs for magnetic recovery.<sup>13</sup> Regardless of the purpose, the NP acts as a scaffold for the biological material in these systems, placing the biological material in a complex environments. Electrostatic double-layer interactions, Van der Waals forces, steric hindrance, the solid-liquid interface between the NP and solution, and the curvature of the NP are just a few of the what seems to be countless forces and interactions occurring at the nano-bio interface. While deconstructing these interactions within a system is quite challenging, the potential of exploiting them for biophysical processes makes this an intriguing area of research.<sup>14</sup> Not surprisingly, many reports have indicated that the function of biological materials is altered when displayed on a NP surface.<sup>6, 15-16</sup> While the conclusions of these reports are typically system dependent, the change in activity/function is usually attributed to one aspect of the nano-bio interface.

Gold nanoparticles (AuNPs) are one of the most commonly used NPs for biological applications as their synthesis is relatively straightforward, they are biocompatible and their surfaces can be readily modified with biomolecules using functional groups such as thiols, phosphines and amines.<sup>17</sup> AuNPs are typically synthesized through the

reduction of  $\text{HAuCl}_4$  into Au(III) in the presence of a capping ligand.<sup>7</sup> Typically, citrate is used as the reducing agent as it can also serve as the capping ligand and enables the AuNP to be colloidally stable in an aqueous environment.<sup>18</sup> A variety of new synthesis techniques have been utilized to make AuNPs ranging from 1-200 nm in diameter in a countless number of different morphologies such as spherical gold nanoparticles, gold nanorods, gold nanostars and gold nanocages.<sup>19-21</sup> These properties alone have made AuNPs useful for a myriad of applications both *in vitro* and *in vivo*.<sup>17, 22-25</sup> Additionally, as discussed in the next section, AuNPs (and other noble metal NPs) have the innate capability to efficiently generate heat when excited with an external light source.<sup>3</sup>

## ***1.1 Optical heating of AuNPs***

### ***1.1.1 Introduction***

AuNPs are a metal, and as such have free electrons in their conduction band. In bulk, these electrons are free to move about the material, yet for AuNPs the free electrons are confined to the size and shape of the AuNPs.<sup>26</sup> This electron confinement gives way to a localized plasmon, which is a normal mode of collective oscillation of the free electrons contained in a metal NP.<sup>27</sup> A localized plasmon resonance can be excited using a wavelength of light that is larger than the NP size and when the electric field of the incoming light oscillates at a frequency close to the plasmon eigen frequency.<sup>28</sup> The localized plasmon resonance is dependent on the NP size, shape, composition and the refractive index of the surrounding material.<sup>27</sup> An example of the size dependence of the plasmon resonance is shown in Figure 1.1A for spherical AuNPs of various diameters. This strong light-matter interaction gives the AuNP a large

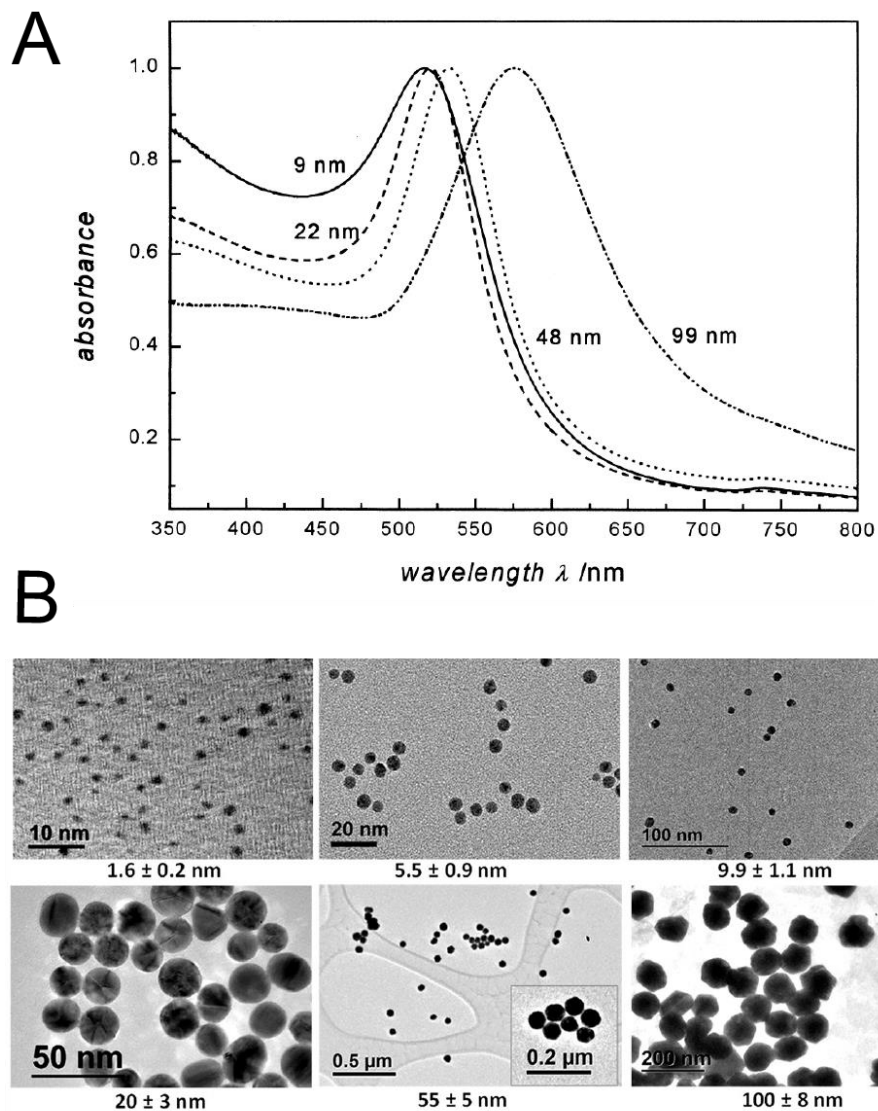


**Figure 1.1:** A) Absorbance spectra of various diameter AuNPs demonstrating the size dependence of the plasmon resonance peak. Reprinted with permission from Stephan Link and Mostafa A. El-Sayed, Size and Temperature Dependence of the Plasmon Absorption of Colloidal Gold Nanoparticles, *Journal of Physical Chemistry B* 1999. Copyright 1999 American Chemical Society. B) Transmission electron microscopy images of various diameter AuNPs. Reprinted with permission from Joyce C. Breger, Eunkeu Oh, Kimihiro Susumu, William P. Klein, Scott A. Walper, Mario G. Ancona, and Igor L. Medintz, Nanoparticle Size Influences Localized Enzymatic Enhancement-A Case Study with Phosphotriesterase, *Bioconjugate Chem.* 2019. Copyright 2019 American Chemical Society.

absorbance cross section at the wavelength corresponding to the localized plasmon resonance and enables the AuNP to absorb a large amount of energy in the form of light. AuNPs can also be excited through interband transitions as they and other noble metals have absorption cross sections here that are comparable with the plasmonic resonance absorption cross section.<sup>29</sup> Irrespective of the excitation mechanism, the absorbed light energy is eventually transferred to the AuNP surroundings in the form of heat.

The ability of AuNPs and other noble metals to efficiently convert light to heat in nanoscale systems has gained much attention over the recent years, and the field has been recently coined “thermoplasmonics”. The ability to externally control (via incident light) a nanoscale heat source has paved ways for thermoplasmonics applications such as protein denaturation,<sup>30</sup> plasmonic photothermal therapy,<sup>25</sup> drug and gene delivery,<sup>31</sup> photoacoustic imaging,<sup>32</sup> nanochemistry,<sup>33</sup> photothermal imaging,<sup>34</sup> and investigating thermal process on the single cell level.<sup>35</sup> As biological processes are almost always temperature dependent, it is no surprise that many groups are actively working to implement these nanoheaters into biological systems.

#### *1.1.2 Types of illumination for optical heating of AuNPs*

Lasers are typically used as the light source for photothermal heating of AuNPs. The laser can be a continuous-wave (CW) laser or a pulsed laser. In a CW laser, a continuous and constant wave of photons illuminates the AuNP. During this type excitation, the AuNP has a constant energy input (the laser) and a constant energy output (heat dissipation into the surrounding environment). As such, photothermal heating of AuNPs under CW irradiation can be modeled as steady-state or equilibrium

heating.<sup>27</sup> In these systems, the temperature increase in the local solution follows a  $1/r$  ( $r$  = NP radius) dependence extending from the NP surface.<sup>36</sup> In this dissertation we will quantify laser illumination using two terms; irradiance and radiant exposure. The irradiance is defined as the radiant power (J/s or W) per unit area incident upon a given surface and is expressed as  $\text{W/m}^2$ .<sup>37</sup> The radiant exposure is defined as the radiant energy per unit area incident upon a given surface and is expressed as  $\text{J/m}^2$ .<sup>37</sup> For a single 50 nm AuNP to increase its surface temperature by  $\sim 10^\circ\text{C}$  using CW excitation, a very high irradiance is needed ( $> 10^8 \text{ W/m}^2$ ).<sup>38</sup> Since such a high irradiance is needed to moderately increase the AuNP surface temperature, CW systems typically rely on collective heating effects to reach temperature increases on the order of tens of degrees. These collective heating effects are achieved by working at a high NP concentrations ( $> 10^{10}$  NPs/ml) and through the  $1/r$  temperature dependence innate to CW excitation.<sup>27, 39</sup> While CW optical heating of AuNPs has shown promise for a variety of biological applications,<sup>25, 40-41</sup> the collective heating effects that are needed for a significant temperature increase (tens of degrees) are present throughout the solution, limiting the application to biological systems where solution heating is desired or can be tolerated.

In contrast to CW lasers, pulsed lasers emit light in pulses of a specific duration (pulse width) at a specific repetition rate. For example a pulsed laser with a 1 ms pulse width and a 1 Hz repetition rate will send out 1 ms duration pulses of light every second. The temperature profile during pulsed optical heating of AuNPs is dependent on both the pulse width and the laser repetition rate.<sup>27</sup> Pulse widths can range from fs to ms and repetition rates can range from below Hz to MHz creating a large parameter space that can be used to tune the temperature profile under pulse irradiation. In this



dissertation we quantify pulse laser illumination using the pulse radiant exposure ( $\text{J}/\text{m}^2$ ) *i.e.* the radiant energy per unit area in a single pulse incident upon a given surface. In the following section, in order to best explain the effects of pulse width and repetition rate, we will take the reader through the physical process of pulse absorption and the subsequent temperature increase for a fs pulse width and 1 kHz repetition rate.

### *1.1.3 Fs laser pulse optical heating of AuNPs*

When a fs pulse of light is absorbed by a AuNP, it can be described by a three-step process.<sup>42</sup> For the purpose of this dissertation, we will briefly summarize these three steps, but a more detailed explanation can be found in Guillaume Baffou's book *Thermoplasmonics*.<sup>27</sup> Additionally, a schematic is provided in Figure 1.2. Initially, the pulse energy is absorbed by the free electron gas of the AuNP, thermalizing the gas into a Fermi-Dirac distribution over a timescale of  $\sim 100$  fs.<sup>42</sup> At this point, the AuNP is not at equilibrium as the electronic temperature of the electron gas has increased, but the gold lattice or phonon (vibration motion in a lattice of atoms) temperature has not yet changed. This leads to the second step where the electronic gas relaxes through internal electron-phonon interactions. For AuNPs greater than 5 nm in diameter and for moderate pulse energies, this time scale is constant and on the order of  $\sim 1.7$  picoseconds.<sup>43</sup> In the third and final step, the gold phonons couple with the phonons in the surrounding environment, transferring energy to the surroundings in the form of heat. This occurs on a longer time scale, typically on the order of 1 ps to 10 ns depending on the AuNP size (larger sizes corresponds to longer times).<sup>44</sup> Because the fs pulse width is much shorter than the timescale for AuNP heating and external heat diffusion, we can assume that no energy is released to the surrounding medium while

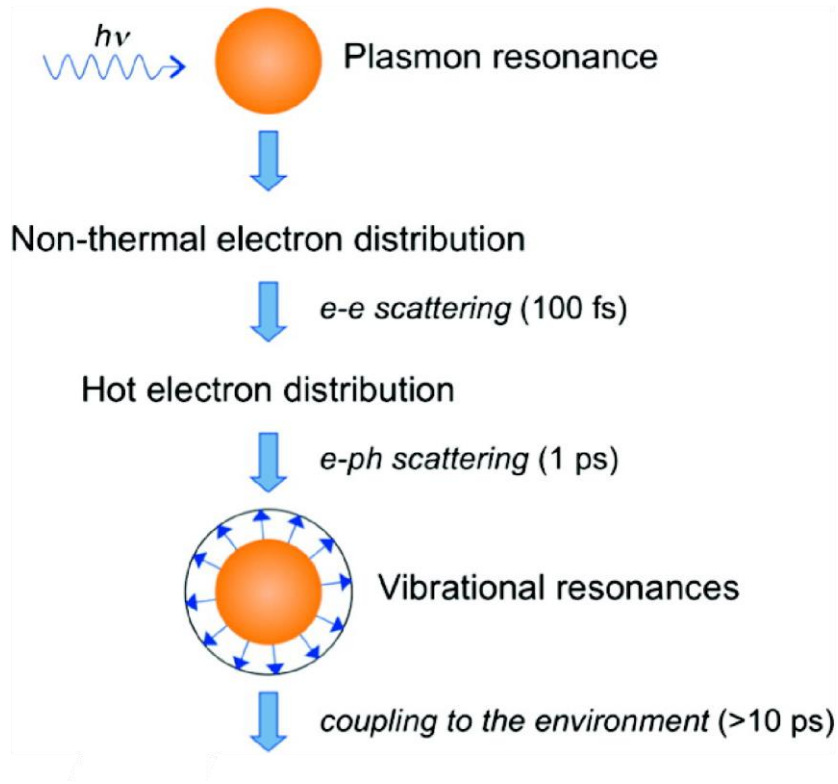


**Figure 1.2:** AuNP light absorption and sequence of events that lead to local environment heating. Reprinted (adapted) with permission from Gregory V. Hartland, Optical Studies of Dynamics in Noble Metal Nanostructures, *Chemical Reviews* 2011. Copyright 2011 American Chemical Society

the pulse energy is being absorbed.<sup>27</sup> This highlights one of the advantages of fs laser pulse excitation: larger (Eq. 1.1) as a rise in temperature  $\delta T$  (K) (Eq. 1.2), where  $\sigma_{abs}$  ( $m^2$ ) is the absorbance cross section of the AuNP,  $F$  ( $J/m^2$ ) is the pulse radiant exposure,  $V$  ( $m^3$ ) is the particle volume,  $\rho_{Au}$  ( $kg/m^3$ ) is the mass density of gold, and  $c_{Au}$  ( $J/kg \cdot K$ ) is the specific heat capacity of gold.<sup>27</sup>

$$\varepsilon_0 = \sigma_{abs} F \quad (\text{Eq. 1.1})$$

$$\varepsilon_0 = V \rho_{Au} c_{Au} \delta T \quad (\text{Eq. 1.2})$$

Combing Eq. 1.1 and 1.2, the theoretical AuNP temperature increase  $\delta T$  can be expressed as:

$$\delta T = \frac{\sigma_{abs} F}{V \rho_{Au} c_{Au}}. \quad (\text{Eq. 1.3})$$

As the particle begins to cool and heat the surrounding environment, we can assume that the NP temperature ( $T_{NP}$ ) remains uniform if the thermal conductivity of the AuNP is much larger than that of the environment.<sup>36</sup> For our work, AuNPs will be in aqueous solution and this assumption is valid as the thermal conductivity of water is  $0.6 \frac{W}{m \cdot K}$  (watts per meter-kelvin) whereas the thermal conductivity of gold is  $317 \frac{W}{m \cdot K}$ .

Thus the temperature  $T$  inside the NP can be expressed as:

$$T(r, t) = T_{NP}(t), \quad \text{for all } t \text{ and for all } r < R, \quad (\text{Eq. 1.4})$$

where  $t$  is time,  $R$  is the AuNP radius and  $r$  is distance from the NP center.<sup>36</sup> The heat diffusion equation outside of the AuNP (assuming a water environment, denoted by the subscript  $w$ ) is:

$$\rho_w c_w \partial_t T(r, t) = \kappa_w \frac{1}{r^2} \partial_r (r^2 \partial_r T(r, t)), \quad \text{for all } r > R, \quad (\text{Eq. 1.5})$$

with the following AuNP-water boundary conditions arising from energy conservation considerations:

$$V \rho_{Au} c_{Au} \frac{dT_{NP}(t)}{dt} = \kappa_w 4\pi R^2 \partial_r T(R, t) = -g 4\pi a^2 \Delta T(t). \quad (\text{Eq. 1.6})$$

where  $\rho_w$  is mass density of water,  $c_w$  is the specific heat capacity of water,  $\kappa_w$  is the thermal conductivity of water and  $g$  ( $W/m^2 \cdot K$ ) is the interface conductivity.<sup>36</sup> This system of equations (Eq. 1.5 and Eq. 1.6) describes the heat transport in the AuNP and

the local aqueous environment and can be solved numerically to determine the temperature profile.<sup>44</sup> Interestingly, the temperature envelope extending from the AuNP surface under fs laser pulse excitation closely follows a  $1/r^3$  distance dependence, whereas the temperature profile during CW excitation follows a  $1/r$  distance dependence.<sup>36</sup> This is a noteworthy distinction as it highlights the temperature confinement afforded through fs laser pulse optical heating of AuNPs. While this is the case for a single AuNP, collective heating effects can still dominate the local temperature increasing during fs laser pulse excitation if high enough AuNP concentrations are used. To determine if confined heating is occurring during fs laser pulsed excitation of AuNPs, the confinement number  $\eta^{\text{ext}}$  can be calculated:<sup>27</sup>

$$\eta^{\text{ext}} = \frac{\langle r \rangle}{f * \tau_{\text{NP}} * R * N^{2/3}} \quad (\text{Eq. 1.7})$$

where  $\langle r \rangle$  is the mean inter-particle distance,  $f$  is the laser repetition rate,  $\tau_{\text{NP}}$  is the characteristic AuNP cooling time,  $R$  is the AuNP radius and  $N$  is the number of particles in the system. When  $\eta^{\text{ext}} \gg 1$ , the AuNP is said to be in a confinement regime (no collective heating effects *i.e.*, the heating from other AuNPs in solution can be ignored).

While the above equations describe the physical process of AuNP excitation from a single fs pulse, it does not describe the process for multiple pulses. To understand the effect of multiple pulses we examine the characteristic cooling time of the AuNP (1 ps to 10 ns) in the context of the laser repetition rate. If we assume a 10 ns characteristic cooling time, that means that after the fs pulse, it takes  $\sim 10$  ns for the AuNP to return to baseline temperature. Using a repetition rate of 1 kHz (1 pulse is absorbed by the AuNP every ms), means that that AuNP is “hot” for  $\sim 10$  ns then returns

to at baseline temperature for over 999  $\mu\text{s}$  before the next pulse arrives. As the repetition rate is increased, the AuNP has less time at baseline temperature between pulses. At high enough repetition rates (depending on the AuNP size) the AuNP may not have time to cool between successive pulses and heat will accumulate in the system.

The above description holds for fs pulse laser excitation and AuNPs of moderate size ( $\sim 15\text{-}80\text{ nm}$ ).<sup>27</sup> As the pulse duration is increased by orders of magnitude (ps, ns, ms) the heating profile becomes progressively more like the steady state heating observed in CW irradiation. Using fs laser pulse excitation to optically heat AuNPs has a few key differences compared to that of CW heating. Firstly, the temperature increase under fs laser pulse excitation is much larger than that of CW excitation for a given average irradiance (Figure 1.3A). For fs laser pulse irradiation, local temperature increases of over  $100\text{ }^{\circ}\text{C}$  are easily achievable using  $\sim 30\text{-}100\text{ nm}$  diameter AuNPs with even moderate pulse radiant exposures ( $\sim 7\text{ J/m}^2$ ). In contrast, CW excitation requires collective heating or extremely high irradiance values of  $>10^8\text{ W/m}^2$  to achieve these temperatures. Second, as seen in Figure 1.3B the temperature increase that can be generated around an AuNP through fs laser pulse excitation can be much more spatially confined on the nanoscale than that of CW excitation ( $1/r^3$  to  $1/r$ ). Finally, the duration of the temperature increase from fs laser pulse optical heating is on the order of ns (Figure 1.3A). Heating on this timescale is not realizable through other methods, and as such it is not clear how biological molecules will respond to these ns temperature increases.

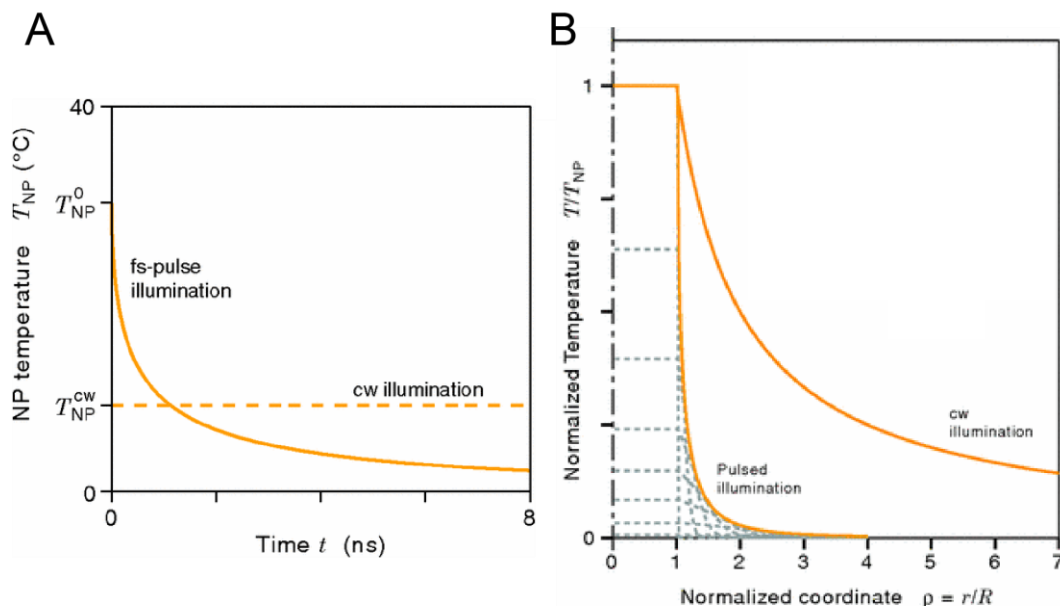


**Figure 1.3:** Time dependence of a 50 nm diameter AuNP temperature increase under cw illumination or after a single fs pulse. The average irradiance for each laser system is  $0.1 \text{ mW}/\mu\text{m}^2$ .  $T_{NP}^0$  is the initial (maximum) AuNP temperature reached after fs pulse absorption.  $T_{NP}^{cw}$  is the NP temperature during cw illumination. B) Temperature profile of AuNP and local environment during cw and fs pulse illumination. The y-axis is normalized by the AuNP temperature and the x-axis by the AuNP radius. Reprinted with permission from Guillaume Baffou and Hervé Rigneault, Femtosecond-pulsed optical heating of gold nanoparticles. *Physical Review B* 2011, 84 (3), 035415. Copyright 2011 American Physical Society.

#### 1.1.4 Biological response to fs laser pulse optical heating of AuNPs

While the theoretical temperature profiles generated from fs laser pulse optical heating of AuNPs are well understood, the application of this technique to biological systems is wanting. Only a few reports have demonstrated using ns or less pulse widths for optical heating of biological materials and even less have utilized fs pulses.<sup>12, 27, 45-50</sup> Most of the work to date with these systems has focused on the release of oligonucleotides from the surface of AuNPs.<sup>12, 48, 50</sup> A few other reports have utilized

this heating technique for the denaturation of proteins.<sup>47, 51</sup> Most of the earlier reports are proof of concept studies, typically displaying a binary response in the system (*e.g.*, DNA release, no DNA release) and demonstrating that no bulk heating occurs. Additionally, many of these reports use high pulse radiant exposures that generate nanobubbles or cause unwanted non-thermal effects such as hot electron ejection.<sup>12, 49</sup> While these effects are desired for many applications, they complicate extracting the thermally induced behavior in these systems and are considered unwanted effects in the context of this work. What is still not clear is how these unique temperature profiles can be used to control biological systems. Although it has been demonstrated that the temperature increase can be tuned to a biological relevant range, it is not yet understood how the steep temperature gradient and ns heating duration will affect the stability and function of biological materials.

## ***1.2 Overview of dissertation***

The scope of this dissertation is to develop a better understanding of how fs laser pulse optical heating of AuNPs can be used control the activity of attached biological materials. To do so, we will generate biological relevant temperature increases (up to 100 °C) that are said to be spatially confined to individual AuNPs. Additionally, we will operate in temporally confined regime, so that AuNPs return to baseline temperature between successive pulses of light. By working in these conditions, we generate a highly localized temperature increase that last for only a few ns. In the context of these unique temperature profiles, the overarching goals of the dissertation are to: 1) probe the kinetic response of biological materials during heating, 2) access

the level of precision and control afforded over biological activity, and 3) understand the relationship between the heating profile and the biological response.

To achieve these goals, we utilized a prototypical biological material, DNA. DNA was chosen as it can be designed to denature over a wide range of temperatures,<sup>16</sup> can be easily conjugated to AuNPs,<sup>52</sup> and previous studies have already demonstrated the feasibility of DNA melting through fs laser pulse optical heating of AuNPs.<sup>12</sup> Furthermore, DNA can be programmed to respond to distinct temperature thresholds and through monitoring the DNA response the local temperature can indirectly be measured. In Chapter 2 we provide a background of the physical properties of DNA as well as a review of the previous work utilizing this technique for DNA melting.

In Chapter 3, we build upon the previous work in the field and examine the denaturation rate of DNA on the surface of 55 nm diameter AuNPs in response to fs laser pulse heating. We investigated DNAs of different melting temperatures and found that the rate of DNA release is dependent on both the DNA melting temperature as well as the pulse radiant exposure. To further control the DNA release rate we varied the bulk solution temperature during irradiation. Using these three control levers the rate of DNA release could be varied by more than three fold. Of perhaps even more interest, we present a modified DNA dissociation equation that allowed us to extract a “sensed” temperature parameter and use our system as a quantitative local nanothermometer. By comparing the sensed temperature with the theoretical temperature profile of the AuNP, we hypothesized that the steep temperature gradient near the AuNP surface plays a significant role in the DNA release.



In Chapter 4 we designed a new system aimed at investigating the positional variance of the DNA with respect to the AuNP surface. As the temperature envelope follows a  $1/r^3$  distance dependence, the distance between the AuNP and DNA is a critical parameter in these systems. Here we systematically varied the distance between the DNA and the AuNP surface in order to determine the influence of the peak or maximum temperatures near the AuNP surface on DNA melting. In doing so, we found that when the DNA is closer to the AuNP surface, it is exposed to ultra-high temperatures ( $> 100\text{ }^{\circ}\text{C}$ ) and releases at a rate higher than what is theoretically predicted. Furthermore, we demonstrated that the rate of DNA release can be modified by up to  $30 \pm 2\%$  by shifting the DNA position by as little as 1.1 nm. To better understand this system we collaborated with Dr. Parth Chaturvedi and Prof. Lela Vuković from the University of Texas El Paso. They performed detailed molecular dynamic (MD) simulations of DNA melting on a gold surface from a ns heat pulse, mimicking the fs laser pulse optical heating in our system. From their MD simulations and our experimental findings, we report that DNA dehybridization in our system likely occurs through a stochastic single-pulse dual end unzipping mechanism. Additionally, the MD simulations showed that the increased release rate near the AuNP surface was due to increased proximal bp separation.

In Chapter 5, we investigate the fs laser pulse optical heating of enzymes. The activity of enzymes is temperature dependent making them an ideal candidate for optical heating. Furthermore, the use of NP scaffolds for hosting enzymes can provide catalytic rate enhancements and increased enzyme stability through a variety of different physical mechanisms.<sup>6, 53-55</sup> Coupling optical heating to these systems could

provide for an even greater degree of control over enzyme kinetics. Our work has allowed us to identify the key variables that dictate these systems and we postulate that the percent increase of enzyme production during laser pulse optical heating is governed by the laser repetition rate, pulse duration and the enzyme turnover number. This allowed us to conclude that laser repetition rate of 1 kHz used in this work is not appropriate for significant enzyme activity enhancement, as the enzyme is only hot for a total of  $\sim 5 \mu\text{s}$  during 1 s of irradiation. We hypothesize that increasing the repetition rate and/or increasing the pulse duration could overcome these limitations

In Chapter 6, we digress and perform preliminary investigations on a novel class of biomaterials known as peptide nucleic acids (PNAs). While we do not currently examine the effect of fs laser pulse optical heating on PNAs, we consider them as candidate for this technique as it becomes more developed. Here, we utilize peptide-PNA hybrids to efficiently conjugate QDs to the surface of DNA nanostructures. We demonstrate that this technique can achieve greater than 90% capture efficiency for placing multiple QDs in a site-specific manner on a single DNA nanostructure. While we utilize QDs in this system as a proof on concept (for ease of capture detection and conjugation), the peptide-PNA hybrids could be used to efficiently tether AuNPs to specific locations on DNA nanostructures. As PNA duplexes have higher thermal stability than DNA duplexes, this conjugation technique could allow for localized heating on a DNA nanostructure without denaturing the PNA duplex and displacing the AuNP. This could enable the AuNP to thermally induce a local actuation in the DNA nanostructure.

Finally, in Chapter 7, we provide a conclusion of this work and discuss future lines of inquiry. Additionally, the publications and presentations that resulted from this dissertation are listed here.

## **Chapter 2: Using ultrashort laser pulses to release oligonucleotides from the surface of gold nanoparticles<sup>o</sup>**

<sup>o</sup>Reprinted (adapted) with permission from David A. Hastman, Igor L. Medintz, Sebastián A. Diaz, Considering variables in ultra-short laser pulses to release nucleic acids from the surface of gold nanoparticles, *Proc. SPIE 11255, Colloidal Nanoparticles for Biomedical Applications XV*, 112550C (21 February 2020).

### **2.1 Introduction**

Oligonucleotide based therapeutics have emerged as a promising tool for controlling disease progression through the regulation of genes. The method of therapeutic action depends on the class of oligonucleotide: antisense oligonucleotides interact with messenger (m) RNA and inhibit translation of specific proteins,<sup>56</sup> DNazymes selectively bind to target mRNAs to induce hydrolysis and suppress specific genes,<sup>57-58</sup> aptamers directly interact with proteins in order to interfere with protein function,<sup>58</sup> and small interfering RNAs (siRNAs) bind to complementary RNA segments and block protein transcription.<sup>59</sup> Using oligonucleotides in combination with NP-mediated drug delivery systems has gained significant interest as NPs can provide a controlled release mechanism and enable specific targeting *in vivo* by decoration with antibodies, peptides, *etc.*,<sup>11</sup> AuNPs have shown promise as scaffolds for oligonucleotide based therapeutics as they are biocompatible, can easily be conjugated to ligands, drugs, and oligonucleotides for targeting, and have unique optical properties that can be used for imaging, photothermal release, and photothermal therapy.<sup>26, 60-61</sup> While there are numerous examples in the literature that have demonstrated the potential of AuNP mediated photothermal delivery of oligonucleotides, a majority of

these systems have utilized CW laser sources.<sup>31, 45, 62-64</sup> As discussed in Chapter 1, generating a significant local temperature increase near the AuNP surface with CW excitation requires either high irradiance values or collective heating effects, limiting its application to biological systems that can tolerate a significant bulk temperature increase. While one report has demonstrated single AuNP heating and release of siRNA using CW excitation, the AuNPs were heated using a sophisticated optical trap system at very high irradiance values ( $10^{10}$  W/m<sup>2</sup>).<sup>62</sup> Oligonucleotide release in CW heating conditions is relatively straightforward as the temperature profiles innate to CW excitation are similar to that of conventional bulk heating. Ultrashort laser pulse excitation of AuNPs has also been used to release attached oligonucleotides.<sup>12, 48-49</sup> While these reports have demonstrated the potential of ultrashort laser pulse-mediated oligonucleotide release, the physicochemical process by which the oligonucleotide release occurs is not fully understood and this continues to be an impediment to medical translation. This is primarily due to the vast parameter space innate to these systems (*e.g.*, NP size/shape/concentration, laser pulse width, laser pulse radiant exposure, heat dissipation rate, spacing from the NP surface, and linkage chemistries) that make a comprehensive understanding elusive. In the following chapter, we review some of relevant physical properties of DNA-AuNP conjugates and examine examples from the literature in order to pinpoint some critical parameters that are believed to influence the oligonucleotide release in systems utilizing ultrashort laser pulse excitation.

## ***2.2 DNA-AuNP conjugates***

### *2.2.1 DNA composition and structure*

In this section we provide a brief background on the physical properties of oligonucleotides as they relate to photothermal release. A majority of the work performed in this field has utilized DNA as the oligonucleotide of choice, as DNA can be purchased commercially at low cost and does not degrade as readily as RNA. As the work performed in this dissertation also uses DNA, we will focus our discussion on the physical properties of DNA, a biopolymer that is composed of deoxyribonucleotides. The deoxyribonucleotides are composed of one of four nitrogenous bases; adenine (A), thymine (T), guanine (G), and cytosine (C) and are linked together by phosphodiester bonds. The deoxyribonucleotide is denoted by the specific base either A, T, G, or C. DNA strands have directionality and contain a 5' end (phosphate group) and a 3' end (hydroxyl group). Each base has a complementary base that it pairs with (A to T, G to C) by hydrogen bonding and when two DNA strands have a full sequence of complementary bases they are said to be complementary strands and can form a double helix structure or double-stranded (ds)DNA. A schematic of dsDNA is shown in Figure 2.1A. The double helix diameter is ~2 nm and the double helix structure repeats itself every 3.4 nm or ten base pairs.

As mentioned above, when two DNA strands are complementary to each other, they can form a duplex or dsDNA. While the base pairing stabilizes the duplex through hydrogen bonding and hydrophobic interactions, the negative charge of the phosphate backbone repels the duplex formation, making the stability of this duplex dependent on ionic strength and temperature. Duplex stability is typically thought of in terms of

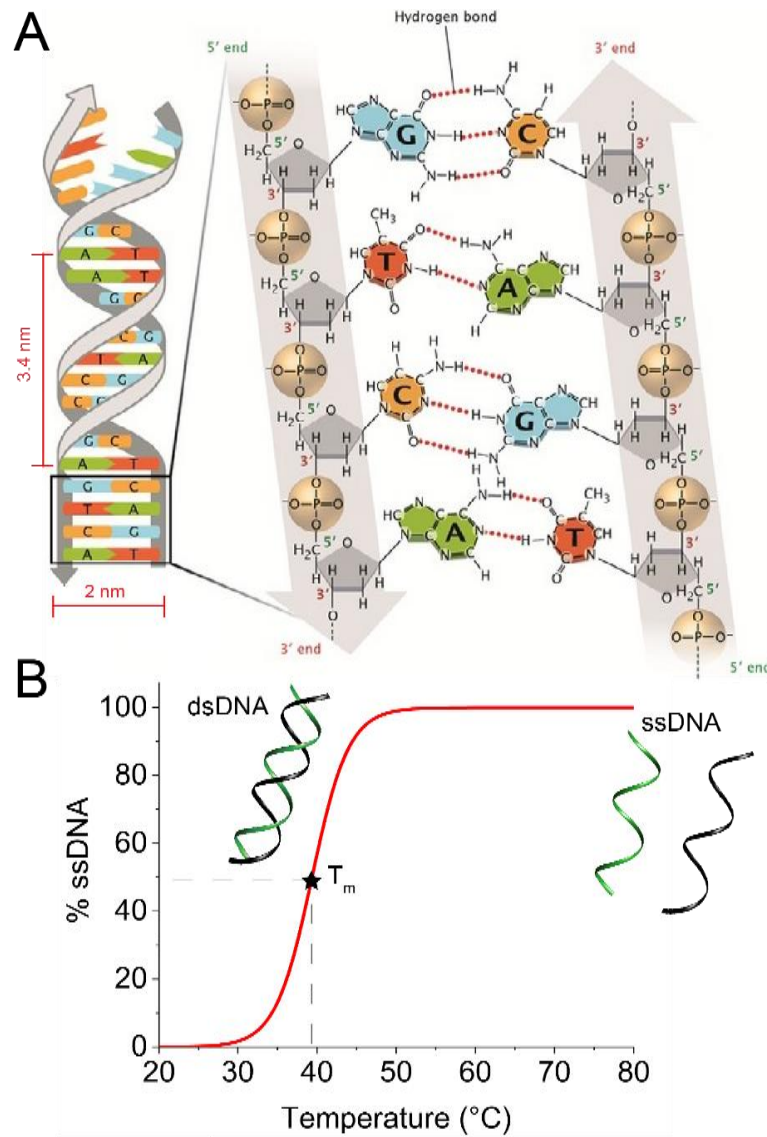


**Figure 2.1:** A) Schematic of a dsDNA. dsDNA duplex formed through hydrogen bonding of the DNA bases; adenine (A), thymine (T), guanine (G), and cytosine (C). The double helix diameter is ~2 nm and the double helix structure repeats itself every 3.4 nm or ten base pairs. Reprinted (adapted) with permission from Pray, Leslie. (2008) *Discovery of DNA structure and function: Watson and Crick. Nature Education* 1(1):100. Copyright 2008 Nature Education. B) dsDNA melting curve and  $T_m$  determination. dsDNA becomes unstable at elevated temperatures and begins to denature into two ssDNA strands. The  $T_m$  is point at which 50% of the dsDNA strands in solution are melted into ssDNA. The  $T_m$  of the DNA represented in this graph is 39 °C.

temperature, as heating dsDNA separates the two strands. The separation (typically thermally induced) of dsDNA into two ssDNA strands is known as denaturation or dehybridization. Upon cooling the ssDNA will base pair with its complementary strand and reform into dsDNA and is known hybridization. The melting temperature ( $T_m$ ) of a duplex is the standard quantification of stability and is defined as the temperature at which 50% of the dsDNA in solution is melted into ssDNA. The  $T_m$  of a duplex is dependent on the ionic strength of the solution (positive ions such as  $\text{Na}^+$  and  $\text{Mg}^{2+}$  screen the negative charge of the phosphate backbone), the length of the duplex (more base pairs require more energy to break) and the G/C composition (G and C have 3 hydrogen bonds to break while A and T have two hydrogen bonds to break). A schematic and graphical representation of dsDNA melting into two ssDNA strands is shown in Figure 2.1B. The  $T_m$  of the DNA shown in Figure 2.1B is 39 °C.

### *2.2.2 DNA modification for AuNP attachment*

Structural DNA nanotechnology has harnessed the specificity of DNA base pairing and allowed researchers to essentially “program” multiple DNA strands in solution to assemble into a vast number of diverse nanostructures. DNA can be designed to make structures that are composed of up to 3000 individual strands and have dimensions spanning from 2 nm to several  $\mu\text{m}$ .<sup>65</sup> Researchers have thought to use this functionality as a tool and have used structural DNA nanotechnology to engineer and study many small scale systems such as molecular photonic wires,<sup>66</sup> plasmonic complexes,<sup>9</sup> biological sensors,<sup>67</sup> and many others.<sup>65-66, 68</sup> Due to this broad interest, DNA can now be modified with numerous functional groups that enables their conjugation to NPs, surfaces, proteins, fluorescent dyes, and many other nano/biomaterials. One of these



modifications is the thiol (reactive –SH group) modification, which is used to react with a wide array of chemical groups and is the prototypical chemistry used to attach biomaterials to a gold surface.<sup>52, 69</sup> The thiol is chemisorbed onto the gold surface with the reductive elimination of the hydrogen atom and the sulfur atom contributing a lone pair of electrons to the empty orbitals of gold atoms on the surface.<sup>70</sup> This is known as a dative bond and these bonds can be comprised by changes in pH, oxidation or displacement by other molecules.<sup>70</sup> When attaching thiolated DNA to the surface of gold the thiol modifier is typically placed on the 5' or 3' end of the DNA so that the DNA extends linearly from the Au surface, leaving the base pairs exposed for subsequent hybridization.

In the context of DNA display on AuNPs, thiolated ssDNA is scaffolded onto the AuNP surface and the loading is dependent on the AuNP size, conjugation conditions and DNA length/sequence.<sup>52</sup> The negatively charged DNA typically stabilizes the AuNPs in solution making DNA-AuNP conjugates colloidally stable in a range of buffers and pHs.<sup>71</sup> The thiolated ssDNA can be hybridized with a complementary strand (before or after loading onto the AuNP surface) to form dsDNA duplexes on the AuNP surface. In Figure 2.2 (left side) a schematic of thiolated DNA (black) hybridized with a complementary DNA strand (green) and attached to a AuNP is shown. As seen in the close up image of dsDNA-AuNP (bottom left), only the thiolated DNA strand is<sup>70</sup> attached to the AuNP surface. The hybridization and denaturation of DNA in close proximity to the surface of AuNPs is more complex due to hydrophobic and van der Waals interactions between the bases and the Au surface.<sup>72-74</sup> While the kinetics and dynamics of these processes are not fully understood,<sup>16</sup> the hybridization and

denaturation of DNA on a AuNP surface has been demonstrated in numerous examples including the photothermal denaturation of AuNP scaffolded dsDNA.<sup>48, 50, 75-76</sup>

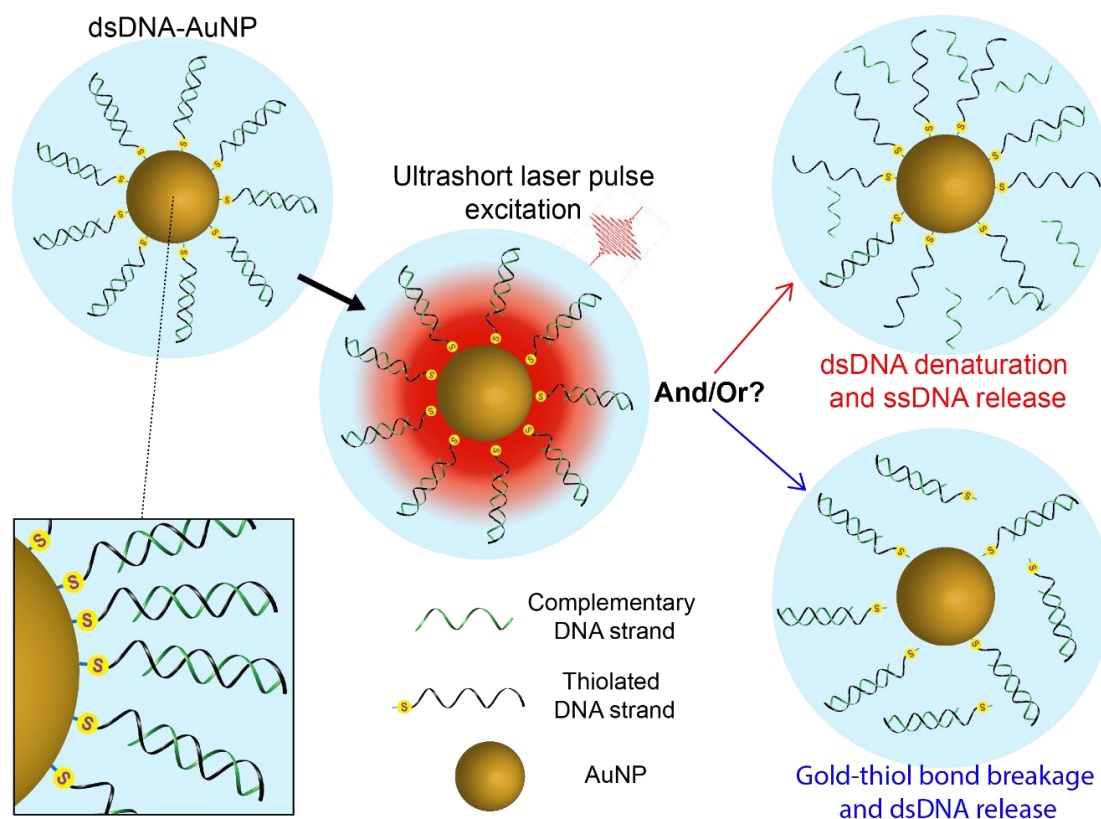


**Figure 2.2:** Schematic of a dsDNA-AuNP conjugate and photothermal release mechanisms. Thiolated DNA (back) is hybridized to the complementary strand (green) and attached to the AuNP surface. After ultrashort laser pulse excitation, the AuNP is heated and DNA is released through either: 1) (red) the thermal denaturing of a dsDNA and release of the complementary ssDNA into solution, 2) (blue) the cleavage of the gold-thiol bond and the release of the complete dsDNA into solution, or 3) a combination of both.

### 2.2.3 Mechanisms of DNA photothermal release on the surface of AuNPs

Typically, in these systems a thiolated DNA or template strand is bound to the surface of the AuNP via a gold-thiol bond and a complementary nucleic acid strand is hybridized to the template.<sup>12, 45, 48-50, 62</sup> When the AuNPs are excited by an external light

source with a high enough photon flux near the AuNP absorbance, the DNA can be released from the AuNP surface due to the subsequent heating. Depending on the experimental system in question, the release mechanism is reported as either: 1) the thermal denaturing of dsDNA and release of the complementary ssDNA into solution,<sup>50</sup> 2) the cleavage of the gold-thiol bond and the release of the complete dsDNA into solution,<sup>12</sup> or 3) a combination of both.<sup>48</sup> The schematic in Figure 2.2, outlines the two proposed release mechanisms (duplex denaturation in red and gold-thiol bond cleavage in blue). To the best of our knowledge, all previous reports using CW laser excitation have observed thermal duplex denaturation.<sup>12, 45, 62</sup>

In order to probe the state of these systems (*i.e.*, whether the thiolated DNA strand is attached to the gold or whether the complementary strand is hybridized to the thiolated strand) the DNA strands can be labeled with a fluorescent dye that engages in energy transfer with the AuNP surface.<sup>12, 48, 50</sup> Metallic NPs are known to ubiquitously quench fluorophores when in close proximity ( $< 40$  nm) and while the underlying mechanism is still not fully understood, it appears to be dependent upon dipole coupling and has been exploited for innumerable turn-on fluorescent sensors.<sup>77-79</sup> The quenching of the fluorescent labeled DNA occurs when the DNA is close to the AuNP surface and the fluorescence is restored when the DNA is released into solution. By monitoring the fluorescence intensity of the system, the release of the DNA from close proximity of the AuNP surface can be monitored.

In the following section, we review the literature and discuss the current understanding of the DNA release mechanisms using ultrashort laser pulse excitation of AuNPs.

## 2.3 Ultrashort laser pulse excitation of dsDNA-AuNP conjugates

### 2.3.1 Fs laser pulse excitation of dsDNA-AuNP conjugates

In 2006, Jain *et al.* were the first to examine the effect of fs laser pulses on DNA-modified AuNPs.<sup>80</sup> Here, a 400 nm laser with a 100 fs pulse width was used to generate pulse radiant exposures ranging from 5 - 3200 J/m<sup>2</sup> to excite 13 nm diameter spherical AuNPs functionalized with ssDNA. In this system, no complementary DNA was used. After AuNP excitation, the hot electron lifetimes in unmodified AuNPs were compared to that of DNA-modified AuNPs using fs transient bleaching experiments. They found that at low pulse radiant exposures, the hot electron lifetimes of DNA modified AuNPs and unmodified AuNPs were similar, yet as the pulse radiant exposure was increased stepwise the electron relaxation rate in the DNA-modified AuNPs becomes progressively faster compared to the unmodified AuNPs. Typically the hot electrons decay through the process of electron-phonon coupling (*i.e.*, AuNP lattice heating), and the faster decay rate of the DNA modified AuNPs indicated that an additional decay pathway for the hot electrons was present. The manuscript concluded that this additional decay pathway was the breaking of the gold-thiol bond and that the extent of bond breaking increased with the pulse radiant exposure. Below in Figure 2.3, the fs transient bleaching of the (a) unmodified and (b) modified AuNPs are shown for various pulse radiant exposures. The hot electron relaxation times  $\tau_d$  and  $\tau_d'$  are obtained by fitting the transient bleaching data to the exponential function  $(1 - \exp(-t/\tau_r)) \exp(-t/\tau_d)$ , where  $\tau_r$  is the rise time. Looking at pulse energies of 378 nJ and 864 nJ (48 J/m<sup>2</sup> and 110 J/m<sup>2</sup>, respectively) we can see that the relaxation time for the DNA modified AuNPs is decreased by approximately 20% compared to the unmodified

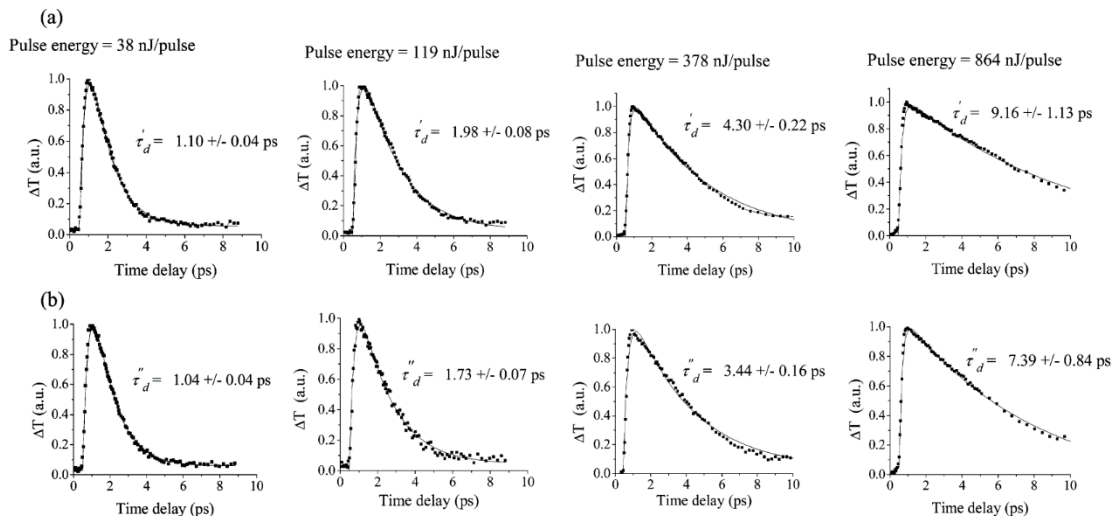


**Figure 2.3:** Transient bleaching in (a) unmodified AuNPs and (b) thiolated single stranded DNA-modified AuNPs. Excited using 100 fs 400 nm pulses at energies of 38, 119, 378 and 864 nJ/pulse (pulse radiant exposures of 1.7, 15.2, 48, and 110 J/m<sup>2</sup> respectively). The hot electron relaxation times  $\tau'_d$  and  $\tau''_d$  are obtained by fitting the transient bleaching data to the exponential function  $(1 - \exp(-t/\tau_r)) \exp(-t/\tau_d)$ , where  $\tau_r$  is the rise time. Reprinted with permission from Prashant K. Jain, Wei Qian and Mostafa A. El-Sayed, Ultrafast Cooling of Photoexcited Electrons in Gold Nanoparticle–Thiolated DNA Conjugates Involves the Dissociation of the Gold–Thiol Bond, *Journal of the American Chemical Society* 2006, 128 (7), 2426-2433. Copyright 2006 American Chemical Society.

AuNPs. In contrast, at pulse energies of 38 nJ and 119 nJ (1.7 J/m<sup>2</sup> and 15.2 J/m<sup>2</sup>, respectively) the relaxation time for DNA modified AuNPs is only decreased by 5% and 13% compared to the unmodified AuNPs. This indicates that amount of gold-thiol bond cleavage can be controlled depending on the amount of energy delivered to the AuNP in a single pulse. While no complementary DNA strand was present in this system this finding suggest that the pulse radiant exposure is a key variable that dictates the DNA release mechanism.

In 2017, the Halas group compared the DNA release mechanisms from AuNPs under CW irradiation to that of fs pulsed irradiation.<sup>12</sup> Using large gold nanoshells

(AuNS) (~120 nm SiO<sub>2</sub> core, 21 nm Au shell), they probed the release of dsDNA under each irradiation type. To monitor the DNA release they labeled either the thiolated DNA strand or the complementary strand with unique fluorescent markers that allowed them to detect the presence of a given strand in solution after irradiation. During CW irradiation, collective heating effects from the AuNSs in solution caused a bulk temperature increase and thermally induced dehybridization of the dsDNA. When exciting the AuNS with 165 fs 800 nm laser pulses (pulse radiant exposures of 2 – 46 J/m<sup>2</sup>) they reported that the dsDNA was being released through gold-thiol bond breaking. In Figure 2.4, the release profiles for the (A) complementary strand and the

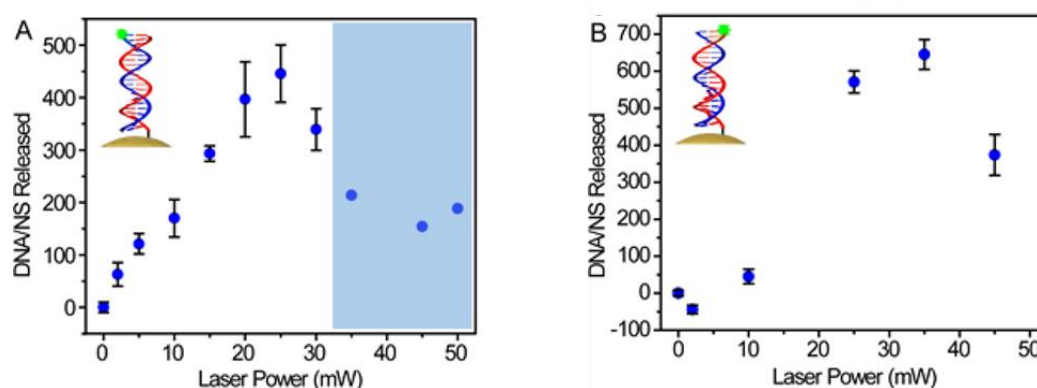


**Figure 2.4:** DNA release profiles during fs laser pulse excitation of AuNS. (A) DNA release profile of fluorescently tagged complementary (non-thiolated) DNA strand under increasing laser power. Highlighted blue box indicates powers at which AuNS reshaping occurs. (B) DNA release profile of fluorescently tagged thiolated DNA strands under increasing laser power. The AuNS were excited with 165 fs 800 nm laser pulses (pulse radiant exposures of 2 – 46 J/m<sup>2</sup>). For reference 20 mW average power equates to a pulse radiant exposure of ~18.2 J/m<sup>2</sup> in this system. Reprinted (adapted) with permission from Amanda M. Goodman, Nathaniel J. Hogan, Samuel Gottheim, Carrie Li, Susan E. Clare, and Naomi J. Halas, Understanding Resonant Light-Triggered DNA Release from Plasmonic Nanoparticles, *ACS Nano* 2017, 11 (1), 171-179. Copyright 2017 American Chemical Society.

(B) thiolated strand are shown for a given average irradiance. While gold thiol bond breaking is clearly observed at higher powers ( $> 25$  mW), significant release was not observed at lower powers. The amount of complementary DNA (A) released at lower pulse radiant exposures ( $< 9.1$  J/m<sup>2</sup> or an average power of 10 mW) is greater than 3 times the amount of thiolated DNA released. This indicates that thermal denaturation of dsDNA is the prevalent release mechanism occurring at these lower pulse radiant exposures.

Recently, Riley *et al.* demonstrated the release of siRNA using a system similar to that used by the Halas group discussed in the above paragraph.<sup>45</sup> Using a 40 fs laser pulse at 800 nm, AuNS (~120 nm SiO<sub>2</sub> core, 21 nm Au shell) displaying siRNA duplexes were excited with pulse radiant exposures from 50-150 J/m<sup>2</sup>. They reported that both siRNA duplexes and ss siRNA are released through pulsed irradiation, but that duplexes are the predominate species. This is not surprising as the pulse radiant exposures used in their system are higher than that of the lowest used by Halas group.<sup>12</sup>

To the best of our knowledge, these are the only reports using fs laser pulses to release DNA displayed on AuNPs. In Table 2.1 the experimental systems and reported release mechanism are listed. From these reports, it seems evident that gold thiol bond breaking occurs more frequently at higher pulse radiant exposures. It is difficult to quantify a pulse radiant exposure threshold that causes gold-thiol bond breaking as the differences in excitation wavelength and NP size/shape/composition make the comparison of these reports quite complicated. Yet, from these reports we conclude that when using a fs pulse width, pulse radiant exposures at or above 20 J/m<sup>2</sup> promote gold-thiol bond breaking over dsDNA denaturing.

Pulse width	Rep rate	Pulse radiant exposure (J/m <sup>2</sup> )	Excitation wavelength	Nanoparticle	Reported release mechanism	Ref.
250 ns	Single pulse or 1 Hz	400 - 1960	527 nm	AuNP 41- 52 nm	Thermal denaturation below pulse radiant exposure of 1550 J/m <sup>2</sup> and gold-thiol bond breaking at higher pulse radiant exposures	50
4 ns	10 Hz	500 - 1020	532 nm	AuNP 16 nm	Thermal denaturation and gold-thiol breaking. At increased pulse radiant exposures the amount of gold-thiol breakage increased.	48
100 fs	1 kHz	5 - 3200	400 nm	AuNP 13 nm	Gold-thiol bond breakage (amount increases at higher pulse radiant exposures)	80
40 fs	10 kHz	50 - 150	800 nm	AuNS 120 nm SiO <sub>2</sub> core 21 nm Au shell	Thermal denaturation and gold-thiol breaking. At increased pulse radiant exposures the amount of gold-thiol breakage increased.	45
150 - 180 fs	250 kHz	2 - 46	800 nm	AuNS 120 nm SiO <sub>2</sub> core 21 nm Au shell	Gold-thiol bond breakage	12

**Table 2.1:** Examples of ultrashort laser pulse excitation of AuNPs for DNA release.

### 2.3.2 *Ns laser pulse excitation of dsDNA-AuNP conjugates*

Other reports have utilized ns pulses of light to release DNA from the surface of AuNPs.<sup>48, 50</sup> This was first demonstrated by Poon *et al.* in 2010 using 16 nm AuNPs functionalized with dsDNA.<sup>48</sup> In this setup, they labeled both the thiolated strand and



complementary (non-thiolated) strand with a fluorescent marker to quantify release. Using a 4 ns laser pulse at 532 nm, they excited the AuNPs with pulse radiant exposures of 50-1020 J/m<sup>2</sup> and monitored the release of the thiolated and non-thiolated strands. They reported that the thermal denaturation of dsDNA and release of the complementary strand is favored to an extent of more than six to one compared to gold-thiol breaking and dsDNA release at a pulse radiant exposure of 50 J/m<sup>2</sup>. When the pulse radiant exposure was increased, the amount of gold-thiol breaking also increased. Interestingly, they found that increasing the salt concentration in the solution significantly reduced (~4 fold) the amount of thiolated strand released into solution. The group speculated that the electrostatic repulsion between DNA strands promotes the breaking of the gold thiol bond and that reducing the electrostatic repulsion by adding salt effectively raised the activation energy required for gold thiol-bond cleavage. In 2012, Thibaudau published a report where ~55 nm AuNPs displaying dsDNA were irradiated with a 250 ns 527 nm laser pulse operating at pulse radiant exposures of 400-1960 J/m<sup>2</sup>.<sup>50</sup> Here, it was observed that thermal denaturation of the dsDNA and ssDNA release was the primary release mechanism when operating at pulse radiant exposures below 1550 J/m<sup>2</sup> and dsDNA release through gold-thiol bond breaking started to occur at higher pulse radiant exposures. Of perhaps equal interest, Thibaudau demonstrated the thermal denaturation of dsDNA using a single 250 ns pulse.

As reported with fs laser pulse excitation, ns laser pulse excitation seems to favor gold thiol bond breakage. Comparing the pulse radiant exposure generated from a ns pulse to a fs pulse is not appropriate as the time over which the pulse is absorbed by

the AuNP varies by 6 orders of magnitude. While much more work is needed before researchers can predict the pulse radiant exposure that will cause gold thiol bond breaking for a given NP-laser combination, the preliminary work in the field clearly points to the existence of a system dependent pulse radiant exposure threshold for cleavage of the gold thiol bond.

## ***2.4 Conclusions***

From the literature it is evident that the extent of gold-thiol bond breaking from ultrashort laser pulsed excitation of AuNP-nucleic acid bioconjugates is dependent on the amount of energy absorbed by the AuNPs. Due to the drastic difference in pulse widths between ns and fs pulses it is difficult to compare results between these two systems. Yet, experimental results with both ns and fs pulse widths indicate that for a given NP-laser system there exists a pulse radiant exposure “threshold” that defines the gold-thiol stability. While the direct application dictates the type of release desired (complete duplex release or ssDNA release), a majority of the therapeutic applications utilize ss nucleic acids, making the thermal denaturation release mechanism preferential. Additionally, a variety of thiolated materials can be appended to the surface of AuNPs. In these systems the stability of the gold-thiol bond is highly desired, as temperature sensitive molecules, such as proteins<sup>30</sup> or polymers<sup>60</sup> can be attached to AuNPs so that light pulses can deliver highly localized heating to these molecules in order to modulate their activity or function. As such, the work presented in this dissertation is performed in the pulse radiant exposure regime that promotes gold-thiol bond stability and nucleic acid denaturation.

While a few proof of concept studies have shown nucleic acid denaturation using AuNPs excited with ultrashort pulses of light, precise control over nucleic acid denaturation has not been demonstrated. Although it is evident that the dsDNA denaturation is occurring through a thermal mechanism in these systems, it is not clear how dsDNA of different lengths respond to these dynamic temperature increases. Furthermore, no work to date has examined the dependence of the DNA release rate on the distance at which the dsDNA resides from the AuNP surface. This is a critical variable in these systems as the temperature profile from fs laser pulse excitation of AuNP follows a  $1/r^3$  dependence.<sup>36</sup> Probing the thermal denaturation of DNA in steep temperature gradients and short heat pulses could also provide insight into the thermal responses of other biological materials, as only a few biological materials have been examined in this context.<sup>46-47</sup> To this end, the primary focus of Chapters 3-5 is understanding how oligonucleotides and other biological materials respond to the nanosecond heat pulses and steep temperature gradients found around the AuNP after excitation with an ultrashort pulse of light. In Chapters 3 and 4 we perform a systematic examination of dsDNA denaturation on AuNPs from fs laser pulse excitation. In doing so, we demonstrate precise control over DNA release and propose a method to quantify the temperature “sensed” by the DNA. Furthermore, using our experimental findings in combination with MD simulations, we provide a basic understanding of the DNA denaturation mechanism in these dynamic temperature increases.

## **Chapter 3: Femtosecond Laser Pulse Excitation of DNA-Labeled Gold Nanoparticles: Establishing a Quantitative Local Nanothermometer for Biological Applications\***

\*Reprinted (adapted) with permission from David A. Hastman, Joseph S. Melinger, Guillermo Lasarte-Aragones, Paul D. Cunningham, Matthew Chiriboga, Zachary J. Salvato, Thomas M. Salvato, Carl W. Brown III, Divita Mathur, Igor L. Medintz, Eunkeu Oh, and Sebastián A. Díaz, Femtosecond Laser Pulse Excitation of DNA-Labeled Gold Nanoparticles: Establishing a Quantitative Local Nanothermometer for Biological Applications, *ACS Nano* 2020. Copyright 2020 American Chemical Society.

### **3.1 Introduction**

Release of nucleic acids from the surface of AuNPs using ultrashort pulses of light has been undertaken by a number of different groups as a method to optically trigger nucleic acid release both *in vitro* and *in vivo*.<sup>12, 48, 81-84</sup> There are, however, conflicting accounts regarding the mechanism of nucleic acid release and precise control over temperature increases in ranges of interest to biological activity has not been demonstrated. Typically, dsDNA is attached to the AuNP surface by modifying one of the nucleic acid strands with a thiol group, allowing the DNA and AuNP to form a gold-thiol bond.<sup>52</sup> A complementary nucleic acid strand is then hybridized to the thiolated strand but not bound to the AuNP surface. In these systems, observations following light irradiation have suggested either the non-thermal cleavage of the gold-thiol bond and subsequent release of the dsDNA duplex,<sup>12</sup> or, alternatively the thermal denaturation of the duplex and the subsequent release of the ss non-thiolated complementary nucleic acid strand while the thiolated strand remains attached to the

AuNP through the gold-thiol bond,<sup>84</sup> as well as a combination of these two mechanisms.<sup>48</sup> Interestingly, as discussed in Chapter 2, some reports identify radiant exposure or irradiance thresholds that separate the thermal denaturing regime from the gold-thiol breakage.<sup>48, 84</sup> Our focus is on the thermal denaturation of the duplex and preservation of the gold-thiol bond during irradiation, as the gold-thiol bond can be used to scaffold a wide range of biological materials to the surface of AuNPs,<sup>60</sup> and could be used as a facile attachment mechanism for other biologicals that can be thermally controlled.

While many of the previous studies using ultrashort pulses of light to photothermally heat AuNPs have quantified the amount of DNA/RNA released during irradiation, no study, to the best of our knowledge, has systematically examined the rate of DNA release in dsDNA-AuNP systems using dsDNAs of different melting temperatures and in varying bulk solution temperatures. To this end, we have designed an experimental system consisting of three unique dsDNA-AuNP conjugates, each with a distinct melting temperature (see Figure 3.1A and section 3.2.1 for details) to examine DNA release kinetics and better understand the process of fs-laser pulse induced DNA denaturation on AuNPs. We used laser pulse radiant exposures below 15 J/m<sup>2</sup> (see section 3.2.1 for determination of pulse radiant exposures) to increase the local temperature around 55 nm AuNPs causing the DNA duplexes displayed on the AuNP surface to thermally denature. By modulating the pulse radiant exposure and the bulk solution temperature, we were able to discern how dsDNA of different melting temperatures reacts to the confined temperature increase around the AuNP during fs-

pulse illumination and probe the local temperature profile. We find that the rate of

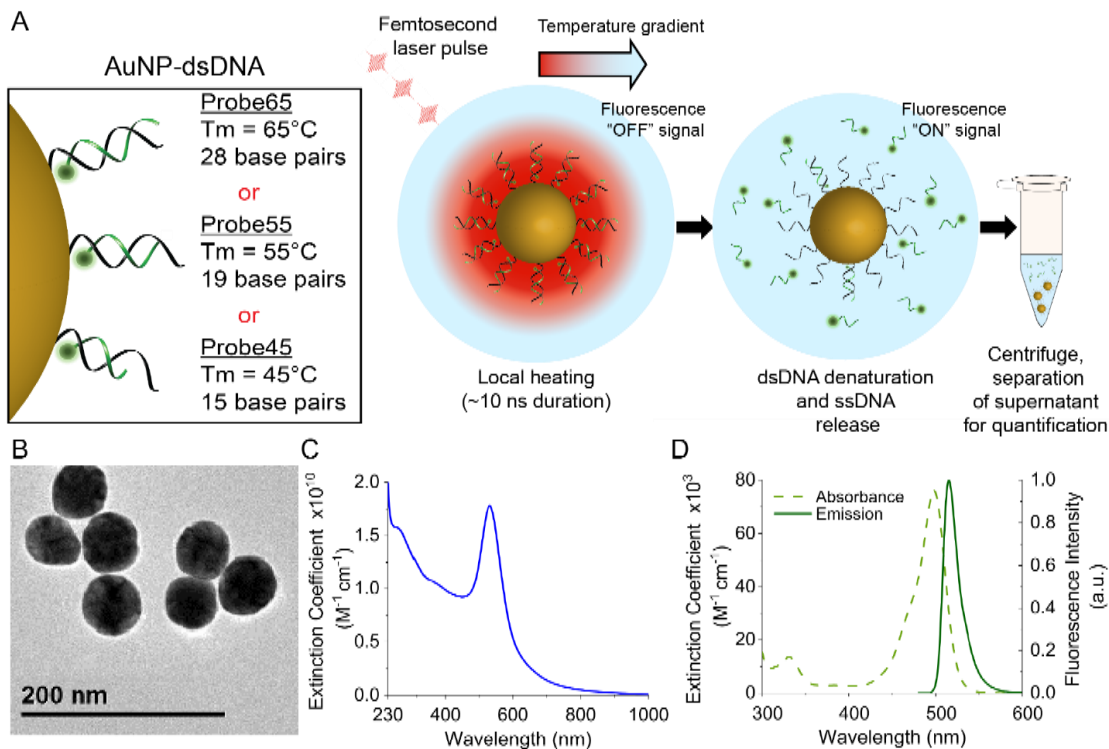


**Figure 3.1:** Schematic and component characterization of AuNP-dsDNA nanothermometer: A) Schematic showing the dsDNA-AuNP system, with the varying DNA strands noted in the highlighted box (left). Local heating due to laser induced photothermal event and subsequent DNA release (right). Although the fluorescence ON signal is detectable immediately after DNA release, the quantification of the signal occurs after the AuNPs and ssDNA are separated *via* centrifugation. B) TEM image of unmodified  $55 \pm 5$  nm diameter AuNPs. C) Absorbance spectra of the AuNP. D) Absorbance and fluorescence spectra of Oregon Green 488 dye used to label probe DNA strands.

photothermally-induced DNA denaturation depends on both the DNA melting temperature as well as the bulk solution temperature and the local temperature increase generated from the absorbed laser pulse. Using these variables as control levers we show regulation over the rates of DNA release without causing a temperature increase throughout bulk solution. Furthermore, we fit the observed release profiles in our

system to a modified DNA dissociation equation to obtain a “sensed” local temperature value, this provided a quantitative local nanothermometer as well as an initial understanding of how DNA responds to fs-pulse induced heating when displayed on the surface of an AuNP.

### ***3.2 Results and discussion***

#### *3.2.1 System design and characterization*

By examining various reported systems from the literature, we identified pulse radiant exposures that had been shown to cleave the gold-thiol bond and designed our system to operate well below these values in the thermal denaturation regime.<sup>12, 48, 84</sup> Based upon these previous reports, we also determined that working below a peak pulse irradiance of  $10^{14}$  W/m<sup>2</sup> or an radiant exposure per pulse of 20 J/m<sup>2</sup> promotes thermal denaturation over gold-thiol bond breakage. In designing our experimental system, we desired the local temperature around the AuNP to be increased up to ~100 °C. Here, we define local as the volume encompassed within 15 nm of the AuNP surface, as the DNA strands used in our system reside in this area. We simulated the temperature profile around various sized AuNPs after a single fs-laser pulse at pulse radiant exposures of 1-15 J/m<sup>2</sup> using a MATLAB program published by Metwally *et al.*<sup>85</sup> Based upon the temperature profiles generated from these simulations, we determined that 55 nm AuNPs were best suited to generate the desired temperature range at the aforementioned pulse radiant exposures. It is important to note that the theoretical radiant exposure threshold for photothermal bubble generation with 55 nm AuNPs is ~24 J/m<sup>2</sup>.<sup>85</sup> The highest pulse radiant exposure we use in this work is 14.1 J/m<sup>2</sup>,

virtually ensuring that water vapor bubbles are not forming around the AuNPs in our system. Additionally, Wang *et al.* found that when 50 nm AuNPs are irradiated with pulse radiant exposures below  $\sim 41 \text{ J/m}^2$  using a pulse width of 75 fs and repetition rate of 80 MHz, the Brownian motion of the AuNPs is stronger than the trapping potential,<sup>86</sup> allowing us to conclude that optical forces do not play a significant role in our system. Figure 3.1B, C displays a TEM image and the corresponding extinction spectra of the 55 nm AuNPs used in this work.

In order to avoid the formation of self-complementary structures in the DNA strands or any sequence dependent effects, we designed a universal 36 bp template strand containing a 5' thiol modification that enables attachment to the AuNP and a short ( $T_3$ ) thymine spacer to extend the duplex portion of the strand further away from the AuNP surface. The template strand acts as scaffold to three different dye-modified complementary probe strands used to visualize the melting of the DNA duplex. The probe strands, each having a distinct melting temperature and length, are denoted as Probe65 (28 bases), Probe55 (19 bases) and Probe45 (15 bases). The probe names are based on the  $T_m$  of the dsDNA in Celsius. Table 3.1 shows the DNA sequences used in this work as well as their relevant physicochemical properties. We limited ourselves to the aforementioned probe strands as sequences with higher melting temperatures increased the strand length beyond the  $\sim 15 \text{ nm}$  regime where the local heating putatively occurs and any further increase in GC content created unwanted secondary structure effects (determined using NUPACK).<sup>87</sup> Probe strands with lower melting temperatures were tested but presented hybridization stability issues at room temperature (RT).



Name	Sequence (5'-3')	Nucleotides (#)	Theoretical $T_m$ (°C)	Solution $T_m$ (°C)	$T_m$ on AuNP (°C)
Probe45	GTGAGTAGGTAGAGA/3AmMO-OG488	15	42.9	43.5 $\pm$ 0.2	39.4 $\pm$ 0.1
Probe55	TGAGGTGAGTAGGTAGAGA/3AmMO-OG488	19	53.2	52.4 $\pm$ 0.2	51.1 $\pm$ 0.4
Probe65	GAGGTGAGGTGAGGTGAGTAGGTA GAGA/3AmMO-OG488	28	64.7	65.5 $\pm$ 0.3	66.9 $\pm$ 0.2
Template	5ThioMC6-D/TTTTCTCTACCTACTCAC CTCACCTCACCTATTCC	36	67.9	----	----

**Table 3.1:** Physicochemical properties of the DNA strands. The theoretical  $T_m$  was determined using the OligoAnalyzer Tool from Integrated DNA Technologies (Coralville, IA), <https://www.idtdna.com/pages/tools/oligoanalyzer>. The solution  $T_m$  and the  $T_m$  while on the AuNP were determined from triplicate experiments using ensemble samples and a temperature controlled fluorometer where the  $T_m$  values were obtained by taking the maximum of the first derivative of the melting curves obtained through bulk solution heating. 3AmM0; 3' amino modification, OG488; Oregon Green 488, 5ThiolMC6-D; 5' thiol modification with a six-carbon linker.

The probe strands were labeled with Oregon Green<sup>TM</sup> 488 (OG488) on the 3' end in order to visualize the melting of the duplexes into solution using fluorescence. When a probe strand was hybridized to the template strand, the fluorescence of OG488 was quenched (>90%) by energy transfer (ET) to the AuNP surface. We estimated that the OG488 was less than 2 nm from the AuNP surface when the probe strand was hybridized to the template strand, see Figure 3.1A. At elevated temperatures, the DNA duplex was denatured, releasing the probe strand into solution and restoring the OG488 fluorescence. OG488 was chosen as the fluorescent reporter for this work as we found the fluorescence to be relatively temperature insensitive (Figure 3.2) and the emission (Figure 3.1D) overlapped well with the AuNP absorbance (Figure 3.1C), a

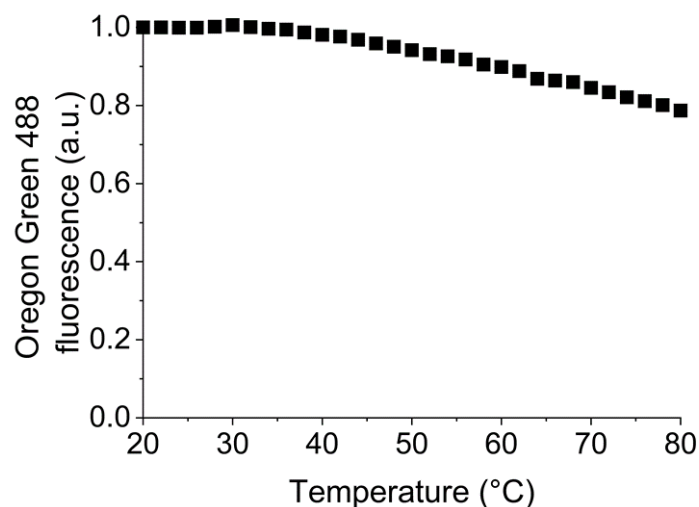


**Figure 3.2:** Temperature dependence of OG488 fluorescence. At each temperature, the OG488 was excited at 465 nm and the emission spectra was collected from 480-700 nm. The emission spectra was integrated and then normalized relative to the data point at 20 °C. Measurements were taking using a temperature controlled fluorometer. The relative intensity at each temperature was used to correct the fluorescent curves obtained from the bulk heating release of probe DNA (Figure 3.4).

characteristic which has been shown to improve quenching.<sup>88-90</sup> Additionally, the fluorescence of OG488 returns to baseline (*i.e.*, the fluorescence at RT) after heating to 80 °C and after irradiation, indicating OG488 is stable after thermal and laser treatment. We evaluated other fluorescent dyes (Cy3, Texas Red, and Alexa Flour 594) as potential reporters, but they were either unstable after thermal treatment or were photobleached during irradiation. We also found that hybridizing the template-probe dsDNA prior to loading onto the AuNP (referred to as pre-hybridized) demonstrated over a 5-fold higher probe DNA loading efficacy when compared to hybridizing the template-probe duplex after template-AuNP conjugation (data not shown). It has been reported that ssDNA is readily adsorbed onto AuNPs *via* van der Walls attraction between the exposed bases and the gold surface, whereas the relatively rigid duplex

structure of dsDNA inhibits the adsorption of the bases onto the AuNP surface.<sup>73, 91-92</sup>

We attributed the improved probe DNA loading observed in the pre-hybridized dsDNA-AuNP to this phenomena, as the duplex structure protects the DNA from non-specifically adsorbing to the AuNP surface during attachment. In contrast, hybridizing the probe strand to the template strand after AuNP conjugation leaves the DNA bases exposed, allowing them to non-specifically adsorb to the AuNP surface and interfere with the hybridization process. As such, all dsDNA-AuNP conjugates used in this work were created using the pre-hybridization procedure. dsDNA-AuNP conjugates were made in batch and washed three times through centrifugation followed by supernatant removal and re-dispersion of the dsDNA-AuNPs into fresh buffer in order to remove unbound/unhybridized DNA as best as possible. Samples were then divided into aliquots and run in a given experiment.

Prior to experiments, we determined the template strand surface coverage was  $14.8 \pm 0.7$  pmol/cm<sup>2</sup> or  $832 \pm 41$  strands per 55 nm AuNP using a quantification procedure described in Demers *et al.*<sup>93</sup> Briefly, the DNA on the AuNP surface was displaced using an excess of mercaptoethanol and then quantified through fluorescence and absorbance measurements once in solution. The template strand loading was in good agreement with previous studies.<sup>52</sup> The reported uncertainties arise from averaging over triplicate measurements. As discussed later, we also tested a range of loading densities to ensure our system was not significantly influenced by duplex-duplex crowding interactions at this loading density.<sup>94</sup> To determine the total number of probe strands per dsDNA-AuNP conjugate, samples were heated to 80 °C for 2 hours to dehybridize the DNA duplexes. The samples were then centrifuged to spin down the AuNPs leaving the

released ssDNA probe strands in the supernatant. The fluorescence of OG488 in the supernatant was then converted into number of probe strands released per AuNP using a standard curve (See Figure 3.3). The hybridization percentage of the probe strand (*i.e.*, the number of probe-template duplexes compared to the total number of template strands) was found to be  $40 \pm 5\%$ ,  $59 \pm 3\%$ , and  $51 \pm 7\%$  for Probe65, Probe55, and Probe45, respectively. The reported uncertainties again arise from averaging triplicate measurements. These hybridization percentages are on par with previous reports for dsDNA immobilization on AuNP surfaces, where estimated probe hybridization percentages of 20-50% were found.<sup>84</sup>

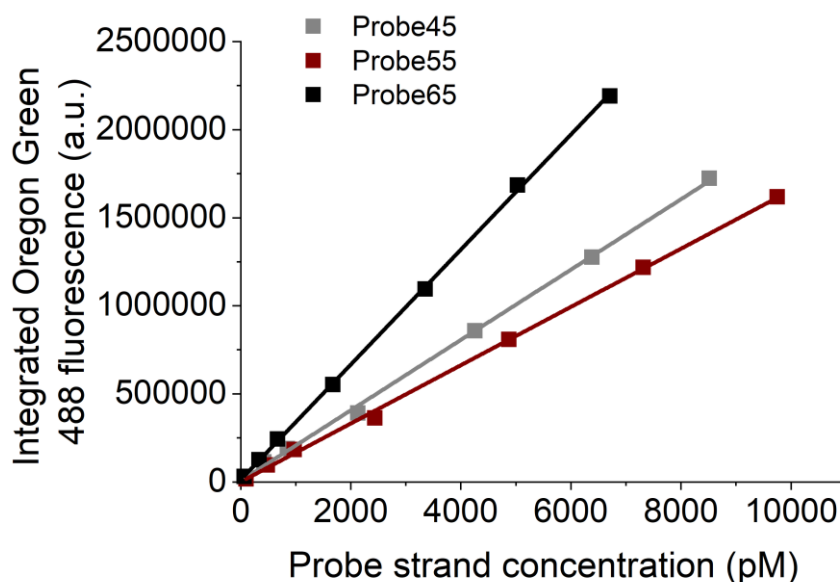


**Figure 3.3:** Standardization curves converting the fluorescence of OG488 labeled probe DNA to concentration of probe DNA. Known concentrations of OG488 labeled probe DNA were measured in a Tecan Infinite M1000 plate reader. OG488 was excited at 465 nm and the emission spectra was collected from 480-700 nm. The emission spectra was integrated to obtain the y-axis values.

### 3.2.2 Determination of DNA denaturation profiles using bulk solution heating

In order to first determine the melting profile of the dsDNA duplexes while free in solution, we used a modified template strand containing an Iowa Black®FQ Dark Quencher at the 5' end in place of the thiol modification. Thus, when the DNA was hybridized, the OG488 fluorescence was quenched through energy transfer to the Iowa Black. Quenching here occurs by conventional Förster resonance energy transfer (FRET) with the OG488-Iowa Black donor-acceptor pair displaying a Förster distance (*i.e.*, the distance at which the energy transfer is 50%) of 5.5 nm.<sup>95</sup> At elevated temperatures the dsDNA is denatured, separating the OG488 and Iowa Black to restore OG488 fluorescence. The melting profiles were obtained by using a temperature controlled fluorometer to increase the bulk solution temperature and monitor the fluorescence of OG488. We then investigated the melting behavior of the DNA duplexes while displayed on the AuNP surface using the same temperature controlled fluorometer. When the DNA dehybridizes on the AuNP surface, the probe strand is released into the solution separating the OG488 and AuNP to restore the OG488 fluorescence. Additionally, buffer conditions were optimized during these experiments, as salt and pH can have an effect on AuNP stability, DNA duplex stability, DNA melting temperature, and OG488 fluorescence.<sup>96-97</sup> After testing a wide range of buffers, salt concentrations, and pH values, it was empirically determined that a buffer of 50 mM HEPES pH 7.5 with 0.5 mM MgCl<sub>2</sub> met the required criteria (*i.e.*, a balance of colloidal stability, minimal dye quenching, distinct DNA melting profiles). In Figure 3.4, the melting profiles of each probe strand in solution and on the AuNP are shown and the corresponding observed melting temperatures are presented in Table 3.1. The

OG488 concentration was set at 10 nM during these experiments so that inner-filter effects could be neglected.<sup>98</sup> The melting temperatures of Probe55 (19 bp) and Probe45 (28 bp) were lower when displayed on the AuNP surface in contrast to that of Probe65

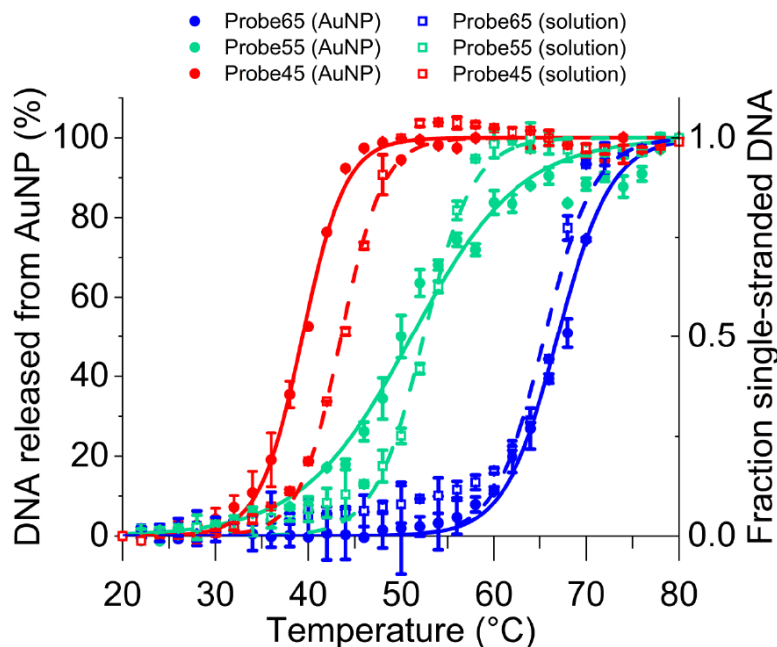


**Figure 3.4:** dsDNA denaturation in solution and on AuNP from bulk heating assays.  $T_m$  values are reported in Table 3.1 and were obtained by taking the maximum of the first derivative of the melting curves. The fluorescence of the dsDNA-AuNP conjugates was monitored in real time. Error bars represent the std. dev. for  $n = 3$  experiments.

(36 bp), for which the melting temperature was slightly higher on the AuNP surface. It has previously been shown that tethering dsDNA on a AuNP surface reduces the energetic barrier of dissociation and causes an accelerated dissociation of the dsDNA.<sup>94</sup> While we observed this with Probe55 and Probe45, we observed a slight shift in the opposite direction for Probe65 and speculate that Probe65 behaves similarly “on” and “off” the AuNP as the duplex is longer and a larger proportion of the bps in its structure

are situated further away from the AuNP surface reducing the accelerated dissociation seen in the shorter probe strands. Overall, the probe strands each displayed a distinct melting profile when bound to the AuNP, which was the most critical point of this assay. In these bulk heating assays, the fluorescence of the dsDNA-AuNP conjugates was monitored in real time. After bringing the solution temperature to 80 °C, which was found to release all of the probe DNA during the max loading assay described in the above section, the solution was slowly cooled back down to 20 °C. The fluorescent signal of the probe DNA did not proximity to engage in ET and that the probe strand did not rebind to the template strand after denaturation and release from the AuNP (data not shown). We hypothesize that this was due to steric issues as well as base adsorption of the template strand to the AuNP surface. While the DNA is in a duplex form, the dsDNA is rigid and extends linearly from the AuNP surface, but when the duplex is dehybridized and the probe strand diffuses into solution, the template strand remains on the AuNP surface in ss form allowing it to interact with itself, neighboring template strands, and the AuNP surface. It is likely that these interactions create a steric boundary making it more difficult for the probe strand to re-hybridize once released.<sup>99</sup> This hypothesis was also supported by the low hybridization efficiencies achieved when we attached the template strand to the AuNP before hybridization with the probe strand (~5%).

### *3.2.3 Femtosecond laser pulse heating for DNA release*

An amplified Ti:Sapphire laser system (Clark-MXR CPA) operating at a center wavelength of 775 nm, a 1 kHz repetition rate and with a 150 fs pulse width was utilized to excite the AuNPs in this study. This repetition rate and pulse width (duty cycle of

$1.5 \times 10^{-8}$  %) ensured that there is enough time for heat relaxation of the AuNP between pulses as the phonon-phonon coupling timescale for the AuNP and local environment is on the order of nanoseconds.<sup>85</sup> The pulse was frequency doubled using a barium borate (BBO) crystal to generate a working excitation wavelength of 387.5 nm. After removing the residual fundamental beam with a dichroic mirror, the light beam at 387.5 nm was gently focused using a 1 meter focal length lens, so that the spot size (3.3 mm diameter) did not change much over the 1 cm path of the sample cuvette. The laser irradiance was controlled using a waveplate-polarizer combination. The pulse radiant exposures used in our experiments ranged between 3.5-14.1 J/m<sup>2</sup>. The transmittance of the sample was ~74%. Immediately prior to experiments, dsDNA-AuNP conjugates were made in batch and washed three times through centrifugation, supernatant removal and re-dispersion of the dsDNA-AuNP into fresh buffer in order to remove unbound/dehybridized DNA. Next, the dsDNA-AuNP conjugate was diluted to a 13 pM AuNP concentration or  $\sim 7.8 \times 10^9$  particles per mL as this concentration places each AuNP at approximately 5  $\mu$ m from its nearest neighbor (mean inter-particle distance) and ensures that individual AuNPs are in a temperature confinement regime, *i.e.*, the influence of heat from neighboring particles can essentially be ignored.<sup>100</sup> For a detailed explanation of the temperature confinement evaluation, we refer the reader to the confinement number derivation in the book *Thermoplasmonics*.<sup>27</sup> During irradiation, we continuously monitored the bulk solution temperature using a thermocouple housed within a protective stainless steel sheath (Figure 3.5). At the highest pulse radiant exposure (14.1 J/m<sup>2</sup>) we did not observe any significant



temperature increase in the bulk solution ( $< 1.5\text{ }^{\circ}\text{C}$ ), with a similar nominal increase observed in a control buffer solution lacking AuNPs.

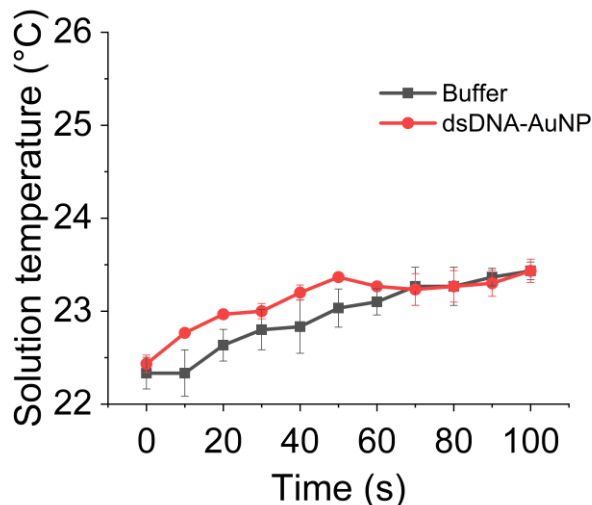


**Figure 3.5:** Bulk solution temperatures measured during irradiation at a  $14.1\text{ J/m}^2$  pulse radiant exposure. A type K thermocouple was used to measure the solution temperature. The buffer sample is a negative control with no AuNPs in solution. The AuNP concentration in the dsDNA-AuNP solution is 13pM. Error bars represent std. dev. for  $n = 3$  experiments.

At the 13 pM working concentration used for experiments, the AuNPs have an absorbance of 0.13 in a 1 cm path length using 387.5 nm light (extinction coefficient of  $1.01 \times 10^{10}\text{ M}^{-1}\text{cm}^{-1}$ ). While the effective pulse radiant exposure is slightly lower at the back of the sample than at the front, we observed no change in the release profile when samples were diluted by a factor of 2x, indicating that the slight change in the laser pulse absorption profile throughout the sample does not significantly impact the observed DNA release profiles. The sample volume was restricted to 200  $\mu\text{L}$  so that the laser beam could interact with the whole sample during irradiation, deriving nearly homogeneous laser exposure without the need for mixing or stirring the sample. Each

sample was placed into the laser path and irradiated for a given number of pulses (up to  $1 \times 10^5$  pulses or 100 seconds). During irradiation, no precipitation or flocculation of the AuNPs was observed in the cuvette. To further ensure that the AuNPs were not aggregating, we carefully monitored the absorbance spectrum of the dsDNA-AuNP samples throughout each assay using UV-Vis spectrometry. Each sample was also lightly vortexed before irradiation to make sure the AuNPs were well dispersed. Figure 3.6 displays an example absorbance spectrum representing a dsDNA-AuNP sample

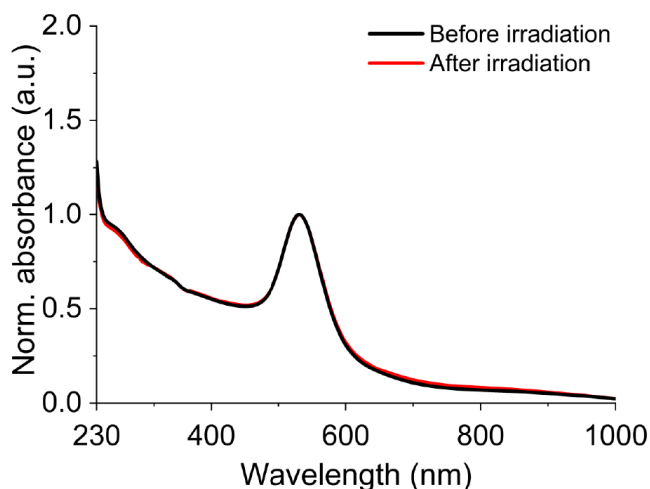


**Figure 3.6:** Absorbance of 13 pM dsDNA-AuNP conjugate (with Probe55) before and after irradiation at  $14.1 \text{ J/m}^2$  for 100 seconds. The OG488 and DNA absorbance are not apparent in this spectra due to the strong absorption profile of the 55 nm AuNP. Samples were prepared and irradiated as described in the Materials and methods section.

before and after irradiation at  $14.1 \text{ J/m}^2$ , demonstrating that irradiation at these pulse radiant exposures does not affect the AuNP shape nor colloidal stability. After irradiation, the samples were centrifuged and the supernatant was carefully collected. Then a fluorescence spectra of the supernatant was taken to extrapolate the amount of

probe DNA released. In Figure 3.7A, the raw fluorescence spectra for AuNPs loaded with Probe65 and irradiated at a pulse radiant exposure of  $14.1 \text{ J/m}^2$  is shown. Each spectrum represents an independent  $200 \mu\text{L}$  aliquot that was irradiated for the specified number of pulses. The bulk heating release (black dashed curve) represents the maximum fluorescence signal obtained during bulk heating (*i.e.*, the max loading of

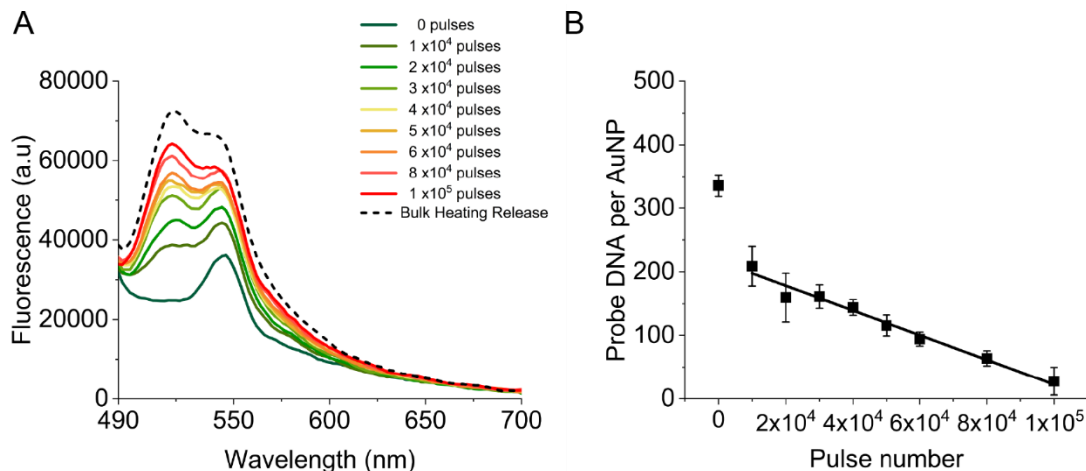


**Figure 3.7:** A) Raw fluorescence data obtained for AuNPs loaded with Probe65 and irradiated at a pulse radiant exposure of  $14.1 \text{ J/m}^2$ . B) Data from A transformed into number of probe DNA per AuNP utilizing the calibration curves in Figure 3.3. Error bars represent std. dev. for  $n = 3$  experiments.

the Probe65 strand). From the fluorescence spectra, it is clear that the amount of probe DNA released into solution increased as the pulse number increased. Using a standard curve (Figure 3.3), the raw data in Figure 3.7A was transformed into the number of probe DNA still hybridized to the template strand on the AuNPs at a given pulse number. It is important to note that the sample is manually removed from the laser path after a specified time that correlates to the specific pulse number and due to the error innate in manual sample removal, the error in the reported pulse number is estimated at  $\leq 1 \times 10^3$  pulses ( $\leq 1$  second). Figure 3.7B shows representative data, obtained from

the raw data in 3.7A, of the amount of Probe65 still hybridized to the template strand on the AuNP as a function of pulse number. The initial drop between the first two data points is discussed in detail below.

To ensure we were only releasing the probe strands into solution and not the whole DNA duplex, we monitored the release of a modified ATTO550-labeled template strand during irradiation. Unlabeled Probe45 was used as the complementary strand in these assays. At our highest pulse radiant exposure ( $14.1 \text{ J/m}^2$ ), we observed a nominal ~6% release of the template strand from the AuNP surface after 100 seconds of irradiation (Figure 3.8). This value was similar to the amount of ATTO550-template

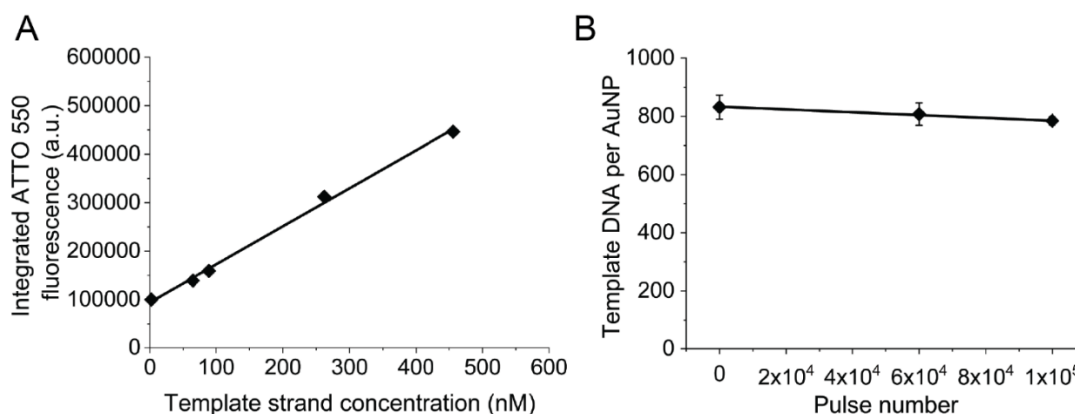


**Figure 3.8:** A) Standardization curve converting the fluorescence of ATTO550 labeled template DNA to concentration of template DNA. Known concentrations of ATTO550 template DNA were measured in a Tecan Infinite M1000 plate reader. ATTO550 was excited at 530 nm and the emission spectra was collected from 550-800 nm. The emission spectra was integrated to obtain the y-axis values. B) Template DNA released using dsDNA-AuNP conjugate with the modified ATTO550-template strand attached to the AuNP at a pulse radiant exposure of  $14.1 \text{ J/m}^2$ . The fluorescence of the released ATTO550 template was converted into the number of DNA per AuNP using the standard curve in A). Error bars represent std. dev. for  $n = 3$  experiments.

DNA released when the dsDNA-AuNP conjugate was incubated at a bulk solution temperature (data not shown) of 80 °C for 2 hours (8%), indicating that the template release occurring in our system during laser excitation is most likely due to the elevated temperatures around the AuNP and not Au-S bond cleavage caused by hot electrons from photoexcitation. This suggests that the released template was non-specifically adsorbed on the AuNP surface and not chemically conjugated through the gold-thiol bond. Conversely, as seen in Figure 3.7B, the Probe65 strand showed complete release after 100 seconds at a pulse radiant exposure of 14.1 J/m<sup>2</sup>, indicating that Probe65 was released through thermal denaturation.

We also controlled for different dsDNA loading densities on the AuNP surface. We examined loading densities of  $14.8 \pm 0.7$  pmol/cm<sup>2</sup> (~832 template strands per AuNP or 1 strand every ~11 nm<sup>2</sup>),  $14.0 \pm 0.6$  pmol/cm<sup>2</sup> (~786 template strands per AuNP or 1 strand every ~12 nm<sup>2</sup>) and  $7.1 \pm 0.5$  pmol/cm<sup>2</sup> (~474 template strands per AuNP or 1 strand every 20 nm<sup>2</sup>) using the Probe55 strand at pulse radiant exposures of 14.1 and 7.1 J/m<sup>2</sup>. No significant difference in the DNA release rate (data not shown) was observed. Surface loading densities of ~7 pmol/cm<sup>2</sup> are considered low and neighboring DNA interactions are considered negligible at these densities.<sup>94</sup> The fact that no changes in the DNA release rate was observed between loading densities, affirms that duplex-duplex interactions were not a considerable factor when considering the DNA release profiles and as such the difference in initial loading of the different probe strands should have had a negligible effect on the results.

Our experimental system contained 3 variables that were each modulated independently: 1) the  $T_m$  of the probe-template dsDNA, 2) the pulse radiant exposure,

and 3) the bulk or bath temperature. We began by testing probe strands with different melting temperatures (Probe45, Probe55, and Probe65) at a fixed pulse radiant exposure of  $14.1 \text{ J/m}^2$  (this being the highest tested pulse radiant exposure), and the corresponding release profiles are shown in Figure 3.9. A two-component DNA release profile during irradiation was observed, an observation that was consistent throughout the study and which will be discussed in depth in the next section. We note that this has also been observed by both Poon *et al.*<sup>48</sup> and Thibaudau *et al.*<sup>50</sup> when using lasers with longer ns pulse widths.

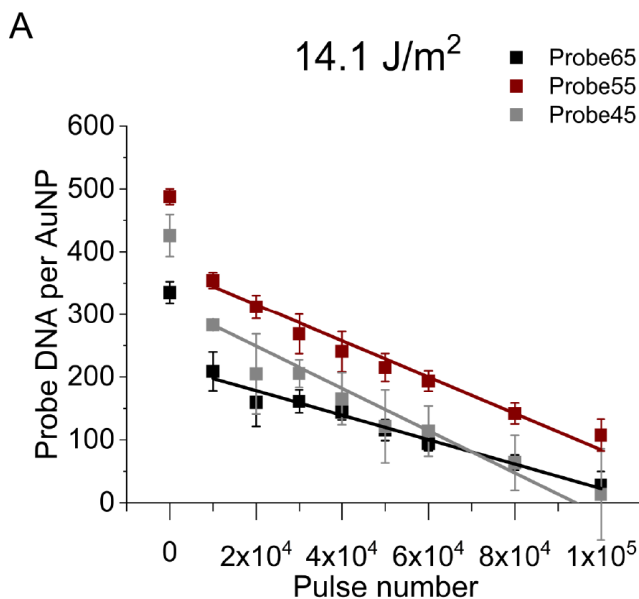


**Figure 3.9:** DNA release as a function of pulse number with the different probe strands at a pulse radiant exposure of  $14.1 \text{ J/m}^2$ . Curves are linear fits of data starting at  $1 \times 10^4$  pulses. Error bars represent std. dev. for  $n = 3$  experiments.

Excluding the initial release of probe DNA during the first  $1 \times 10^4$  pulses, the release profile from subsequent pulses was well fit with a linear function as seen in Figure 3.9. These fits correspond to the largest portion of released DNA (>75%) which also have a higher dissociation energy (*vide infra*) and as such are assumed to be good

representations of the local temperature. Using the slope obtained from the linear fits of the data, the following probe strand release rates were determined; Probe45 releases at  $3.36 \pm 0.37 \times 10^{-3}$  DNA/pulse, Probe55 releases at  $2.89 \pm 0.22 \times 10^{-3}$  DNA/pulse, and Probe65 releases at  $1.94 \pm 0.26 \times 10^{-3}$  DNA/pulse for an incident radiant exposure of  $14.1 \text{ J/m}^2$ . Reported uncertainties arise from averaging triplicate measurements. As predicted, a lower DNA melting temperature corresponds to a faster DNA release rate during irradiation and is further evidence that the probe DNA is released through thermal denaturation.

Subsequently, the assorted dsDNA-AuNP conjugates were irradiated at varying laser pulse radiant exposures including 3.5, 7.1, 10.5, and  $14.1 \text{ J/m}^2$ . The corresponding release profiles are shown in Figure 3.10. Reported uncertainties arise from triplicate measurements (not necessarily of the same sample batch). Quantification results are summarized in Table 3.2. For each probe strand, the DNA release rate was dependent on the pulse radiant exposure, where the larger pulse radiant exposures corresponded to faster DNA release rates. At pulse radiant exposures of 7.1, 10.5 and  $14.1 \text{ J/m}^2$ , the DNA release rate was dependent on the melting temperature of the probe strand, *i.e.*, the lowest melting temperature probe strand, Probe45, released the quickest at these pulse radiant exposures compared to that of Probe55, while Probe65 was even slower. At the pulse radiant exposure of  $3.5 \text{ J/m}^2$ , the DNA release was minimal and in line with the observed release rates for the ATTO550-template control experiments. To further ensure that there were no collective heating effects, control experiments were realized in which the samples were further diluted by 50% (representative data referred

to as half [C] shown in Figure 3.10B) and the release rate was found to be unmodified from the full concentration samples.

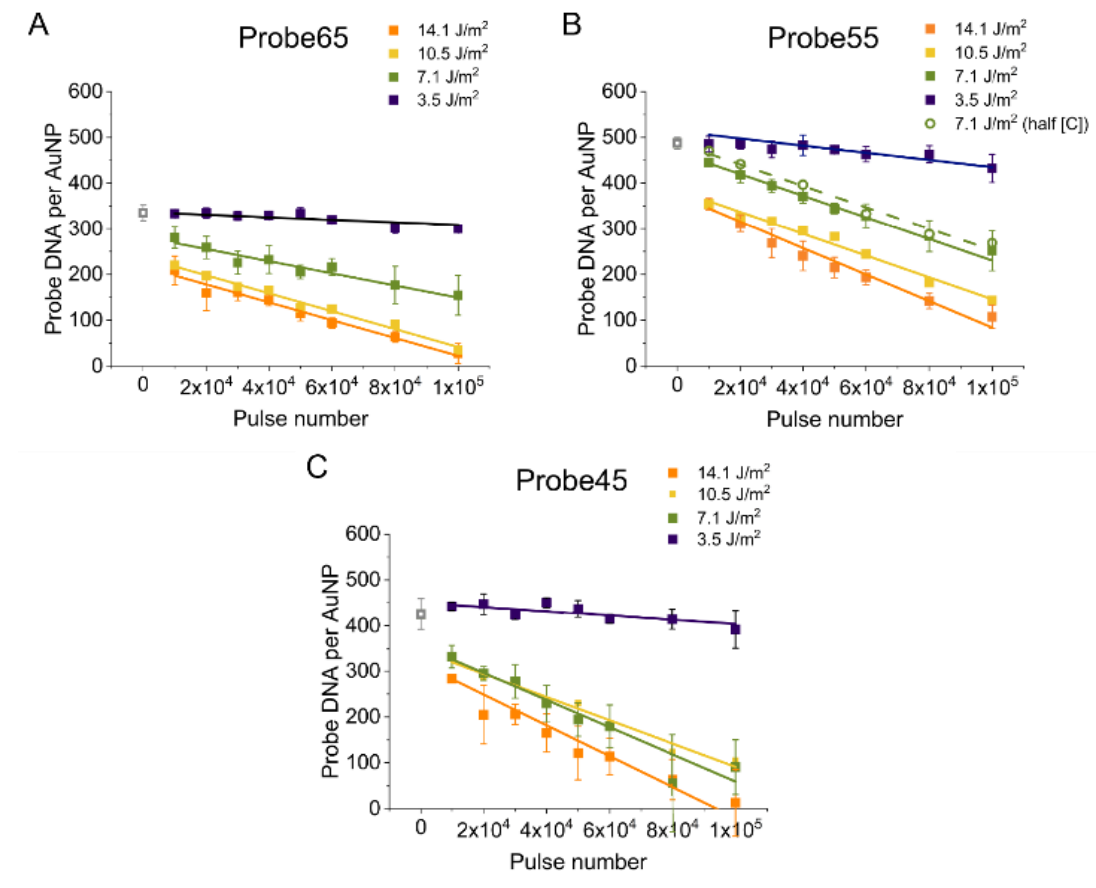


**Figure 3.10:** DNA release as a function of pulse number for A) Probe65, B) Probe55, and C) Probe 45 at varying pulse radiant exposures. In B), the empty light green circles-dotted line, (7.1 J/m<sup>2</sup> (half [C])), is a sample run at 2-fold dilution of the other samples to demonstrate that there are no collective heating effects. All data sets in each panel share the same initial number of DNA before laser heating (hollow grey square). Curves are linear fits of data starting at  $1 \times 10^4$  pulses. Error bars represent std. dev. for  $n = 3$  experiments.

Finally, we irradiated dsDNA-AuNP conjugates while controlling the bulk solution temperature using a temperature controlled cuvette holder. By lowering the bulk solution temperature, we were able to decrease the DNA release rate at a given pulse



radiant exposure, as the temperature increase provided by the laser pulse had the same magnitude, yet the effective solution temperature around the DNA was lower. We held the bulk solution temperature at 6, 12, and 22 °C and irradiated the various dsDNA-AuNP conjugates at pulse radiant exposures of 7.1 and 14.1 J/m<sup>2</sup> (Figure 3.11).

Pulse radiant exposure	3.5 J/m <sup>2</sup>	7.1 J/m <sup>2</sup>			10.5 J/m <sup>2</sup>	14.1 J/m <sup>2</sup>		
Bath temperature	22 °C	6 °C	12 °C	22 °C	22 °C	6 °C	12 °C	22 °C
Probe DNA release rate (x10 <sup>-3</sup> strands/pulse)								
Probe 65	0.28 ± 0.01	0.62 ± 0.08	0.66 ± 0.04	1.33 ± 0.38	1.95 ± 0.10	0.54 ± 0.05	0.77 ± 0.02	1.94 ± 0.26
Probe 55	0.78 ± 0.17	0.98 ± 0.15	1.23 ± 0.14	2.37 ± 0.25	2.38 ± 0.13	1.05 ± 0.11	1.54 ± 0.19	2.89 ± 0.22
Probe 45	0.47 ± 0.21	0.98 ± 0.84	1.97 ± 0.19	2.96 ± 0.54	2.53 ± 0.20	0.58 ± 0.20	3.21 ± 0.15	3.36 ± 0.37

**Table 3.2:** Probe DNA release rates. Probe DNA release rate is the slope of the linear fit of the release data starting at  $1 \times 10^4$  pulses. Error represents std. dev. for  $n = 3$  experiments.

For Probe65, we observed a significant decrease in the DNA release rate (>50%) when the solution temperature is lowered to 12 °C. Interestingly, we did not observe any additional reduction of the DNA release rate when the solution temperature is further lowered to 6 °C, indicating that when dropping the bath temperature by 10 °C the  $\Delta T$  increase around the AuNP caused by the laser pulse no longer reached a temperature capable of releasing Probe65. For Probe45, we observe a decrease in the release rate at each stage of reduction in solution temperature; ~66% from 22 °C to 12 °C and ~50% from 12 °C to 6 °C at a pulse radiant exposure of 7.1 J/m<sup>2</sup>. The decrease in the DNA release rate at cooler bulk solution temperatures, provides further evidence that we were controllably heating the DNA to temperatures in the range of the duplex melting

temperatures (40-70 °C). In Table 3.2, the probe DNA release rates at the three solution temperatures are presented for experiments realized at 14.1, 7.1 and 3.5 J/m<sup>2</sup>.

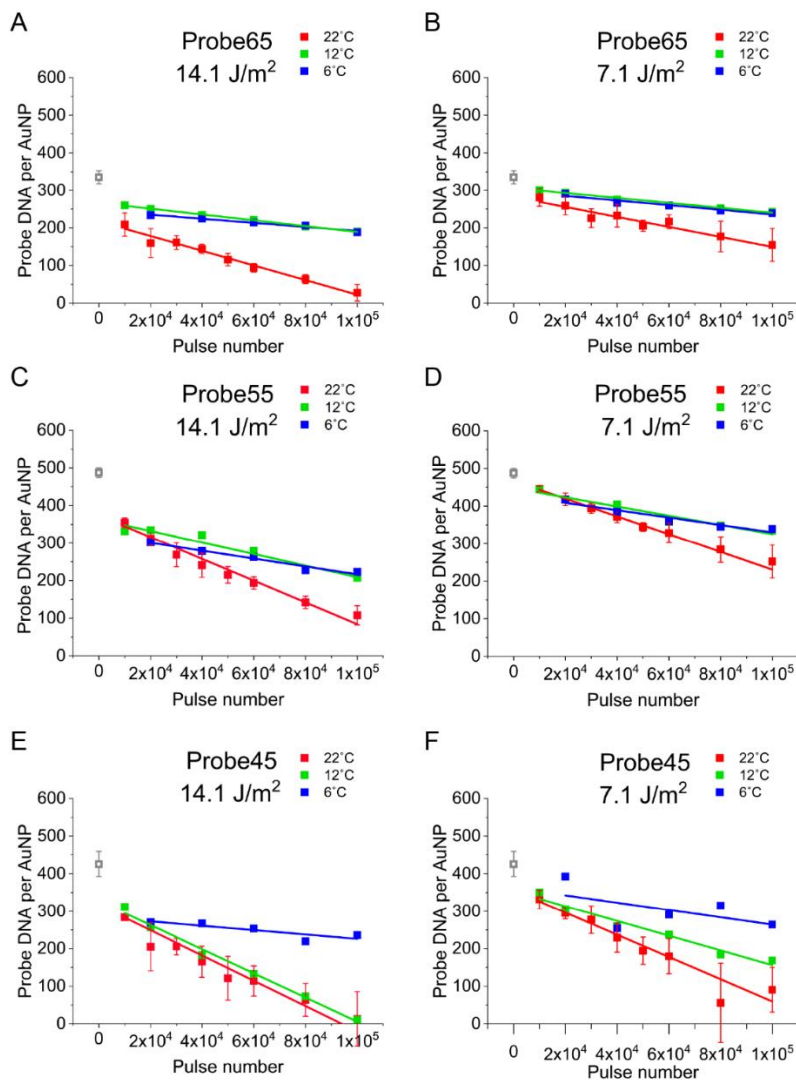


**Figure 3.11:** DNA release as a function of pulse number at varying bath temperatures for A) Probe65 at a pulse radiant exposure of 14 J/m<sup>2</sup>, B) Probe65 at a pulse radiant exposure of 7 J/m<sup>2</sup>, C) Probe55 at a pulse radiant exposure of 14 J/m<sup>2</sup>, D) Probe55 at a pulse radiant exposure of 7 J/m<sup>2</sup>, E) Probe45 at a pulse radiant exposure of 14 J/m<sup>2</sup>, and F) Probe45 at a pulse radiant exposure of 7 J/m<sup>2</sup>. All data sets share the same initial number of DNA (hollow grey square). Curves are linear fits of data starting at 1 x 10<sup>4</sup> pulses. Error bars represent std. dev. for n = 3 experiment.

### 3.2.4 Quantification of locally sensed temperature

Utilizing the obtained data sets, the results were analyzed in detail to better understand the nanolocalized heating profile sensed by the DNA both in time and space after a fs-laser pulse induced heating event. To do this the equations developed for a steady-state bulk heating condition of DNA denaturation on AuNPs were applied with a key variation, our system is not at equilibrium but instead is an average of non-equilibrium states over time, *i.e.*, a pulse occurs and the AuNP is heated, the heat dissipates to the local environment containing the DNA, the system cools down to the bulk solution temperature during the 1 ms between successive pulses, and then the reaction repeats itself but for the next pulse the starting point is a AuNP with fewer probe DNA hybridized to the template strands on the AuNP surface. That there was no observed DNA rebinding during the bulk heating assays provided confidence in this assumption. It is important to distinguish the difference between rebinding post probe strand diffusion from the AuNP and rebinding while the probe strands are still associated with the template-AuNP. We observe no rebinding once the probe DNA diffuses into solution, but are unable to determine if rebinding occurs while the probe strand is still associated with template strand, *e.g.*, the DNA bases are unpaired or only partially unpaired but the probe strand has not yet diffused into solution and rebinds to the template strand.

The system has an additional intricacy, as noted, for any experiment with noticeable release (*i.e.*, above 3.5 J/m<sup>2</sup> pulse radiant exposure), the system presented a two-component release profile as briefly mentioned in the previous section. To explain this result we refer to the work of Chen *et al*, where it was shown that a DNA duplex

immobilized to the surface of a AuNP will adopt minimally two conformations on the AuNP surface and these conformations lead to distinct dissociation constants.<sup>94</sup> One of these conformations leads to a faster dissociation constant, while the other leads to a slower dissociation constant. We note that although the exact physical description of the conformations is still unknown, it is predicted that the duplex configuration with the faster dissociation constant is due to the formation of partial duplexes caused by interactions with the Au surface.<sup>94</sup> The thermally induced biphasic release of DNA on AuNPs has also been observed in other studies.<sup>48, 84</sup> As an example, during the first ten seconds of irradiation at 14.1 J/m<sup>2</sup>, we observed the release of a large number of each probe strand;  $143 \pm 34$ ,  $133 \pm 18$  and  $127 \pm 35$  for Probe45, Probe55, and Probe65 respectively (see Figure 3.9); similar results were seen in the other experimental conditions. We propose that a majority of the probe DNA released during the first  $1 \times 10^4$  pulses had a faster dissociation constant due to interactions with the Au surface and/or improper hybridization. Therefore, it is appropriate to modify the equation for DNA dissociation used in the current analysis so that it accounts for the quick release observed in the subspecies of probe DNA that is interacting with the Au surface (less than 25% of total probe DNA) as well as the major species of probe DNA that does not strongly interact with Au surface and is said to have a “slow” dissociation constant.

Following the work of Chen *et al.*,<sup>16</sup> ( $\chi$ ) is designated as the total amount of DNA duplexes on the AuNP surface:

$$\chi = \sum \chi^i \quad (\text{Eq. 3.1})$$

Where  $\chi^i$  is representative of each DNA conformation on the AuNP. A two component system is sufficient in this case, represented by  $f$  = fast and  $s$  = slow. As such:

$$\chi = \chi^f + \chi^s \quad (\text{Eq. 3.2})$$

Each duplex component ( $\chi^f$  or  $\chi^s$ ) has a dissociation curve that can then be fit to the following equation:

$$\chi^i = \chi_0^i * e^{-k_d^i t} \quad (\text{Eq. 3.3})$$

Where  $\chi_0$  is the initial number of DNA duplexes in the specific component,  $k_d$  is the dissociation rate of duplexes in the specific component and  $t$  is time. The dissociation rate can then be written as:

$$k_d^i = \kappa \frac{kT}{h} e^{(-\frac{\Delta H_d^{i,\ddagger}}{RT})} e^{(\frac{\Delta S_d^{i,\ddagger}}{R})} \quad (\text{Eq. 3.4})$$

where  $T$  is temperature,  $R$  is the ideal gas constant,  $k$  is Boltzmann's constant,  $h$  is Planck's constant,  $\kappa$  is the transmission coefficient, which was assumed to have a value of 1.<sup>94, 101-102</sup>  $\Delta H_d^\ddagger$  is the activation enthalpy and  $\Delta S_d^\ddagger$  is the activation entropy. Activation entropy is the change in entropy of the DNA when moving from the duplex state to the denatured state and activation enthalpy is the change in enthalpy of the DNA when moving from the duplex to denatured state. It is important to note that each duplex component ( $\chi^f$  or  $\chi^s$ ) in this system has a distinct activation enthalpy and activation entropy. The pulsed heating effect in this system (Figure 3.12D) was further simulated using a previous published MATLAB code.<sup>85</sup> Using these simulated temperature profiles we empirically determined that the heating duration ( $t$ ) after a

single pulse was approximately 5 ns. Thus, after a single laser pulse, Equation (3.3) can be rewritten as:

$$\chi_1 = \chi_0 * e^{-k_d(5 \text{ ns})} \quad (\text{Eq. 3.5})$$

Subsequently, the AuNP and local environment return to ambient temperature before the next pulse arrives. Then, a second pulse arrives and heats the AuNP and local environment for another 5 ns as given by:

$$\chi_2 = \chi_1 * e^{-k_d(5 \text{ ns})} \quad (\text{Eq. 3.6})$$

And for the Nth pulse the dissociation curve can be written as:

$$\chi_N = \chi_0 \prod_{j=1}^N (e^{-k_d(5 \text{ ns})})^j = \chi_0 * e^{-k_d(5 \text{ ns})(N)} \quad (\text{Eq. 3.7})$$

Substituting equation (3.7) into equation (3.1) for both the fast and slow DNA components yields:

$$\chi = [\chi_0^f * e^{-k_d^f(5 \text{ ns})(N)}] + [\chi_0^s * e^{-k_d^s(5 \text{ ns})(N)}] \quad (\text{Eq. 3.8})$$

Equation 3.8 was used to fit the raw data collected during our pulsed release experiments. The results of the fits can be seen in Figures 3.12A-C.

As we are primarily interested in fitting for  $T$ , substituting the dissociation rate equation (Equation 3.4) into the  $k_d$  values for each DNA component in Equation 3.8, allowed us to directly output a  $T$  value from the fit of each data set and ensure the  $T$  values obtained were identical in the slow and fast DNA components. Additionally, this allowed us to independently input thermodynamic values for each DNA component

in the range of 32-49 kcal/mol for  $\Delta H_d^\#$  and 0.06-0.11 kcal/mol\*K for  $\Delta S_d^\#$ , which are

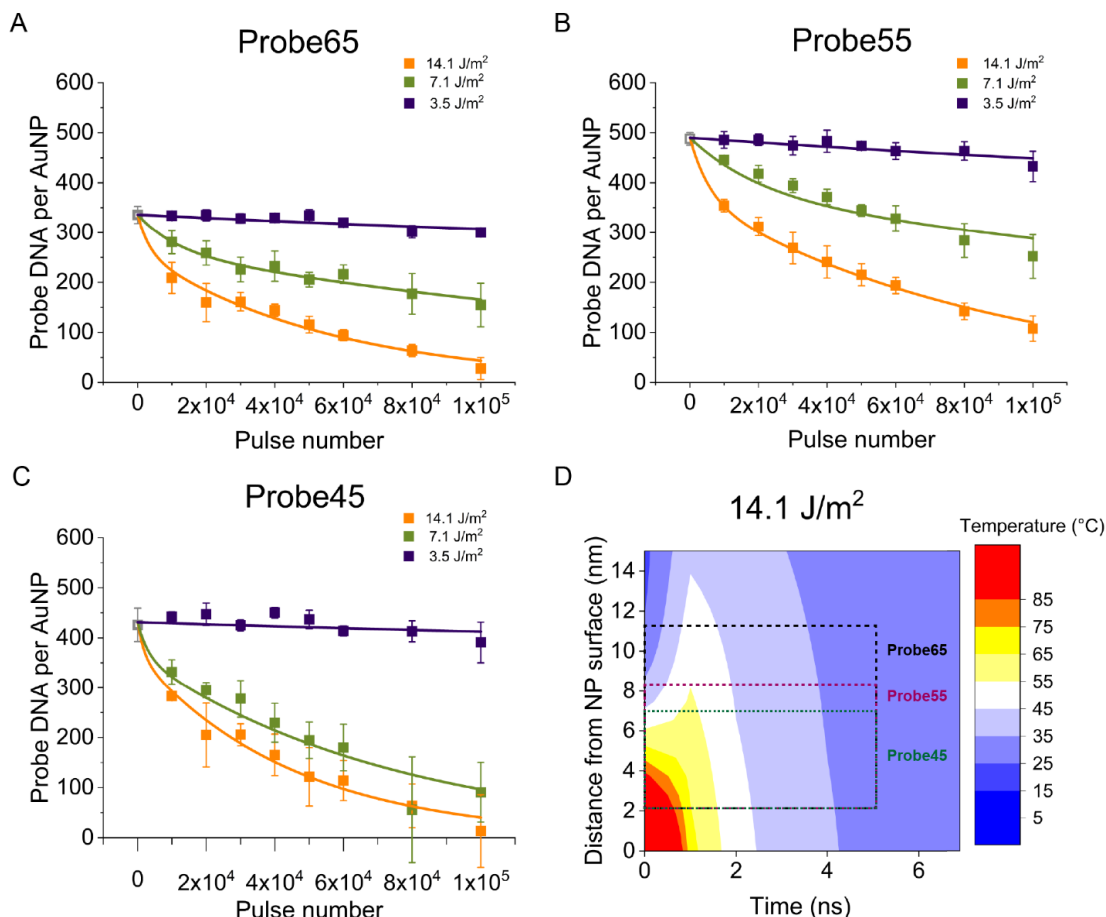


**Figure 3.12:** Probe DNA per AuNP and a function of pulse number for pulse radiant exposures of 14.1, 7.1 and 3.5 J/m<sup>2</sup> for Probe65 (A), Probe55 (B), and Probe45 (C). Fit curves were obtained using Equation 3.8. D) 2-D data set of simulated heat profile around a AuNP after a single laser pulse at 14.1 J/m<sup>2</sup>. The dashed rectangles (black-Probe65, maroon-Probe55, green-Probe45) represent the area used to determine the average temperature ‘sensed’ across the respective probe strand in a 5 ns time window. Each probe strand was estimated to start at approximately 2.1 nm from the AuNP surface and extend throughout the height of the respective dashed rectangle.

consistent with values reported in the literature for similar length DNA strands dissociating on an AuNP surface during bulk solution heating.<sup>94</sup> For each DNA strand the  $\Delta H_d^\#$  and  $\Delta S_d^\#$  values were kept the same regardless of the experimental conditions

and the values used in our fitting ensured that the longer the probe DNA strand the greater the energy barrier for dissociation. The  $\Delta H_d^\ddagger$  and  $\Delta S_d^\ddagger$  values we used for the probe DNA strands are reported in Table 3.3. Similarly the percentage of fast and slow DNA components was kept fixed throughout every fitting, however it was dependent on the particular probe DNA strand. The fast component composed 15%, 24%, and 22% for Probe45, Probe55, and Probe65, respectively, in line with values of 10-20% reported in the literature for the fast DNA configuration.<sup>94</sup> While we did not directly fit  $k_d$ , it was derived using the  $\Delta H_d^\ddagger$  and  $\Delta S_d^\ddagger$  values as well as the  $T$  value obtained from the fittings. We report  $\ln(k_d)$  values over the range of 6.5-10.9 for the fast DNA component and 3.2-8.1 for the slow DNA component, which are similar to what has been previously reported for bulk solution heating on AuNPs.<sup>94</sup>

		Probe65	Probe55	Probe45
Component with "slow" dissociation rates	Proportion	78%	76%	85%
	$\Delta H_d^\ddagger$ (kcal mol <sup>-1</sup> )	49	37	37
	$\Delta S_d^\ddagger$ (kcal mol <sup>-1</sup> K <sup>-1</sup> )	0.11	0.072	0.07
Component with "fast" dissociation rates	Proportion	22%	24%	15%
	$\Delta H_d^\ddagger$ (kcal mol <sup>-1</sup> )	44	33	32
	$\Delta S_d^\ddagger$ (kcal mol <sup>-1</sup> K <sup>-1</sup> )	0.1	0.065	0.06

**Table 3.3:** Parameters used for data fitting with the modified DNA dissociation equation. Parameters used to obtain “sensed” temperature values from fitting data with Equation 3.8.  $\Delta H_d^\ddagger$  is the activation enthalpy and  $\Delta S_d^\ddagger$  is the activation entropy. Error on all values was  $\leq 5\%$ .

The value of  $T$  obtained from the fits quantifies the *sensed* temperature for a specific probe DNA at a given pulse radiant exposure and bulk solution temperature. We use the term *sensed* as it represents a time and length temperature average around



the DNA, since the temperature is not uniform over time or distance in our system. In the context of DNA denaturation, we expect the *sensed* temperature to represent the bulk steady-state temperature that would impose similar DNA dissociation rates. We averaged the *sensed* temperature values ( $T$ ) obtained from the three probe DNA strands at pulse radiant exposures of 14.1, 7.1, and 3.5 J/m<sup>2</sup> for a bulk solution temperature of 22 °C. Additionally we calculated an average *sensed* delta temperature ( $\Delta T$ ) by subtracting out the respective bulk solution temperature so that we could determine the average *sensed* delta temperature at a given pulse radiant exposure. The *sensed*  $\Delta T$  value represents the average delta temperature from all three probe strands at all bath temperatures for a specific laser pulse radiant exposure. The obtained *sensed* temperatures ( $T$ ) and *sensed* delta temperature increases ( $\Delta T$ ) are presented in Table 3.4.

To physically interpret the *sensed* temperatures in this system, the temperature profile around a single AuNP was simulated after a single pulse at each radiant exposure used. Simulations were carried out using MATLAB code published by the Baffou lab.<sup>85</sup> It is important to note that when using 55 nm AuNPs in conjunction with a 1 kHz laser repetition rate, we were in a time-localization regime,<sup>27</sup> meaning there was no temperature accumulation in the system between successive pulses; the AuNP and surrounding medium return to the solution baseline temperature before another pulse is absorbed. Furthermore, at the low concentration in our system (13 pM) each AuNP was approximately 5  $\mu$ m from neighboring particles and individual AuNPs could be said to be in the temperature confinement regime when used with our laser parameters.<sup>27</sup> As such, the simulated temperature profile around the AuNP after a single

pulse could be used to model the temperature increase around the probe DNA. An example of the theoretical heat maps produced, shown for 14.1 J/m<sup>2</sup> at RT is presented in Figure 3.12D. Using these theoretical temperature profiles, we empirically determined that a majority of the temperature increase occurs within the first 5 ns and as such this was chosen as the heating duration for the pulsed release equation used in our fits. To interpret the fit *sensed* temperature, the average theoretical temperature across the physical extension of the DNA strands were calculated over a 5 ns time window. These values, reported in Table 3.4 as Model  $\langle T \rangle$ , are an average of the temperatures felt across each probe strand at a given pulse radiant exposure. The dashed rectangles (black-Probe65, maroon-Probe55, green-Probe45) in Figure 3.12D

Pulse radiant exposure (J/m <sup>2</sup> )	<i>Sensed</i> Temperature <sup>a</sup> (°C)	Model $\langle T \rangle$ <sup>b</sup> (°C)	<i>Sensed</i> $\Delta T$ <sup>c</sup> (°C)
14.1	48.3 ± 1.5	47	31.0 ± 3.6
7.1	43.0 ± 3.6	34	26.0 ± 4.3
3.5	24.3 ± 5.0	28	2.3 ± 5.0

**Table 3.4:** Quantification of local temperature around AuNP after photothermal heating event at different laser pulse radiant exposures. <sup>a</sup>Average value of  $T$  from Probe65, Probe55, and Probe45 at RT (bath = 22 °C) obtained from the fit data using Equation 3.8. <sup>b</sup>Average model temperature at a bath temperature of 22 °C obtained from MATLAB simulations. The average model temperature is the average temperature along the length of the probe DNAs over a 5 ns heating interval after a pulse at the respective radiant exposure. <sup>c</sup>Average  $\Delta T$  from the fits of all probe strands and all bath conditions obtained by subtracting the bath temperature from the *sensed* temperature at the specific laser pulse radiant exposure.

represent the area used to determine the average temperature for each probe strand and the Model  $\langle T \rangle$  is an average of these three temperatures. The *sensed* temperature is in

good agreement with the 5 ns model average for 14.1 and 3.5 J/m<sup>2</sup>, while overestimating the temperature for 7 J/m<sup>2</sup>. This overestimation of the *sensed* temperature leads us to believe that the temperature gradient across the length of the DNA as well as the local max temperature play a considerable role in DNA denaturation (discussed further in Chapter 4). Additionally, our results point very strongly to a single-pulse stochastic driven release rather than a gradual cumulative release. As the heating timescale after a single pulse is on the order of ns and the time between successive pulses is 1 ms, we can safely assume the temperature of the local environment around the AuNP returns to baseline after each pulse. Both this and the good fit of our data to the modified pulsed release equation (Equation 3.8) provide strong evidence towards stochastic release. Moreover, the linear fitting of the ‘slow’ release component opposes a cumulative effect as we would expect the release rate to increase at longer pulse.

### **3.3 Conclusions**

Overall, we find that when operating under the proper experimental conditions, fs-pulse excitation of AuNPs can be used to thermally denature dsDNA displayed on the AuNP surface without causing significant cleavage of the gold-thiol bond used for DNA attachment. This is an important finding, as we have demonstrated that the gold-thiol bond is a viable attachment chemistry for placing biological molecules on AuNPs during fs-pulsed heating with pulse radiant exposures at or below 14.1 J/m<sup>2</sup>. Additionally, we observed no bulk solution temperature increase from AuNP heat dissipation, providing further evidence that each AuNP is in a spatio-temporal temperature confinement regime in the experimental configuration we utilized.<sup>27</sup> This

work demonstrates that the rate of DNA release under fs-pulse heating can be correlated to the DNA length or  $T_m$  and can be tuned by controlling both the pulse radiant exposure and the bulk solution temperature. After fs-pulse absorption, the theoretical temperature increase around the AuNP can last for as little as 5 ns and the theoretical temperature profile follows a  $1/r^3$  temperature dependence extending from the AuNP surface.<sup>103</sup> This creates an interesting distinction from that of steady state heating or bulk solution heating when considering biological materials such as DNA, since the temperature profile around the AuNP generated from fs-pulse absorption changes drastically on the nanosecond time and nanometer length scales. To better understand how DNA reacts to the temperature profile generated from fs-pulse heating, we modified the equations describing the steady-state DNA dissociation on AuNPs<sup>94</sup> to account for the pulsed laser heating. Our data was well fit using the derived pulsed-modified dissociation equations and allowed us to extract thermodynamic properties of the dsDNA attached to AuNP. Of perhaps greater interest, a “*sensed*” temperature value was derived, providing a quantitative local nanothermometer for fs-pulsed heating in coordination with biological systems. We designate this a *sensed* temperature as the temperature profile is not uniform over time or even along the DNA as it extends from the AuNP surface. Temperature profile simulations were used to better understand the fit *sensed* temperature value and we found that the theoretical average temperature over the physical extension of the probe DNA for a 5 ns time window after pulse absorption matched closely to the *sensed* temperature for two of the three pulse radiant exposures examined (14.1 and 3.5 J/m<sup>2</sup>). For a pulse radiant exposure of 7.1 J/m<sup>2</sup>, the *sensed* temperature is 9 °C higher than the model average temperature, indicating that local

peak or maximum temperatures may play a larger part in the denaturation process. Overall we have demonstrated that when both the laser system and AuNP colloidal suspension are properly designed, fs-pulsed heating of AuNPs can be used to generate highly local temperature increases in a biologically relevant range, and the magnitude of the temperature increase can be controlled to modulate relevant biological activity.

### ***3.4 Materials and methods***

#### *3.4.1 AuNP synthesis*

AuNPs were synthesized as previously described.<sup>104-105</sup> Briefly, 55 nm diameter AuNPs were synthesized in aqueous phase by using a seeded growth method in the presence of citric acid and ascorbic acid. 10 nm seed AuNPs were first synthesized using sodium citrate and NaBH<sub>4</sub>. The seeds were then added to a growth solution of 0.4 mM HAuCl<sub>4</sub> and 0.8 mM sodium citrate in 50 mL of deionized water. Then *L*-ascorbic acid was added to the solution to make a final concentration of 2 mM. The reaction was stirred for 2 hours at room temperature and then kept at room temperature for 24 hours. The completion of the reaction was confirmed by UV-Vis absorption spectroscopy by measuring the AuNP surface plasmon resonance band's red shift (from 515 nm to 531 nm) and the decrease of the ascorbic acid peak in the UV region. The size of the AuNP,  $55 \pm 5$  nm, was confirmed using transmission electron microscopy (TEM).

#### *3.4.2 DNA conjugation and quantification*

DNA sequences were purchased from Integrated DNA Technologies Inc. (Coralville, IA). The probe DNA strands were purchased with a 3' amino modification

and conjugated in-house with Oregon Green 488 Carboxylic Acid, Succinimidyl Ester, 5-isomer (OG488) purchased from ThermoFisher Scientific (Waltham, MA) using the amine-reactive probe labeling protocol described on <https://www.thermofisher.com/us/en/home/references/protocols/cell-and-tissue-analysis/labeling-chemistry-protocols/amine-reactive-probe-labeling-protocol.html>. Probe strands were then purified using PD-10 Columns (GE Healthcare) and/or Ultra-High Performance Liquid Chromatography (UHPLC).<sup>106</sup> The template strand and the desired probe strand at equimolar 0.05 mM concentration were combined into a solution of 100 mM HEPES pH 7.5 with 5 mM MgCl<sub>2</sub>. This solution was thermally annealed using a thermocycler (Applied Biosystems ProFlex PCR System) by heating up to 85 °C followed by controlled cooling at 1 °C per minute. Samples were then stored at 4 °C or immediately used. The probe-template dsDNA were incubated with Tris (carboxyethyl) phosphine hydrochloride (TCEP) at a molar ratio of 1:100 for 30 minutes to reduce the thiol bond. AuNPs were added to the activated dsDNA at a ratio of 1:2,000 in a solution of 50 mM HEPES pH 7.5 with 0.5 mM MgCl<sub>2</sub>. The solution was stirred at room temperature overnight. The final solution was then concentrated and rinsed to remove unbound DNA using Amicon ultracentrifugation columns with a molecular weight cutoff of 100 kDa. To quantify the amount of probe DNA attached to the AuNP, a portion of the AuNP-dsDNA solution was heated to 80 °C for 2 hours. This temperature was expected to dehybridize and release into solution all the hybridized probe strands. The solution was then centrifuged at 5,000 x g for 5 minutes and the supernatant was collected to quantify the amount of released probe DNA. A standard curve was then used to convert fluorescence intensity to moles of DNA.

To quantify template DNA attached to the AuNP, we used a modified template strand displaying an ATTO 550 fluorescent dye. The dsDNA attachment to the AuNP was performed as described above except an unlabeled Probe45 strand was utilized. Following a previously published protocol,<sup>93</sup> an excess of mercaptoethanol (10,000 times the Au concentration) was added to the AuNP-dsDNA conjugate solution and the reaction was allowed to proceed overnight. The solution was then centrifuged at 5,000 x g for 5 minutes and the supernatant collected to quantify the amount of template DNA. A standard curve was used to convert fluorescence intensity to moles of DNA.

#### *3.4.3 Experimental set up of bulk heating assays*

For the melting curves “off” of the AuNP (*i.e.*, dsDNA probe alone), we used a modified template strand containing a 5' Iowa Black®FQ Dark Quencher. To measure the melting curves, a 1:1 solution at 5 nM of the template strand and each probe strand were annealed to form DNA duplexes. Each DNA duplex was then placed in a temperature controlled fluorometer cuvette, where the bulk solution temperature was raised from 20 °C to 80 °C at 1 °C per minute. The temperature sensitivity of OG488 fluorescence was determined and incorporated into the melting curves. With every 2 °C change, a fluorescence reading was taken. The fluorescence intensity at each temperature was converted to the fraction of ssDNA present in solution by using the 20 °C fluorescence readout as the 0.0 ssDNA state and the 80 °C fluorescence readout as the 1.0 ss DNA state. The melting curves for the DNA duplexes “on” the AuNP were obtained in similar manner but the fluorescence intensity was converted to percent DNA released.  $T_m$  values were obtained by taking the temperature corresponding to maximum of the first derivative of the melting curves.

#### *3.4.4 Experimental set up of fs-pulse laser assays*

The pulsed laser heating assays are as described in the text. Samples were irradiated for a set amount of time, measured manually, and then transferred to a microcentrifuge tube. The sample was then centrifuged at 5,000 x g for 5 minutes and the supernatant was collected. The fluorescence spectra of the supernatant was measured using a Tecan Infinite M1000 plate reader and a standard curve was used to quantify the amount of probe or template DNA released from the AuNP. The OG488 was excited at 465 nm and the fluorescence spectra was collected from 480 nm to 700 nm. For kinetic studies, each time point represents a discrete sample. To ensure that the temperature increase was a local effect around the AuNPs and not due to an increase in the bulk solution temperature, the solution temperature was monitored with a thermocouple during the laser assays. A temperature controlled cuvette holder was used to control the bulk solution temperature.

#### *3.4.5 Temperature profile simulations*

Origin software (OriginLab, Northampton, MA) was used to generate all fittings. For the linear fits, the initial data point was not included in the fits. A custom function was created in Origin to fit the data to the pulsed-DNA dissociation equation (Equation 3.8). In order to simplify the fits, we examined all the simulated temperature profiles and determined that a 5 ns heating time was representative of the heating duration around the DNA after a single pulse. We also fit the data using 10 ns and 3 ns heating times but found the data was best fit to the 5 ns heating time. The MATLAB code used to simulate the temperature profile around a AuNP after a single fs-laser pulse was



published in Ref.<sup>85</sup> The governing equations for the MATLAB code are described in detail in Ref.<sup>103</sup> The temperature profile for each pulse radiant exposure and solution temperature were determined using a 28 nm AuNP radius, 387.5 nm pulse wavelength, 150 fs pulse width and an interface conductance value of  $300 \times 10^6 \text{ W/m}^2\text{K}$ . The interface conductance value was chosen as it is similar to AuNP-ligand interface conductance values reported in the literature.<sup>107-109</sup>

## **Chapter 4: Mechanistic Understanding of DNA Denaturation in Nanoscale Thermal Gradients Created by Femtosecond Excitation of Gold Nanoparticles<sup>#</sup>**

<sup>#</sup>Currently submitted to *ACS Applied Materials and Interfaces*.

### ***4.1 Introduction***

In Chapter 3, our work demonstrated indirect control over dsDNA denaturation rates on AuNPs under fs laser pulse irradiation by varying the dsDNA melting temperature, bulk solution temperature and laser pulse radiant exposure. Using these “control levers”, we were able to modulate the local temperature average along the dsDNA over the biological relevant range of 8-53 °C without increasing the temperature of the bulk solution. Furthermore, the “pulsed-heating” modified dissociation equation model we developed to describe this process allowed us to extract a “sensed” temperature and compare it with the theoretical temperature around the AuNP. From this model we found that the sensed temperature is typically greater than the theoretical average temperature, suggesting that the local peak or maximum temperature plays a significant role in the denaturing process. This finding was supported by the local temperature profile which follows a  $\sim r^{-3}$  dependence from the AuNP surface,<sup>36</sup> placing the dsDNA in an exceptionally steep thermal gradient. The steep dependence of the temperature profile on the distance from the AuNP surface makes this space a key variable in creating the optimal nanoenvironment for biological moieties whose activity is controlled by temperature under the current functional scenario.

In the above studies, two key questions about DNA dehybridization following fs-laser pulse excitation of AuNPs remained unanswered. First, the mechanism and timescale of DNA dehybridization in nanoscale thermal gradients remained unknown. Second, the influence of the peak or maximum temperature near the AuNP surface on the DNA dehybridization was also unclear. To address these two questions, as well as improve the control over dsDNA denaturation rate from fs-laser pulse heating of AuNPs, we designed dsDNA-coated AuNPs with varying distances between the dsDNA and AuNP surface. Using a 19 bp dsDNA domain, we systemically increased the distance between the dsDNA and the AuNP surface by adding in poly-thymine (T) spacers of different lengths. A schematic of this system is shown in Figure 4.1A,B. Although the distance from the AuNP surface is only varied by approximately 3.8 nm in total, with 1.1 nm intervals, this small shift in distance changes the predicted maximum temperature that the dsDNA is exposed to by  $\sim 43$  °C, with the interval change increment as large as  $\sim 19$  °C. We report that as the distance between the dsDNA and AuNP surface is increased, the DNA dehybridization rate decreases. By extending the dsDNA  $\sim 3.8$  nm into solution and decreasing the pulse radiant exposure from  $14.1 \text{ J/m}^2$  to  $7.1 \text{ J/m}^2$ , the total amount of DNA released into solution was reduced from of 93% to 26% in only 100 seconds of irradiation. It is estimated that the average dsDNA dehybridization rate is modified by up to  $30 \pm 2\%$  by shifting the dsDNA position by as little as  $\sim 1.1$  nm, thus providing a higher level of control over DNA release.

To address the mechanistic question underpinning these processes and provide insight into dsDNA melting in the presence of nanoscale heat gradients *versus* the steady-state temperature conditions, we developed a distinct computational approach

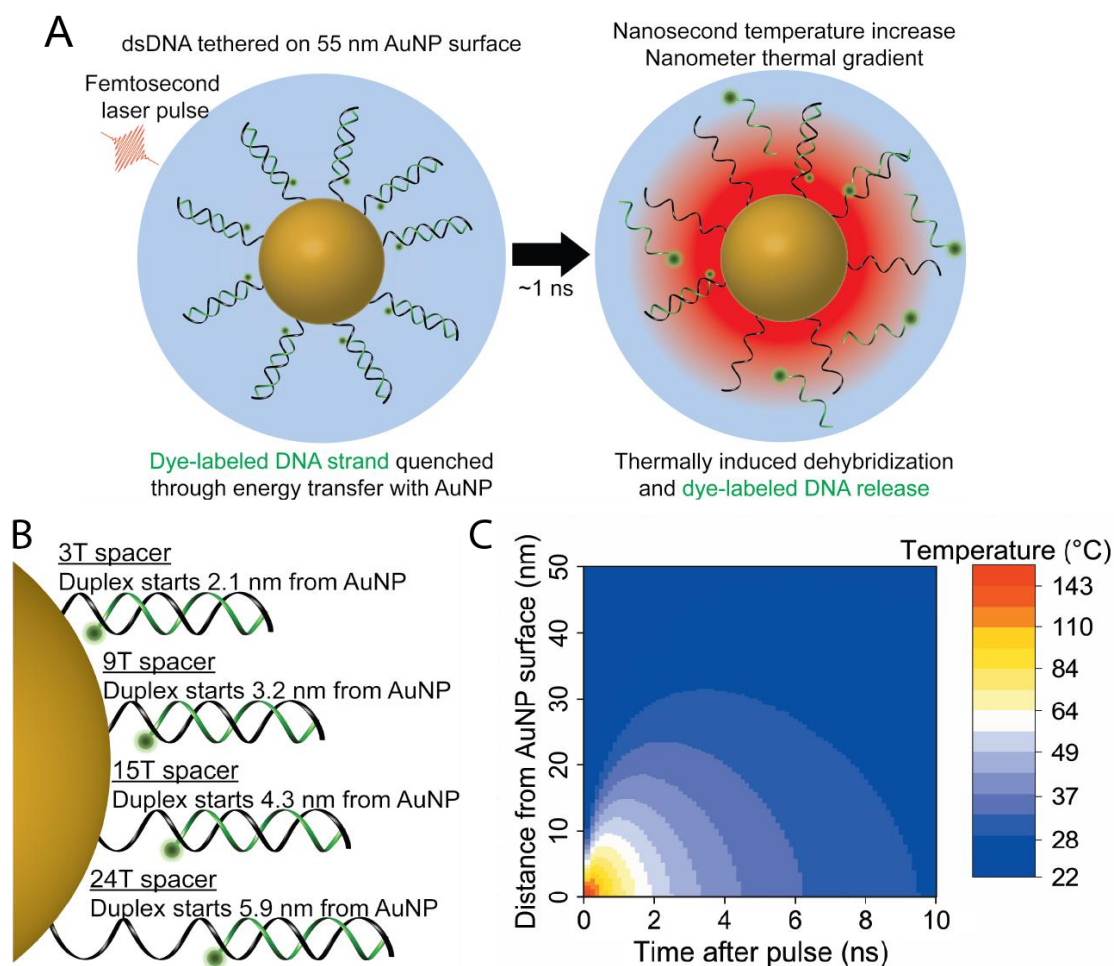


**Figure 4.1:** A) Schematic of fs-laser pulse excitation of dsDNA-AuNP (not to scale). Before heating, the dsDNA is hybridized and the OG488 fluorescence is quenched through energy transfer with the AuNP. During heating, the dsDNA denatures and the probe strands are released into solution, restoring the OG488 fluorescence and allowing for quantification of released DNA. B) Schematic of dsDNA-AuNP (not to scale) displaying the four duplexes used in this system (3T, 9T, 15T, 24T). Each duplex consists of a unique template strand (black) that contains the polyT spacer domain and enables attachment to the AuNP surface through a 5' thiol modification. The probe strand (green) is a 19 bp strand fluorescently-labeled on the 3' end with OG488 and is the same strand for each duplex. While the schematic displays all four strands on a single AuNP, only one strand is present on the AuNPs during each experiment. C) Theoretical temperature profile around a 55 nm AuNP after single pulse excitation at a pulse radiant exposure of  $14.1 \text{ J/m}^2$ .

to introduce pulsed heating into atomistic molecular dynamics (MD) simulations. This approach allowed us to build on and make comparisons to the previous examples of templated dsDNA melting simulations, which have been limited to conditions of steady-state temperatures.<sup>110-112</sup> Overall, the experimental results, numerically determined temperature profiles, and atomistic MD simulations suggest that the DNA dehybridization likely occurs through a stochastic single-pulse, dual-ended unzipping mechanism with bp separations occurring as quickly as 50 ns after heat exposure. The proximity to the gold surface and resulting exposure to high temperatures promotes surface proximal bp separation that produces an increased release rate in comparison to the theoretical prediction.

## **4.2 Results and discussion**

### *4.2.1 System design and local temperature evaluation*

To systematically increase the distance between the dsDNA and the AuNP surface, we designed four ssDNA template strands that each contain 1) a 5' thiol modification for AuNP attachment, 2) a ss, variable length, poly T spacer domain, and 3) a 19 nucleotide domain that hybridizes with a fluorescently-labeled complementary strand (probe strand) to make up the dsDNA portion of the strand (see Table 4.1). 3T, 9T, 15T, and 24T spacers are used to extend the dsDNA domain further into solution by a distance of 2.1, 3.2, 4.3 and 5.9 nm from the AuNP surface, assuming a spacing of 0.18 nm per T.<sup>113</sup> The probe strand, equivalent in all four spacer systems, was fluorescently labeled on the 3' end with OG488 in order to provide a readout of system (*i.e.*, amount of dsDNA denatured, See Chapter 3). A schematic of the designed system is shown in Figure 4.1A and 4.1B.

Strand	Sequence (5'-3')	Bases	dsDNA start (nm from AuNP)	dsDNA end (nm from AuNP)
3T-template	5ThioMC6-D/(T) <sub>3</sub> TCTCTACCTACTCACCTCA	22	2.1	8.4
9T-template	5ThioMC6-D/(T) <sub>9</sub> TCTCTACCTACTCACCTCA	28	3.2	9.5
15T-template	5ThioMC6-D/(T) <sub>15</sub> TCTCTACCTACTCACCTCA	34	4.3	10.6
24T-templaee	5ThioMC6-D/(T) <sub>24</sub> TCTCTACCTACTCACCTCA	43	5.9	12.2
OG488-probe	TGAGGTGAGTAGGTAGAGA/3AmMO-OG488	19	----	----

**Table 4.1:** DNA sequence information and dsDNA domain locations. The OG488 probe strand hybridizes to the same 19 base domain on each template strand. dsDNA domain start and end distances in relation to the AuNP surface were determined using a length of a 0.18 nm for each single stranded T linker and a length of 0.33 nm for each bp. 3AmMO; 3' amino modification, OG488; Oregon Green 488, 5ThioMC6-D; 5' thiol modification with a six- carbon linker. All DNA was purchased from Integrated DNA Technologies, Inc.

The dsDNA is hybridized before loading onto AuNPs. After loading, samples were washed three times through centrifugation to remove unbound dsDNA. The amount of DNA loaded per AuNP was quantified as discussed in Chapter 3.<sup>114</sup> dsDNA loading was found to be  $818 \pm 17$  duplexes per AuNP, regardless of the number of T spacers on the strand. To ensure that each duplex melted near the predicted  $T_m$  of 50.8 °C when displayed on the AuNP surface, we measured the bulk solution melting curves of each duplex (Figure 4.2). The melting temperatures for all duplexes on the AuNP (3T, 9T, 15T, 24T) were found to be equivalent within the experimental uncertainty,  $49.5 \pm 0.5$  °C and the melting temperature of the duplex in solution (no AuNP) was  $52.6 \pm 0.5$  °C. The 3T-solution melting curve experiment was performed using a template strand modified to contain an Iowa BlackFQ Dark Quencher at the 5' end of the strand,

similarly to the “off AuNP” melting curve experiments described in Chapter 3. In agreement with previous reports,<sup>16</sup> the melting temperature of dsDNA is slightly reduced when the duplex is tethered to AuNPs, indicating that the duplex is less stable on the AuNP surface than in solution.

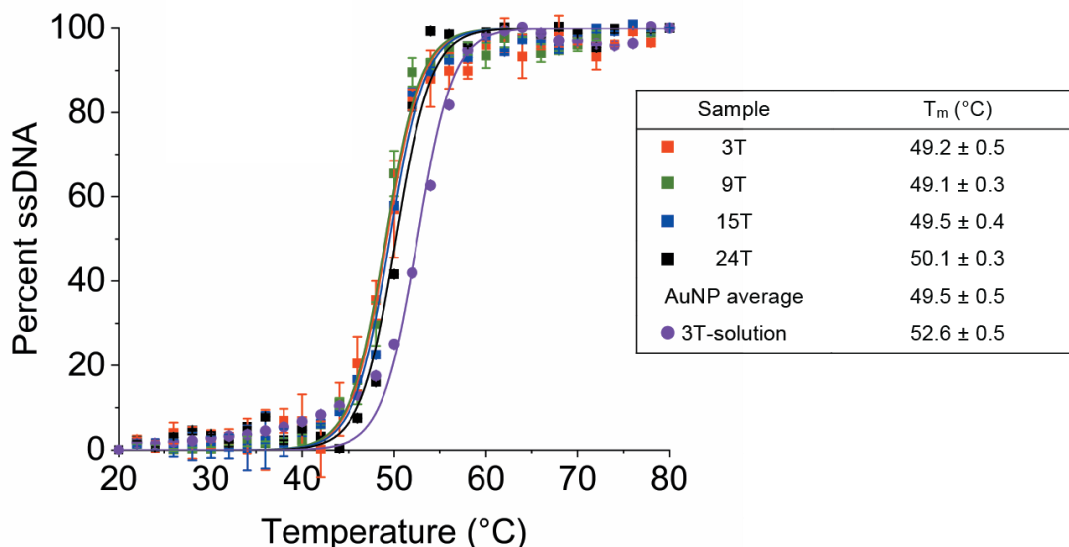


**Figure 4.2:** Bulk solution heating DNA melting curves and  $T_m$  values. 3T, 9T, 15T, and 24T are melting curves of the duplexes tethered to the AuNP surface. As in Chapter 3, the 3T-solution melting curve was obtained by using a template strand modified to contain an Iowa BlackFQ Dark Quencher at the 5' end of the strand (dye labeled DNA strand purchased from IDT). The OG488-probe strand is hybridized to the Quencher-template strand and OG488 quenching occurs through FRET ( $R_0 = 5.5$  nm).  $T_m$  values for each strand were obtained by taking the maximum of the first derivative for each melting curve. Error bars represent the std. dev. for  $n = 3$  experiments.

From the work described in Chapter 3, it was concluded that utilizing AuNPs of  $55 \pm 5$  nm diameter should provide local temperature increases of up to  $\sim 100$  °C using a 150 fs pulse width, 1 kHz repetition rate, a working excitation wavelength of 387.5 nm and pulse radiant exposures up to  $14.1 \text{ J/m}^2$ .<sup>36, 44</sup> These parameters, and our low working

concentration of 13 pM AuNP, also ensured that the AuNPs would return to baseline temperature between each pulse and that each AuNP is in a temperature-confinement regime, *i.e.*, the influence of heat from neighboring particles can be disregarded.<sup>27, 100</sup> Bulk solution measurements utilizing thermocouples demonstrated negligible temperature increases ( $< 1\text{ }^{\circ}\text{C}$ ) during laser irradiation. The theoretical temperature profile around a single 55 nm AuNP after excitation with a pulse radiant exposure of  $14.1\text{ J/m}^2$  is shown in Figure 4.1C, demonstrating the nanoscale spatial and temporal confinement of the temperature increase. All temperature profiles were numerically determined using a MATLAB code that utilizes a one-temperature thermal model previously published by the Baffou group.<sup>36, 44</sup> Following the work of Metwally *et al.* we determined the theoretical radiant exposure threshold for photothermal bubble generation with 55 nm AuNPs to be  $\sim 24\text{ J/m}^2$ ,<sup>44</sup> and as the pulse radiant exposures we use here are significantly less, it is highly unlikely water vapor bubbles are forming around the AuNPs after excitation. It has also been demonstrated by Boulais *et al.* that water bubble formation can occur from nanoscale plasma generation rather than from heating during fs-pulse irradiation at pulse radiant exposures near  $2000\text{ J/m}^2$ ,<sup>115</sup> however those pulse radiant exposures are two orders of magnitude higher than those used in this work.

We began by examining the numerically derived temperature profiles in the context of the dsDNA positional variance. Using dsDNA starting points with respect to the AuNP surface: 3T at 2.1 nm, 9T at 3.2 nm, 15T at 4.3 nm and 24T at 5.9 nm, we determined the predicted location of the dsDNA domains and the corresponding temperature profile around each dsDNA strand. The theoretical temperature profiles



indicate that the heating pulse decays to the approximate baseline temperature in ~5 ns. After the 5 ns time-window ~80% of all predicted temperature areas along the dsDNA above room temperature (RT) had passed, 100% of all predicted temperature areas above the melting temperature had passed, and all remaining temperatures were < 10 °C above RT even for the hottest system. As such, it was determined that the temperature across the length of the dsDNA domain over a 5 ns duration was a good representation of the local temperature felt by the dsDNA. In Figure 4.3A, the temperature profile for a pulse radiant exposure of 14.1 J/m<sup>2</sup> is displayed with the 5 ns average temperature of the 3T strand represented by the internal green frame. The temperature values within the green frame represent the predicted temperature profile that the dsDNA should experience from end to end over a 5 ns time interval, the average value of this temperature profile is referred to throughout the text as the ‘average temperature’. The maximum or peak temperature is the highest temperature that occurs in this time/space domain. Figure 4.3A represents the hottest temperature profile around the 19 bp duplex in our system. For comparison, the theoretical temperature profile for a pulse radiant exposure of 7.1 J/m<sup>2</sup> is displayed with the footprint of the 24T strand in Figure 4.3B (the coolest temperature profile in our system). The theoretical max and average temperatures for the pulse radiant exposures used in this work (14.1, 10.5 and 7.1 J/m<sup>2</sup>) are reported in Figure 4.3C. As predicted, the max and average temperature decreases for lower pulse radiant exposures and for dsDNA strands that are extended further from the NP surface. As the strand is moved farther from the AuNP surface by the ~1.1 nm spacing interval, the average temperature decreases by  $1.7 \pm 0.3$  °C,  $1.3 \pm 0.2$  °C, and  $0.9 \pm 0.1$  °C for pulse radiant exposures of

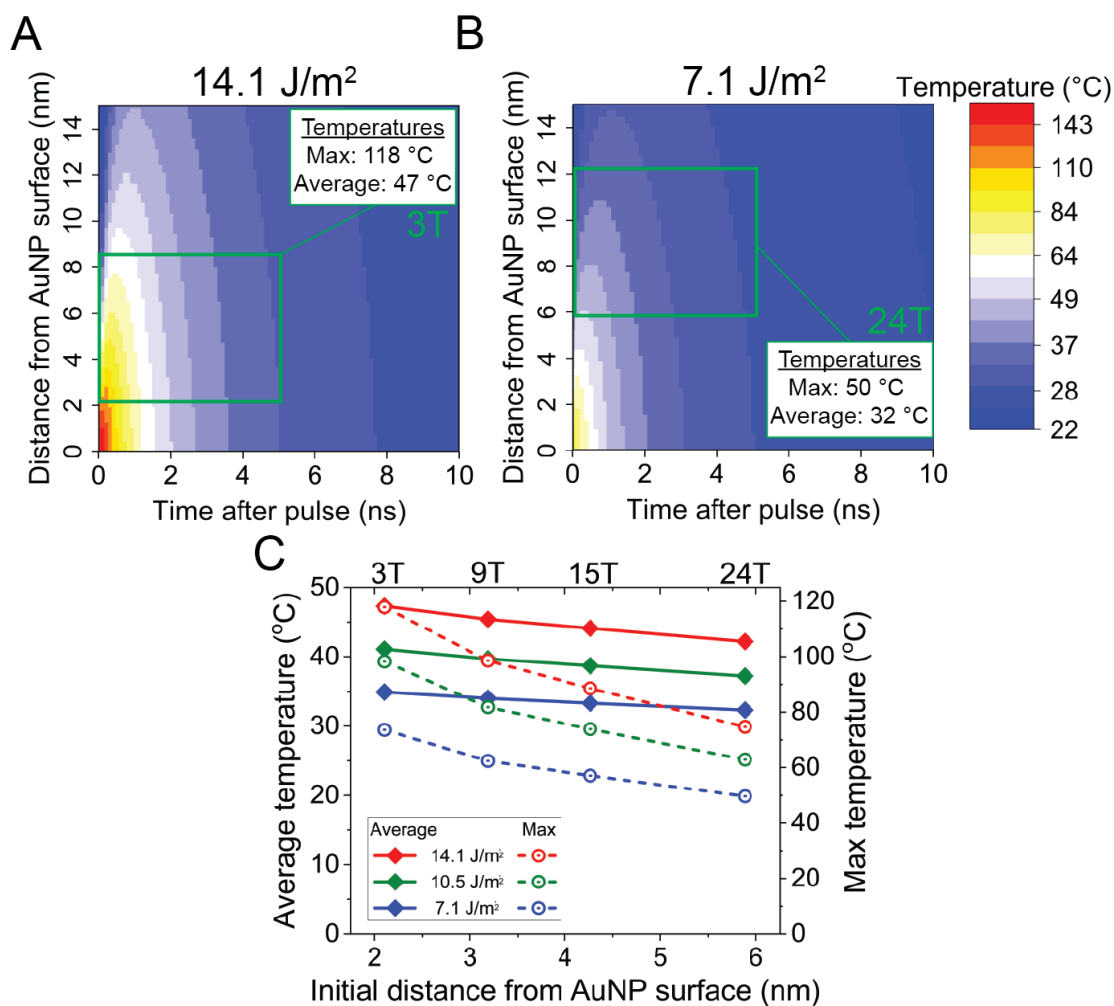


**Figure 4.3:** Representative temperature profiles and 5 ns average temperature determinations. A) Temperature profile around a 55 nm AuNP after single pulse with pulse radiant exposure 14.1 J/m<sup>2</sup>. Temperature scale same as in B. The internal green frame represents the temperatures used to determine the 5 ns average temperature across the length of the dsDNA, in this case the area for the 3T strand is displayed, the hottest temperature profile around the 19 bp duplex used in this work (average temperature = 47.3 °C, maximum temperature = 117.9). B) Similar to A), the temperature profile for a pulse radiant exposure of 7.1 J/m<sup>2</sup> with the internal green frame representing the temperatures used for the 24T strand, the coolest temperature profile around the 19bp duplex (average temperature = 32.3 °C, maximum temperature = 49.7 °C) C) Double Y-axis showing the 5 ns average temperatures (full lines) and the maximum temperature (dashed lines) across each strand for pulse radiant exposures of 14.1, 10.5, 7.1 J/m<sup>2</sup>.

14.1, 10.5 and 7.1 J/m<sup>2</sup> respectively (see full lines in Figure 4.3C). The uncertainties are the standard deviations of the average temperature change across the three dsDNA distance shifts (from 3T to 9T, 9T to 15T, 15T to 24T). In comparison, as the strand is moved ~1.1 nm into solution, the maximum temperature achieved in the system decreases by  $14.4 \pm 3.8$  °C,  $11.8 \pm 3.6$  °C, and by  $8.0 \pm 2.4$  °C for pulse radiant exposures of 14.1, 10.5 and 7.1 J/m<sup>2</sup> respectively (see dashed lines in Figure 4.3C). Clearly, the maximum temperature difference (68 °C) is considerably larger than the average temperature difference (15 °C), highlighting the complex nature of these heating profiles. By monitoring the denaturation of the dsDNA at different distances from the AuNP surface, we expect to elucidate the influence that the maximum and average temperatures have on the denaturation process.

#### *4.2.2 dsDNA denaturation during fs-laser pulse heating of AuNPs*

Each test dsDNA-AuNP system under evaluation was irradiated at pulse radiant exposures of 14.1, 10.5 and 7.1 J/m<sup>2</sup> for up to  $(100 \times 10^3) \pm 1000$  pulses using a 1 kHz laser. This is equivalent to a maximum of 100 seconds of irradiation, though the actual or active irradiation time is in fact only 15 ns and the total heating time is ~500 μs (estimated from the numerically determined temperature profiles). The AuNP concentration was fixed at 13 pM and the solution volume was restricted to 200 uL so that the laser spot was interacting with the entire sample during irradiation. Samples were placed in the laser path for a given number of pulses then centrifuged to pellet the AuNP and collect the probe DNA released in the supernatant. A standard curve was then used to convert OG488 fluorescence into number of DNA released (data not shown, see Chapter 3 for representative example). We note that due to steric issues and

base absorption by the template strand to the AuNP surface post denaturation, for all intents and purposes the DNA dehybridization is irreversible once the probe strand is released into solution.<sup>114, 116</sup> AuNP integrity and colloidal stability were verified after 100 seconds of irradiation at 14.1 J/m<sup>2</sup> through absorbance measurements (data not shown, see Chapter 3 for representative example). In the absence of irradiation, no DNA release was detectable.

Once the DNA release data was collected, the release profiles were fit to a previously derived pulsed-release equation (Eq. 3.8, Chapter 3) to determine the temperature “sensed” by the dsDNA.<sup>114</sup> The fitting parameters are reported in the Materials and methods section. Figure 4.4A displays the release profile and corresponding fits for 15T at pulse radiant exposures of 14.1, 10.5 and 7.1 J/m<sup>2</sup> respectively. As previously reported, the dsDNA release rate decreases with a drop in pulse radiant exposure, as lower pulse radiant exposures generate temperature profiles with smaller temperature magnitudes (Figure 4.3C).<sup>114</sup> We also observe this trend in the sensed temperature values (Table 4.2) obtained from the fits of the release data. This is also observed for 3T, 9T, and 24T (release data not shown, see Table 4.2 for sensed temperatures). In Figure 4.4B, the release profile for each strand at a pulse radiant exposure of 10.5 J/m<sup>2</sup> is displayed. Consistent with the predictions, the closer the dsDNA domain is to the AuNP surface the quicker the probe DNA is released into solution, as the max and average temperature are higher when in close proximity to the AuNP surface (Figure 4.3C), promoting quicker release. The sensed temperature values emphasize this observation and are reported in Table 4.2. We also observed this trend for pulse radiant exposures of 7.1 and 14.1 J/m<sup>2</sup> (release data not shown, see Table 4.2

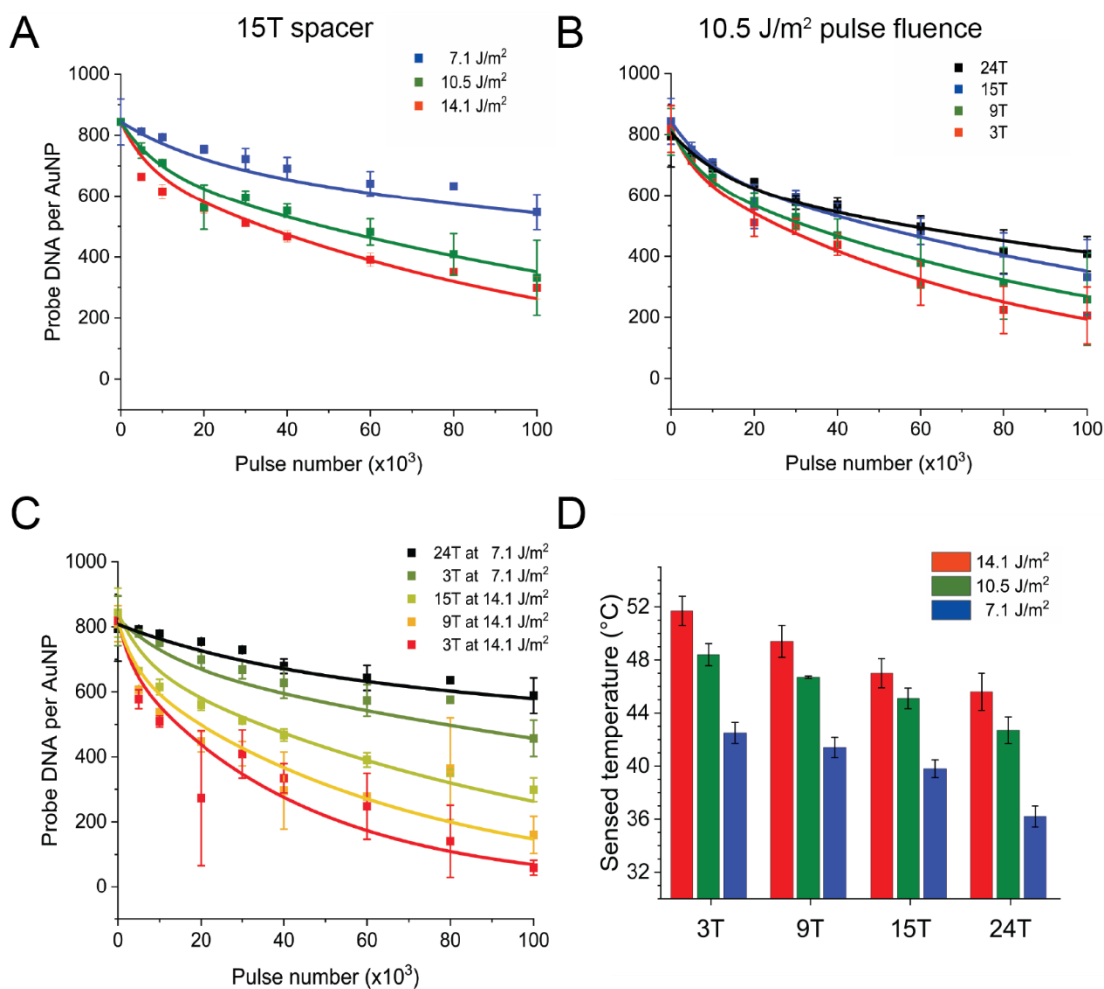


**Figure 4.4:** A) DNA release profile and fits to pulsed released equation (Eq. 3.8) for 15T at pulse radiant exposures of 7.1, 10.5 and 14.1 J/m<sup>2</sup>. B) DNA release profile and fits (Eq. 3.8) for 3T, 9T 15T and 24T at a pulse radiant exposure for 10.5 J/m<sup>2</sup>. C) Release profiles and fits (Eq. 3.8) for various linker length and pulse radiant exposure combinations, demonstrating the high level of temporal control afforded over dsDNA denaturation with fs-laser pulse AuNP heating. D) Sensed temperatures obtained by fitting release data with Eq. 3.8. Standard deviations are derived from triplicate measurements.

for sensed temperatures). For the two extremes in our system (3T at 14.1 J/m<sup>2</sup> and 24T at 7.1 J/m<sup>2</sup>) we report a sensed temperature difference of  $16 \pm 2.2$  °C, in excellent agreement with the theoretical average temperature difference of  $\sim 15$  °C. Additionally we report that the sensed temperature decreased by an average of  $2.0 \pm 0.7$  °C across

		3T	9T	15T	24T
14.1 J/m <sup>2</sup>	Maximum temperature (°C)	117.9	98.6	88.6	74.7
	Average temperature (°C)	47.3	45.4	44.1	42.2
	Sensed temperature (°C)	51.7 ± 0.8	49.4 ± 0.8	47.0 ± 0.7	45.6 ± 0.8
	ΔT temperature (°C)	4.4 ± 0.8	4.0 ± 0.8	2.9 ± 0.7	3.4 ± 0.8
10.5 J/m <sup>2</sup>	Maximum temperature (°C)	98.3	81.8	73.9	62.9
	Average temperature (°C)	41.1	39.7	38.7	37.2
	Sensed temperature (°C)	48.4 ± 0.8	46.7 ± 0.9	45.1 ± 0.8	42.7 ± 0.8
	ΔT temperature (°C)	7.3 ± 0.8	7.0 ± 0.9	6.4 ± 0.8	5.5 ± 1.0
7.1 J/m <sup>2</sup>	Maximum temperature (°C)	73.6	62.4	57.1	49.7
	Average temperature (°C)	34.9	34.0	33.3	32.3
	Sensed temperature (°C)	42.5 ± 1.1	41.4 ± 1.2	39.8 ± 1.1	36.2 ± 1.4
	ΔT temperature (°C)	7.6 ± 1.1	7.4 ± 1.2	6.5 ± 1.1	3.9 ± 1.4

**Table 4.2:** Quantification of local temperature around dsDNA after femtosecond-laser pulse excitation<sup>a</sup>.

<sup>a</sup>Temperature values used in analysis of dsDNA denaturation during fs-pulse laser heating of AuNPs for the various linker lengths (3T, 9T, 15T, 24T) and pulse radiant exposures (14.1, 10.5 and 7.1 J/m<sup>2</sup>) used in this work. Maximum temperature is the highest temperature value in the numerically simulated temperature profile. The average temperature is the temperature average across the length of the dsDNA for a 5 ns time interval after the heating begins (see Figure 4.3A,B). The sensed temperature is obtained from fitting the DNA release to Eq. 3.8. The ΔT temperature is the difference between the sensed temperature and average temperature. All error bars are derived from triplicate measurements.

all pulse radiant exposures as the strand is moved ~1.1 nm into solution, whereas the theoretical average temperature decrease was  $1.3 \pm 0.4$  °C. A more expansive analysis of this general agreement is discussed later in the text. In Figure 4.4C, we demonstrate the high level of control afforded over DNA release using fs-laser pulse AuNP heating. By precisely positioning the dsDNA with respect to the AuNP surface and modulating the pulse radiant exposure, the amount of DNA released can be varied over 26-93% in only 100 seconds of irradiation. Using the 3T strand at a pulse radiant exposure of 14.1 J/m<sup>2</sup>, 93% of the DNA is released into solution and by simply fixing the dsDNA 3.8

nm further from the surface (using the 24T strand) we decreased the DNA release to ~63%. The DNA release can be reduced even further to 26% by reducing the pulse radiant exposure to 7.1 J/m<sup>2</sup>.

Based on these results, we examine the important variables for DNA denaturation in nanoscale thermal gradients. Although there is sensible agreement for the temperature differences between the various spacer strands and pulse radiant exposures, the sensed temperatures are consistently higher than the average temperatures. Though the choice of time-window for the average temperature would modify the precise values, for any substantial time-length (*i.e.*, 3-10 ns), the trends are consistent. As such we utilize the 5 ns time-window as discussed in the previous section. The differences between the sensed and average temperatures, reported in Table 4.2 and Figure 4.5A, are more pronounced when the dsDNA is closer to the AuNP surface and at the lower pulse radiant exposures of 10.5 and 7.1 J/m<sup>2</sup>. When the dsDNA is closer to the AuNP surface, differences between the max and average temperatures significantly increase. For example, a max-average temperature difference of 70.6 °C for 3T and of 32.5 °C for 24T are predicted for a pulse radiant exposure of 14.1 J/m<sup>2</sup>. This difference is not surprising since the temperature profile follows a  $\sim r^{-3}$  decay from the AuNP surface. In Figure 4.5B, the relative standard deviation of the temperature profile ( $\sigma/\text{average temperature}$ ) around the dsDNA is shown for the different linker lengths (3T, 9T, 15T, 24T). For each linker length, the relative standard deviation is an average across the three pulse radiant exposures. A lower relative standard deviation represents a more uniform temperature profile (*i.e.*, a smaller difference between maximum and average temperature). The relative standard

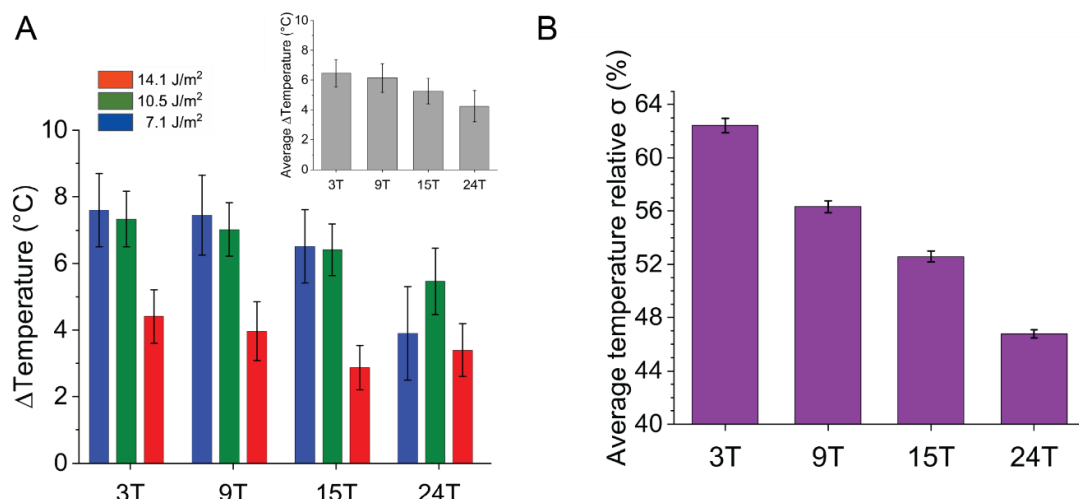


**Figure 4.5:** A)  $\Delta T$  temperature, obtained by subtracting the theoretical average temperature from the sensed temperature, as a function of pulse radiant exposure and dsDNA linker length. Inset: Representation of the average  $\Delta T$  temperature across the three pulse radiant exposures (14.1, 10.5, 7.1 J/m<sup>2</sup>) for each linker length. B) Relative standard deviation of the first 5 ns of the theoretical temperature profiles in which the dsDNA are located after fs-laser pulse excitation of the dsDNA-AuNP systems. For each linker length, the relative standard deviation is an average across the three pulse radiant exposures.

deviation of the temperature at different pulse radiant exposures does not vary much, as shown by the small error bars, but for the different distances from the AuNP surface the trend is clear. As the dsDNA is extended further from the AuNP surface, the decrease in the relative standard deviation of the temperature profile correlates well with the better agreement between the sensed temperature and average temperature empirically observed in our system (Figure 4.5A inset).

At a pulse radiant exposure of 14.1 J/m<sup>2</sup>, better agreement between the sensed and average temperature is observed. Across all the dsDNA strands, the average temperature is  $44.8 \pm 1.9$  °C,  $39.2 \pm 1.4$  °C, and  $33.6 \pm 1.0$  °C for the pulse radiant



exposures of 14.1, 10.5, and 7.1 J/m<sup>2</sup>, respectively. Interestingly, all of the average temperatures are below the melting temperature of 49.5 °C for this duplex, yet a temperature of  $44.8 \pm 1.9$  °C (14.1 J/m<sup>2</sup> average temperature) is high enough to cause  $14.8 \pm 5.2\%$  of the duplexes to melt in bulk/equilibrium heating (Figure 4.2). This is experimentally observed in the good agreement between the sensed and average temperature at 14.1 J/m<sup>2</sup>. In contrast, the average temperatures generated from pulse radiant exposures of 10.5 and 7.1 J/m<sup>2</sup> would only result in  $4.7 \pm 2.2\%$  and  $2.7 \pm 1.5\%$  of the duplexes melting in bulk/equilibrium heating (Figure 4.2). The above observations may indicate that the dsDNA denaturation occurring at the lower pulse radiant exposures is primarily driven by the peak or maximum temperatures, causing the dsDNA to release faster than predicted by the average temperature and for the  $\Delta T$  temperature to increase.

Perhaps the simplest comparison is to contrast the (24T-14.1 J/m<sup>2</sup>) result to (15T-10.5 J/m<sup>2</sup>) and (3T-7.1 J/m<sup>2</sup>). All three have a maximum temperatures of ~75 °C, but the average temperature are 42, 39, and 35 °C, respectively. The (24T-14.1 J/m<sup>2</sup>) is furthest from the surface and has the highest average temperature, resulting in the smallest  $\Delta T$  (3.4 °C). The (3T-7.1 J/m<sup>2</sup>) is closest to the surface with a low average temperature, resulting in the highest  $\Delta T$  (7.6 °C). While the (15T-10.5 J/m<sup>2</sup>) is between those two states and as expected has an intermediate  $\Delta T$  (6.4 °C).

#### *4.2.3 Molecular dynamics simulations of dsDNA denaturation*

In order to better understand the mechanism of dsDNA melting in the nanosecond duration heating profiles, we collaborated with Dr. Parth Chaturvedi and Prof. Lela

Vuković from the University of Texas El Paso to preform MD simulations that mimic the heat pulse around the dsDNA after AuNP excitation. In simulations, the modeled systems were based on the shortest spacer strand (3T) and our highest pulse radiant exposure ( $14.1 \text{ J/m}^2$ ), where approximately 93% of the dsDNA is released after the AuNP is excited by  $10^5$  fs-laser pulses. With only ~818 dsDNA strands per AuNP, it is evident that a particular pulse has a very small probability of denaturing a DNA duplex (on average 0.008 strands released per pulse, based off the release rate of 3T at  $14.1 \text{ J/m}^2$  pulse radiant exposure). Because denaturing is such a rare event when examined on a pulse-by-pulse basis, we utilize a smaller 13 bp duplex for our MD simulations. The theoretical melting temperature of the smaller 13 bp duplex is  $35.1^\circ\text{C}$ , approximately  $15^\circ\text{C}$  lower than that of the 19 bp duplex used in the experimental work. We have previously shown that for fs-laser pulse heating of dsDNA-AuNPs, dsDNAs with lower melting temperatures have a higher probability of denaturing at a given pulse radiant exposure.<sup>114</sup> Simulations of the 13 bp duplex provide dynamics of DNA melting under fs-laser pulse heating without the need for excessive computational reiterations, saving time and costs.

The effects of the non-uniform heat pulses on dsDNA at the AuNP surface were examined in atomistic MD simulations of dsDNA covalently bound to a flat segment of a gold crystal. The simulated system contained a 13-bp long dsDNA attached to a 3T spacer ssDNA and an alkane thiol linker (same linker as the experimental system), covalently bound to the gold surface *via* the Au-S bond. First, the system was equilibrated at a constant temperature of  $22^\circ\text{C}$ . Then it was simulated in non-equilibrium conditions to mimic the AuNP heating and cooling processes induced by a

single laser pulse at  $14.1 \text{ J/m}^2$ , or in equilibrium conditions at a constant temperature of  $49^\circ\text{C}$  (this is the average temperature across the 3T-13 bp duplex for a  $14.1 \text{ J/m}^2$  pulse radiant exposure). The MD heating profile was tuned to match the theoretical temperature profile of the aqueous solution after AuNP excitation obtained from the previously published MATLAB code.<sup>44</sup>

The initial conformation of the 13-bp dsDNA duplex, solvated in the aqueous solution and oriented normal to the gold surface, is shown in Figure 4.6A. During 100 ns of equilibration at  $22^\circ\text{C}$ , the number of dsDNA-gold interactions increased, with the dsDNA duplex eventually tilting towards the gold surface, and the hydrogen bonding between the first and last bps breaking and quickly forming again. Once formed, the interactions between dsDNA and the gold surface remain stable over the course of the trajectory, which is similar to previous MD studies<sup>117</sup> as well as to observations made for other polymers adsorbing to solid surfaces.<sup>118-120</sup> Overall, the simulations demonstrate that the presence of the gold surface has a significant effect on duplex conformations, as also confirmed by a comparison of simulations using a 19-bp dsDNA duplex on the gold surface and in aqueous solution (data not shown) and previous studies.<sup>121-122</sup>

In the next step, the 13-bp dsDNA system (Figure 4.6A), pre-equilibrated for 100 ns at  $22^\circ\text{C}$ , was simulated in three independent runs where the temperature profile was tuned to mimic the localized heating induced in the AuNP by a single fs-laser pulse at  $14.1 \text{ J/m}^2$ . The temperature profile obtained in the aqueous solution during the simulation is shown in Figure 4.6B. After the initial heat pulse, the system was run for an additional 100 ns. A representative 13-bp dsDNA conformation on the gold surface

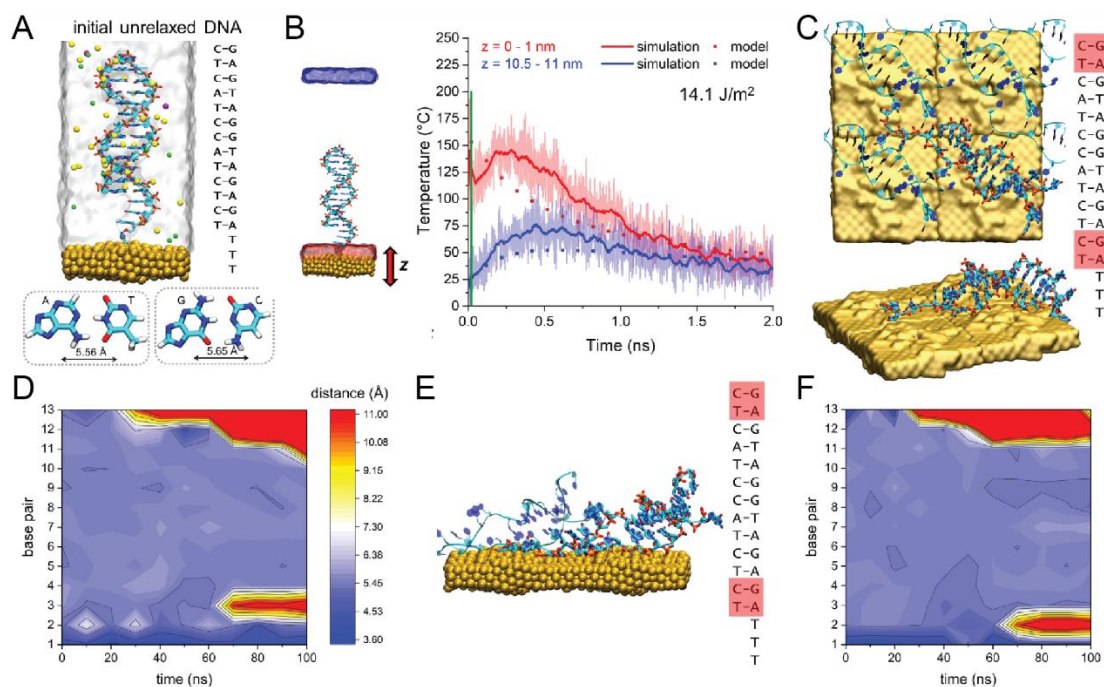


**Figure 4.6:** Molecular dynamics simulations of dsDNA attached to the gold surface and exposed to pulse heating and continuous heating. A) The initial system and definition of bp distances. Water is shown as a transparent surface, and system atoms are shown in cyan (C), red (O), blue (N), orange (P), white (H), gold (Au), yellow ( $\text{Na}^+$ ), green ( $\text{Cl}^-$ ) and magenta ( $\text{Mg}^{2+}$ ). B) Temperature profiles at two distances from the AuNP surface (0-1 nm in red and 10.5-11 nm in blue). The model temperature was obtained from the MATLAB code and the simulated temperature was used during MD. C) Representative dsDNA conformation on the gold surface 100 ns after the application of the heat pulse, bps highlighted in red are broken. D) Heat map of the bp distances in dsDNA during the first 100 ns after the application of the heat pulse shown in panel B. E) Representative dsDNA conformation on gold surface after 100 ns equilibration at 49 °C constant temperature, bps highlighted in red are broken. F) Heat map of the bp distances in dsDNA during 100 ns equilibration at 49 °C constant temperature. The color scheme in the map is the same as in panel D.

100 ns after the application of the heat pulse is shown in Figure 4.6C. The breaking of hydrogen bonds is observed at both ends of the duplexes in all simulations, as shown in a representative heat map in Figure 4.6D. After the heat pulse, the bps began to break

on both ends of the duplex and the breaking progressed towards the duplex center from both ends. The number of broken hydrogen bonds varies between 1 and 5 base paired nucleotides at the duplex end closer to the Au-S bond, and between 1 and 3 base-paired nucleotides at the other end of the duplex. On average, 100 ns after a heat pulse, the end of the duplex closest to the Au surface had  $3.3 \pm 1.2$  bps broken, the opposite end of the duplex had  $2.0 \pm 1.0$  bps broken and the whole duplex had a total of  $5.3 \pm 0.9$  bps broken (40%). It is generally considered that  $\geq 50$  % bp separation results in full DNA dehybridization,<sup>112</sup> so though we do not reach the exact threshold, there is considerable convergence. A significant portion of the bp breaking begins to occur after tens of nanoseconds into the simulation and progress over time. Previously published MD simulations have investigated the melting of a 12bp poly A-T duplex in solution and on a silica surface at 400 K.<sup>111-112</sup> These earlier works reported that melting occurred within a few nanoseconds of the temperature jump. It is not surprising that melting was observed to occur quicker in these reports as the 12 bp poly A-T duplex is significantly less stable ( $T_m < 20$  °C) than the 13 bp duplex we utilized, the 400 K temperature is significantly higher than our MD simulation temperatures, and no  $Mg^{2+}$  ions were utilized in the previous reports.

For comparison, we separately ran simulations of the 13 bp duplex on the Au surface in a uniform and continuous heating profile (steady state temperature of 49 °C). Figure 4.6E shows a representative conformation of DNA after 100 ns equilibration in constant 49 °C temperature conditions as this is the 5 ns time-window average temperature across the length of the dsDNA during the pulsed heating simulation. After 100 ns of heating, the end of the duplex closest to the Au surface had  $2.3 \pm 0.5$  bps

broken, on the opposite end of the duplex  $2.0 \pm 0.0$  bps had broken and the whole duplex had a total of  $5.7 \pm 2.4$  bps broken. Here, we also observe that a majority of the bp breaking occurred tens of nanoseconds into the simulation and progressed over time. In all three independent runs performed at constant 49 °C temperature, dsDNA conformations behaved in a similar way as after the laser pulse heating simulations. Even though molecular dynamics are stochastic, the heat maps of bp nucleotide distances over time during steady state heating have significant similarity to the heat maps determined for the pulsed heating system. The observation that dsDNA behavior and resulting structures at 49 °C are similar to dsDNA behavior and structures when exposed to fs-laser pulse heating ( $14 \text{ J/m}^2$ ) provides validation to the performed modeling and analysis. In both the equilibrium and pulsed heating simulations, we observe bps breaking on the end of the duplex away from the Au surface. This “unzipping” from the non-tethered end of the duplex has been previously reported for melting of dsDNA on a silicon dioxide surface.<sup>111</sup> In the fs-laser pulse heating simulation, there is ~1 more broken bp on the dsDNA end near the gold surface as compared to the 49 °C equilibrium simulation. The difference indicates that although the temperature increase lasts ~20 times longer during the 49 °C simulation, that high local temperatures near the AuNP surface in the heating pulse simulation are present long enough to cause more bp breaking in this region of the dsDNA. This is not surprising as the high temperatures near the AuNP surface exceed 110 °C and likely cause significant bp disruption in the close portion of the dsDNA. Further comparisons performed using atomistic MD simulations suggests that the gold surface is a factor in increasing dsDNA dehybridization rates. Simulations were run that compared similar

temperature conditions with and without the gold surface (data not shown) and it was seen that the gold-bound dsDNA had more bp separations than the freely diffusing dsDNA. This observation aligns well with literature evidence that show that AuNP bound dsDNA has conformations that have lower melting temperatures,<sup>16</sup> as well as our own experimental work where we observed a decreased melting temperature in bulk heating experiments when the dsDNA was bound to the AuNP and a two conformation release profile during fs-laser pulse heating.

#### *4.2.4 Discussion*

Connecting the MD and experimental results, we postulate the following mechanisms and variables that are key to DNA dehybridization as displayed on fs-laser pulsed AuNPs. The AuNP surface plays an important part in lowering the activation energy required for dehybridization as seen through greater bp separation of dsDNA termini in MD simulations and decreased bulk melting temperatures when the dsDNA was bound to the AuNP. This surface effect is of greater relevance to bps that are nearer to the AuNP surface. This suggests that AuNPs coated with other materials, *e.g.*, SiO<sub>2</sub> or Ag, may have different release profiles under the same heating conditions. Of greater import is the conclusion that dsDNA dehybridization occurs through a single-pulse, dual-ended unzipping mechanism with bp separations occurring as quickly as tens of nanoseconds after heat exposure for both steady-state and pulsed heating profiles. The significant difference in the fs-laser pulse induced heating gradients is that the extremely high-temperatures near the AuNP surface, even if they last for  $\leq 3$  ns, results in increased base-pair separation of the DNA nearest to the AuNP surface. This was

supported by the fact that the sensed temperatures are consistently higher than the average temperatures (see Figure 4.5A).

A simplified, yet useful, way of thinking about this proposition is that the sensed temperature is composed of the DNA release caused by exposure to: A) ~1 ns-duration max temperatures ( $>100\text{ }^{\circ}\text{C}$  near AuNP surface) and B) ~5 ns duration average temperature over the dsDNA extension. The question that now arises is that of what is the relative weight of these two components? Two variables provide insight when understanding the relative weight of the max and average temperatures. The first is the positional exposure to the heat gradients as seen by comparing the 3T, 9T, 15T, and 24T systems. Considering the sharp,  $r^{-3}$ , dependence of the temperature profile, it is expected that the further the dsDNA from the AuNP, the smaller the relative standard deviation of the temperature will be (Figure 4.5B). Though the uncertainty of the values is appreciable (only 3T and 24T have a  $P < 0.15$  based on a two sample t-test), the trend seen in Figure 4.5A inset is clear, a decrease of the  $\Delta T$  is observed with increasing distance from the AuNP surface. This observation and that the difference between max and average temperatures increases as the dsDNA approaches the AuNP surface signifies that the relative importance and influence of the max temperature as a dsDNA denaturation activator increases the closer you get to the AuNP surface.

The second issue is the relationship between the average temperature and the dsDNA melting temperature. This effect is seen clearest when comparing the temperature profiles of the 7.1 and 14.1 J/m<sup>2</sup> pulse radiant exposures (Figure 4.3, Table 4.2). The higher pulse radiant exposure has an average temperature profile between 42-47  $^{\circ}\text{C}$  for all the dsDNA strands while for 7.1 J/m<sup>2</sup> the average temperature profile is



between 32-35 °C. If we compare these values to the bulk melting temperature of 49.7 °C, we would expect  $14.8 \pm 5.2\%$  and  $2.7 \pm 1.5\%$  ssDNA in a steady-state dehybridization curve. Clearly, the average temperature for 7.1 J/m<sup>2</sup> is not high enough to cause significant duplex denaturation in bulk heating. We can again compare the  $\Delta T$  shown in Figure 4.5A and see that the relative difference for the 7.1 J/m<sup>2</sup> system is consistently higher than for 14.1 J/m<sup>2</sup>. This indicates that for 7.1 J/m<sup>2</sup> the peak temperatures and AuNP proximal base pair separation drives the dsDNA denaturation dynamics as the average temperature is not high enough to cause significant perturbations throughout the entire dsDNA. In the case of 14.1 J/m<sup>2</sup>, the average temperature is high enough to cause significant melting of the dsDNA in bulk heating and the weight of max-temperature is relatively diminished. This can be compared to our MD simulations, where we observed good agreement between the base pair breaking in the steady-state and pulse heating simulations, as 49 °C is high enough temperature to cause significant denaturation of the 3T-13 bp strand in bulk heating, diminishing the weight of the max temperature peaks.

### ***4.3 Conclusions***

Through a combination of experiment and MD simulations, this study provides a basis for understanding the dehybridization mechanisms of dsDNA displayed on AuNPs during fs-laser pulse heating. The temperature increase around the AuNP after fs-laser pulse excitation, has a  $\sim r^{-3}$  temperature dependence and nanosecond temperature duration, creating a highly dynamic local environment in which the dsDNA is positioned. We found that a shift as small as  $\sim 1$  nm from the AuNP surface changed the dsDNA dehybridization rate up to 30% by placing the dsDNA in a lower

magnitude temperature profile. By varying both the laser pulse radiant exposure and distance between dsDNA and the AuNP surface, we demonstrated that the amount of DNA released can be varied in a range of 26-93% release in only 100 seconds of laser exposure. This data can be modeled to provide an experimentally determined sensed temperature, making the whole construct a nanothermometer capable of reporting on temperatures within the 15 nm extending from the AuNP surface. The increased dehybridization rate of dsDNA observed when closer to the AuNP can be explained by the relatively high maximum or peak temperatures in this environment (*i.e.*, a more intense temperature gradient). As the dsDNA is extended into solution the relatively high maximum temperatures are avoided, causing the dsDNA to denature at a rate better predicted by the average temperature. Interestingly, we find that the influence of the maximum temperature on dsDNA denaturation depends on the magnitude of the average temperature increase (*i.e.* if the average temperature approaches the dsDNA melting temperature) and observe that when the average temperature is not high enough to cause significant dsDNA melting in bulk heating, the maximum temperatures proximal to the AuNP surface drive the dsDNA denaturation dynamics. These interpretations are further supported by MD simulations where we find that DNA dehybridization on the surface of AuNPs likely occurs through a stochastic single-pulse, dual-ended unzipping mechanism. We observed bp separations occurring as quickly as tens of nanoseconds after heating, and due to the proximity to the gold surface and exposure to ultra high temperatures there, the bps proximal to the AuNP surface have a higher probability of separating compared to steady state heating simulations.

Overall, we have demonstrated that when using fs-laser pulse optical heating of AuNPs for dsDNA denaturation, the distance from the AuNP surface at which the dsDNA resides can be strategically selected to control the temperature profile and consequently the denaturation rate at a given pulse radiant exposure. By understanding the mechanism of DNA denaturation in a highly local temperature increase, confined photothermal heating systems can be better designed for temporal control over DNA release without causing off target heating effects. Our work should be directly translatable to delivery of other nucleotide systems such as RNA and peptide nucleic acids). Additionally, understanding the key variables of DNA denaturation in nanoscale temperature gradients should provide insight towards controlling other biological materials through confined photothermal heating in a similar NP-material-laser heating scenario.

#### ***4.4 Materials and methods***

##### *4.4.1 AuNP synthesis*

The synthesis of 55 nm AuNPs was previously described in multiple reports.<sup>15, 114, 123</sup> Briefly, the synthesis was carried out in an aqueous phase using a seeding growth method in the presence of citric acid and ascorbic acid. 10 nm AuNP seeds were first synthesized with sodium citrate and NaBH<sub>4</sub>. Seeds were then added to 0.4 mM HAuCl<sub>4</sub> and 0.8 mM sodium citrate in 50 mL of deionized water. Next, L-ascorbic acid was added to the solution at 2 mM. The solution was then stirred for 2 h at room temperature. The solution was then kept at room temperature for 24 h. UV-Vis absorption spectroscopy was then used to measure the AuNP surface plasmon

resonance band's red shift from 515 to 531 nm as well as the decrease of the ascorbic acid peak. Transmission electron microscopy was then used to confirm the size of the AuNP ( $55 \pm 5$  nm).<sup>123</sup>

#### *4.4.2 dsDNA attachment to AuNP and quantification procedures*

All DNA was purchased from Integrated DNA Technologies, Inc. The probe DNA strand has a 3' amino modification and was conjugated with Oregon Green 488 Carboxylic Acid, Succinimidyl Ester, 5-isomer (ThermoFisher Scientific) using the labeling protocol described in Chapter 3. Probe strands were then purified using PD-10 Columns (GE Healthcare). For probe strand hybridization to the template spacer strands, the strands at 0.05 mM were combined into a solution of 100 mM HEPES pH 7.5 with 5 mM MgCl<sub>2</sub>. The solution was then heated to 85 °C and then cooled by 1 °C per minute to thermally anneal the DNA strands in a PCR thermal cycler. The newly formed dsDNA was then stored at 4 °C or immediately used. To conjugate the dsDNA to the AuNP surface, the dsDNA was first incubated with Tris(carboxyethyl) phosphine hydrochloride (TCEP) at a molar ratio of 1:100 for 30 min to reduce the thiol bond on the 5' end of the template strand. Then the 55 nm AuNPs were added to the dsDNA at a ratio of 1:2000 in 50 mM HEPES pH 7.5 with 5 mM MgCl<sub>2</sub>. This solution was stirred overnight at room temperature and then concentrated and rinsed to remove unbound dsDNA using Amicon ultracentrifugation column (molecular weight cutoff of 100 kDA). To calculate the loading of DNA onto the AuNP, the dsDNA-AuNP samples were heated to 80 °C for 2 h in order to dehybridize all of the DNA on the AuNP surface. The solution was then centrifuged at 5000 x g for 5 min and the supernatant was collected. The supernatant was quantified to determine the amount of DNA

released. A standardization curve was used to convert the fluorescence of the released probe strand into the amount of DNA (Figure 4.1A).

#### *4.4.3 Bulk heating of dsDNA-AuNPs*

dsDNA-AuNP conjugates were placed in a temperature-controlled fluorometer cuvette and the bulk solution temperature was raised from 20 to 80 °C at 1 °C per minute. Every 2 °C a fluorescent measurement was taken. For the 3T strand in solution, we used a modified template strand containing a 5' Iowa BlackFQ Dark Quencher. To measure the melting curves, a 1:1 solution at 5 nM of the modified template strand and the probe strand were annealed to form a DNA duplex. The duplex was then run in the bulk heating experiment as described above. The melting temperatures were obtained by taking the maximum of the first derivative of the melting curves.

#### *4.4.4 Femtosecond laser pulse excitation of dsDNA-AuNP*

We used an amplified Ti:Sapphire laser system (Clark-MXR CPA) operating at a center wavelength of 775 nm, a 1 kHz repetition rate, and with a 150 fs pulse width. We frequency-doubled the pulse using a barium borate (BBO) crystal to generate a working excitation of 387.5 nm. The residual fundamental beam was removed with a dichroic mirror. The 387.5 nm excitation light beam was focused using a 1 m focal length lens to obtain a spot size of 3.3 mm diameter that did not change much over the 1 cm path length of the sample. The laser irradiance was controlled with a waveplate-polarizer combination. Samples (13 pM AuNP, 200 uL) were irradiated for a set amount of time then transferred into a microcentrifuge tube and centrifuged for 5 min

at 5000 x g. The supernatant was collected and measured using a Tecan Infinite M1000 plate reader. The Oregon Green 488 was excited at 465 nm and the fluorescence spectra was collected from 480 to 700 nm. The amount of DNA released was determined using a standardization curve (data not shown).

#### *4.4.5 Theoretical temperature profile generation*

The MATLAB code used to numerically determine the temperature profile around the AuNP after a fs laser pulse was previously developed by the Baffou group.<sup>36, 44</sup> The temperature profile for each pulse radiant exposure was determined using a 28 nm AuNP radius, 387.5 nm pulse wavelength, 150 fs pulse width, and an interface conductance value of  $300 \times 10^6 \text{ W/m}^2 \cdot \text{K}$ . This interface conductance value was chosen, as it is similar to AuNP-ligand interface conductance values reported in the literature.<sup>107, 124-125</sup> The temperature profiles are shown in Figure 4.6. The largest differences in the temperature profiles are seen in the initial 5 ns after the laser pulse.

#### *4.4.6 DNA dissociation equation modified for fs-laser pulse heating of AuNPs*

Fits were performed using Eq. 3.8 and 3.4 from Chapter 3. From the literature we identified values in the range of 32-49 kcal/mol for  $\Delta H_d^\#$  and 0.06-0.11 kcal/mol\*K for  $\Delta S_d^\#$  for DNAs of similar length tethered to AuNPs during bulk solution heating.<sup>16</sup> During the fitting, the  $\Delta H_d^\#$  and  $\Delta S_d^\#$  parameters were set within this range and  $\Delta H_d^\#$  and  $\Delta S_d^\#$  for each duplex species were globally fit regardless of linker length or pulse radiant exposure. Additionally, the percentage of the fast duplex species was globally fit for all pulse radiant exposures, but allowed to vary between the various linker lengths. The parameters used to obtain the sensed temperatures from the fits are as

follows: fast duplex species ( $\Delta H_d^\# = 33$  kcal/mol,  $\Delta S_d^\# = 0.065$  kcal/mol\*K), slow duplex species ( $\Delta H_d^\# = 37$  kcal/mol,  $\Delta S_d^\# = 0.072$  kcal/mol\*K). The percent fast duplex species was found to be  $18 \pm 3\%$ , in line with values previously reported in the literature.<sup>16, 114</sup> All fittings were performed in Origin software (Origin Lab).

## **Chapter 5: Understanding Femtosecond Pulse Excitation of Gold Nanoparticles for the Potential Thermal Enhancement of Surface Bound Enzymes**

### ***5.1 Introduction***

The use of NP scaffolds for the display of enzyme systems has shown promise as a cell-free alternative to bacterial based biosynthesis. It has been demonstrated that displaying enzymes on the surface of a NP can augment enzymatic activity.<sup>126</sup> In many cases, the NP acts to stabilize the enzyme and can provide a catalytic rate enhancement when compared to the free enzyme in solution.<sup>6, 53-55</sup> Yet, NP display does not always lead to an improvement in enzyme activity and the underlying physical mechanisms that give way to rate enhancements are system dependent.<sup>127</sup>

There is significant interest in combining the advantages of enzyme-NP immobilization with the photothermal properties AuNPs. In principle, a AuNP can be decorated with enzymes and excited by an external light source to induce localized heat dissipation from the AuNP and an increase in the temperature around the attached enzymes. Enzymatic activity is temperature dependent and typically increases with temperature until an optimum catalytic temperature is reached. For mesophilic enzymes, this typically falls between 20-45 °C. At higher temperatures enzymes begin to denature and lose catalytic function, essentially placing an upper bound on the temperature increase if activity enhancement is desired. This, of course, excludes the exceptional biology of acidothermophiles. The confined heating possible through fs



laser pulse excitation of AuNPs could be advantageous for control of a specific enzyme within a multienzyme cascade. Heat could be delivered to a target enzyme without affecting the activity of the other enzymes or substrates in the system. If we consider a two-enzyme cascade in solution where enzyme A has an optimum catalytic temperature at 45 °C and enzyme B denatures at 40 °C, one could envision this technique being applied to heat and increase the catalytic rate of enzyme A without denaturing enzyme B. Another potential application involves the confined heating of thermophilic enzymes. Thermophilic enzymes have optimum catalytic temperatures of 45-122 °C, making them difficult to efficiently integrate into cascades with mesophilic enzymes. If thermophilic enzymes can be locally heated without causing denaturation of other mesophilic enzymes in the cascade, the high catalytic rate of the thermophile can be accessed.

While a few reports have demonstrated enzyme catalytic enhancement through CW photothermal heating of AuNPs,<sup>128-131</sup> no work to date has utilized ultrafast laser pulsed heating of AuNPs for enzymatic enhancement. Interestingly, one group has utilized ns laser pulses to investigate the thermal denaturation of enzymes displayed on AuNPs (Figure 5.1A).<sup>30</sup> Here, the enzyme  $\alpha$ -chymotrypsin was displayed on AuNPs of different sizes and irradiated with pulse radiant exposures of 180-6090 J/m<sup>2</sup>. Pulse radiant exposures of this magnitude can cause the local temperature to increase by over 100 °C, which is much higher than the  $\alpha$ -chymotrypsin denaturation temperature of ~59 °C. The enzyme activation was quantified after irradiation (Figure 5.1B) and “impact zones” around the AuNPs were determined. While this work demonstrates that “molecular hyperthermia” can be used to locally denature functional proteins

within a larger system, it also serves as a basis for considering the more difficult objective of enzymatic enhancement.

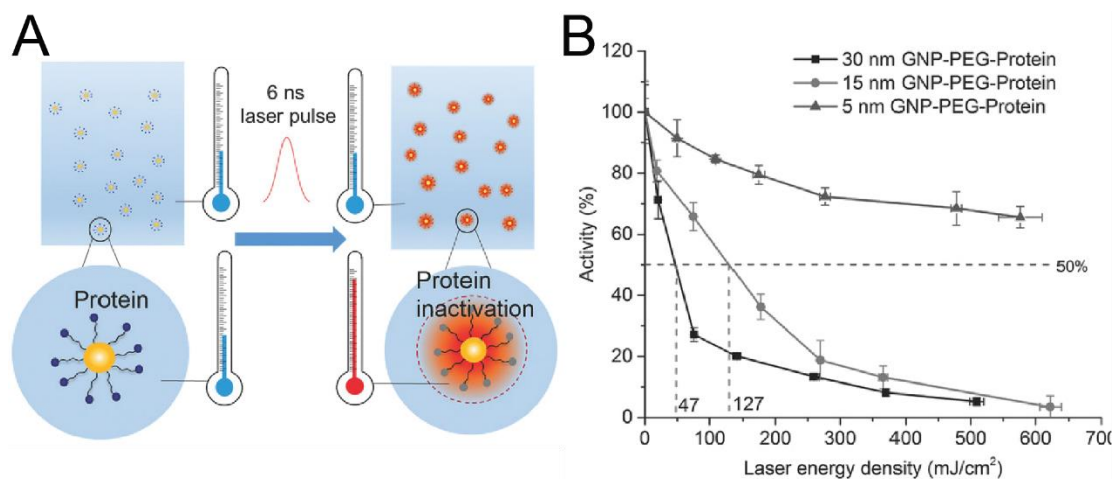


**Figure 5.1:** A) Schematic of ns laser pulse inactivation of  $\alpha$ -chymotrypsin. AuNPs (or GNPs) functionalized with  $\alpha$ -chymotrypsin are irradiated with a single pulse, causing a local temperature increase around the GNP. After heating, a proportion of the  $\alpha$ -chymotrypsin have been denatured, which depends on the laser energy density. B) Activity of  $\alpha$ -chymotrypsin after ns pulsed excitation of 5, 15, and 30 nm diameter GNPs. A 1 kDa polyethylene glycol (PEG) spacer was used to attach the protein ( $\alpha$ -chymotrypsin) to the GNP surface. Dashed lines correspond to the laser energy density that causes a 50 % reduction in activity. Reprinted (adapted) with permission from Peiyuan Kang, Zhuo Chen, Steven O. Nielson, Kenneth Hoyt, Sheena D’Arcy, Jeremiah J. Gassensmith, Zhenpeng Qin, *Molecular Hyperthermia: Spatiotemporal Protein Unfolding and Inactivation by Nanosecond Plasmonic Heating*, *Small*, 2017, 13, 1700841. Copyright 2017 WILEY-VCH Verlag GmbH & Co.

From Chapters 3 and 4, we determined that pulse radiant exposures of 3.5 to 14.1 J/m<sup>2</sup> cause dsDNA strands displayed on 55 nm diameter AuNPs to “sense” local temperatures ranging from 28 – 53 °C. Here, we sought to determine if these same temperature increases could augment enzymatic activity. To this end, we independently displayed two different enzymes, alkaline phosphatase (AP) and trypsin, on 55 nm

diameter AuNPs and performed an initial evaluation of the enzyme kinetics during irradiation.

## ***5.2 Fs laser pulse excitation of AuNPs for AP enhancement***

### *5.2.1 System design and characterization*

AP is a commercially produced dimeric enzyme that is typically used to remove phosphate groups from DNA and other biological substrates as a part of preparation protocols in molecular biology.<sup>132</sup> We have selected AP as a prototypical enzyme as it has a reduction in activity at temperatures above 45 °C.<sup>133</sup> Additionally, AP is readily available in our lab, and we have extensively characterized its activity previously while displayed on NPs and while free in solution.<sup>132</sup>

The AP enzyme was expressed and purified as previously reported.<sup>132</sup> AP was expressed with a terminal polyhistidine (His)<sub>6</sub>, which allows it to assemble to AuNPs displaying nitrilotriacetic acid (NTA) modified dithiolated ligands through metal affinity coordination following Ni<sup>2+</sup> addition. A schematic of the conjugation strategy is shown in Figure 5.2A. 55 nm AuNPs were synthesized as described in Chapter 3. Using a 50-50 ratio of thioctic acid (TA) and TA-NTA ligands was previously found to provide optimal colloidal stability and enzyme conjugation.<sup>134</sup> To confirm AP loading onto AuNP, AP was labeled with Alexa Flour 532 C5 maleimide (AF532) and incubated with AuNP in the presence or absence of Ni<sup>2+</sup>. The AuNP concentration was fixed at 13 pM and the Ni<sup>2+</sup> concentration was 5-fold higher than the AP concentration. All samples were run in 50 mM HEPES, pH 7.5 with 0.5 mM MgCl<sub>2</sub>. In Figure 5.2B the quenching of AF532-AP through ET to the AuNP surface is shown for various AP:AuNP ratios. Quenching was determined by comparing samples with Ni<sup>2+</sup> to

samples of the same AP:AuNP ratio without  $\text{Ni}^{2+}$ . Clearly, the addition of  $\text{Ni}^{2+}$  facilitates AP loading. At a ratio of 50:1 AP:AuNP, we estimate that  $52 \pm 7\%$  of the AP was attached to the TA-NTA- $\text{Ni}^{2+}$  ligands, and this loading ratio was used throughout the rest of this work.

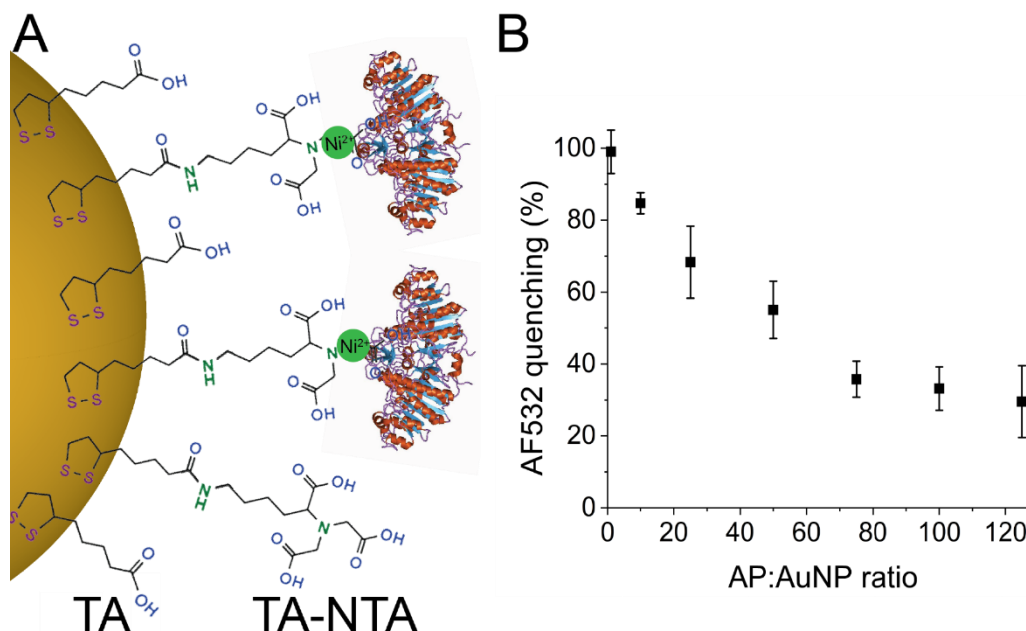


**Figure 5.2:** A) Schematic of a 55 nm diameter AuNP displaying AP (not to scale). AuNP is coated with a 50:50 ratio of thioctic acid (TA) and TA-nitrilotriacetic acid (NTA) ligands. AP is added to AuNP solution with a 5-fold excess of  $\text{Ni}^{2+}$  ions to promote conjugation of the AP terminal His<sub>6</sub> through metal affinity coordination. B) Fluorescence quenching of Alexa Fluor (AF532) labeled AP through ET with the AuNP. Quenching values are determined by comparing samples of the same AP:AuNP ratio, with and without  $\text{Ni}^{2+}$ . AP structure reprinted from “Reaction Mechanism of Alkaline Phosphatase based on Crystal Structures: Two-metal Ion Catalysis”, Kim, E. E.; Wyckoff, H. W., Journal of Molecular Biology 1991, 218 (2), 449-464. Copyright 1991, with permission from Elsevier.

Next, the kinetic activity of AP was examined when displayed on the AuNPs and when free in solution. The AP concentration is fixed at 650 pM and the AuNP concentration at 13 pM (if present). All samples were run in 50 mM HEPES, pH 7.5

with 0.5 mM MgCl<sub>2</sub> and 3.25 nM Ni<sup>2+</sup>. The substrate 4-methylumbelliferyl phosphate (MUP) was utilized in all kinetic assays. AP acts to remove the phosphate group from MUP, forming the fluorescent product 4-methylumbelliferyl (MU). Monitoring the emission of MU (peak excitation at 386 nm and emission at 448 nm) provides a simple method to readout AP activity. A representative fluorescent spectrum of MU is provided in Figure 5.3A. We utilize the well-known Michaelis-Menten (MM) model of enzyme kinetics to examine the effect of AP loading onto AuNPs. In the MM model, the enzymatic reaction steps are described as:



where E is enzyme, S is the substrate, ES is the enzyme-substrate complex, P is the product,  $k_1$  is the association rate and  $k_{-1}$  is the dissociation rate of the E and S, and  $k_{cat}$  is the enzyme turnover number.<sup>132</sup> When working at a fixed enzyme concentration and at an excess substrate concentration, the initial reaction velocity can be expressed as:

$$V \cong \frac{k_{cat}e_0s_0}{K_M + s_0} \quad (\text{Eq. 5.2})$$

where  $K_M = (k_{-1} + k_{cat}) / k_1$  (the Michaelis-Menten constant),  $e_0$  is the enzyme concentration, and  $s_0$  is the initial substrate concentration. At high enough substrate concentrations, the reaction will reach a maximum velocity and Eq. 5.2 can be written as:

$$V_{max} = k_{cat}e_0 \quad (\text{Eq. 5.3})$$

By obtaining the initial reaction velocity for a fixed  $e_0$  over a range of substrate concentrations (in excess to  $e_0$ ), Eq 5.2 can be fit to the data and the  $k_{cat}$  and  $K_M$  values can be extracted.

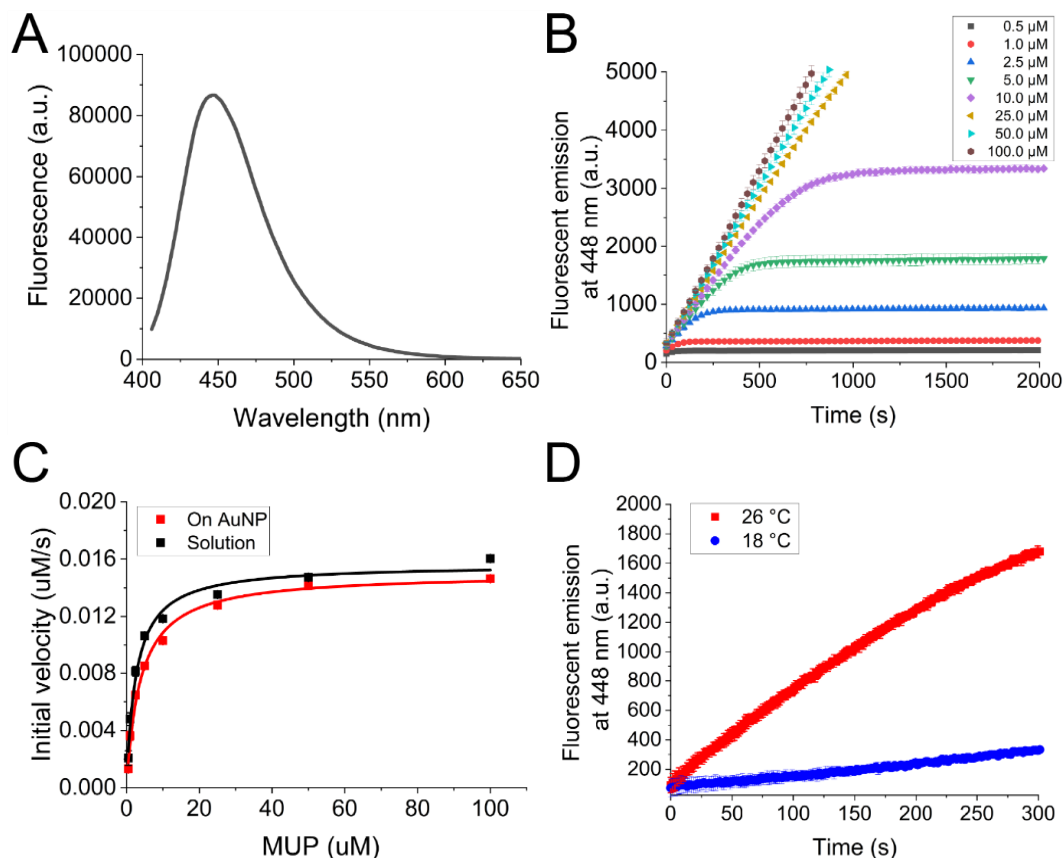


**Figure 5.3:** A) Representative fluorescent spectrum of the product MU excited at 386 nm. B) MU production over time for AP-AuNP at initial MUP concentrations ranging from 0.5 to 100  $\mu\text{M}$ . The initial (linear) portion of the production curves were used to obtain the slope or initial velocity of the enzyme reaction at a given substrate concentration. C) Michaelis-Menten (MM) plots of AP-AuNP and AP in solution. On AuNP  $k_{cat}$ ,  $K_M$  ( $15.0 \pm 0.6 \text{ s}^{-1}$ ,  $3.8 \pm 0.4 \mu\text{M}$ ). Solution  $k_{cat}$ ,  $K_M$  ( $15.7 \pm 0.5 \text{ s}^{-1}$ ,  $2.6 \pm 0.3 \mu\text{M}$ ). D) Temperature dependent activity of the AP-AuNP conjugate.

Figure 5.3B, displays MU production over time for AP-AuNP at initial MUP concentrations ranging from 0.5 to 100  $\mu\text{M}$ . The initial (linear) portion of the

production curves were used to obtain the slope or initial velocity of the enzyme reaction at a given substrate concentration. The same analysis was performed on the production curves for AP in solution. Initial velocities were then fit to Eq. 5.2 (Figure 5.3C) to obtain  $k_{cat}$  and  $K_M$ . We report that the  $k_{cat}$  value of AP is unchanged when displayed on the AuNP ( $15.7 \pm 0.5 \text{ s}^{-1}$  for solution and  $15.0 \pm 0.6 \text{ s}^{-1}$  for AP-AuNP). Interestingly, the  $K_M$  increased from  $2.6 \pm 0.3 \text{ }\mu\text{M}$  to  $3.8 \pm 0.4 \text{ }\mu\text{M}$  (decreased enzyme-substrate affinity). While the exact mechanism behind this decreased affinity is unknown, we speculate that electrostatic interactions between the MUP and AuNP local environment play a significant role. For the purposes of this work, we are merely interested in confirming that the AP is functional on the AuNP surface and as such we have not investigated the decreased substrate affinity further.

Finally, we confirmed the temperature dependent activity of the AP-AuNP conjugate. Samples consisted of 13 pM AuNP with 650 pM AP (50 AP:AuNP) in 50 mM HEPES, pH 7.5 with 0.5 mM  $\text{MgCl}_2$  and 3.25 nM  $\text{Ni}^{2+}$ . Using a MUP concentration of 10  $\mu\text{M}$ , the MU production was monitored over time at bulk solution temperatures of 18 °C and 26 °C (Figure 5.3D). When the solution temperature was dropped from 26 °C to 18 °C the initial rate of MU production dropped by over 10-fold, confirming the temperature dependence of the enzyme kinetics.

### 5.2.2 *Fs laser pulse irradiation of AP-AuNP*

The laser system utilized in these experiments is the same as described in Chapters 3 and 4. During laser assays, the AuNP concentration was fixed at 13 pM and the AP concentration at 650 pM. The initial MUP concentration was 10  $\mu\text{M}$ . All samples were

run in 50 mM HEPES, pH 7.5 with 0.5 mM  $\text{MgCl}_2$  and 3.25 nM  $\text{Ni}^{2+}$ . As in Chapter 3, we restricted the sample volume to 200  $\mu\text{L}$  so that the laser interacted with the whole sample during irradiation. After the reaction was run for a given amount of time, the reaction was quenched by the addition of 1800  $\mu\text{L}$  of 0.05 M Ethylenediaminetetraacetic acid (EDTA).

In the first experiment, three independent samples were run for 5 total minutes with either 0, 2, or 4 mins of laser exposure at  $7.1 \text{ J/m}^2$  (Figure 5.4A). We observed a decrease in MU signal as the time in the laser increased. Next, we investigated AP activity with and without laser exposure to determine if AP denaturation was occurring during irradiation. During these experiments, no MUP was present during irradiation. After irradiation, 10  $\mu\text{M}$  MUP was added to a sample of AP-AuNP that had been exposed to  $14.1 \text{ J/m}^2$  for 2 mins and to a sample of AP-AuNP that was not exposed to the laser. The initial velocities of these two samples are shown in Figure 5.4B. We report no significant difference between the initial rates of these samples, indicating AP was not denatured during laser heating. Finally, we investigate the photostability of MUP. 10  $\mu\text{M}$  MUP was predigested and introduced to the laser at  $14.1 \text{ J/m}^2$  for either 0 s, 60 s or 120 s (Figure 5.4C). We observed a reduction in MU signal over time, indicating that photobleaching is occurring. This finding also explains the decrease in MU signal with more time in the laser observed for the complete enzymatic reaction (Figure 5.4A).

As we observed MU photobleaching, we decided to investigate the enzyme trypsin as an alternative in the context of fs laser pulse heating. Trypsin is a type of protease,



one of the most prevalent enzyme groups in the human genome,<sup>135</sup> and functions by hydrolyzing peptide bonds in protein/peptide substrates.<sup>67</sup> Utilizing trypsin expressing

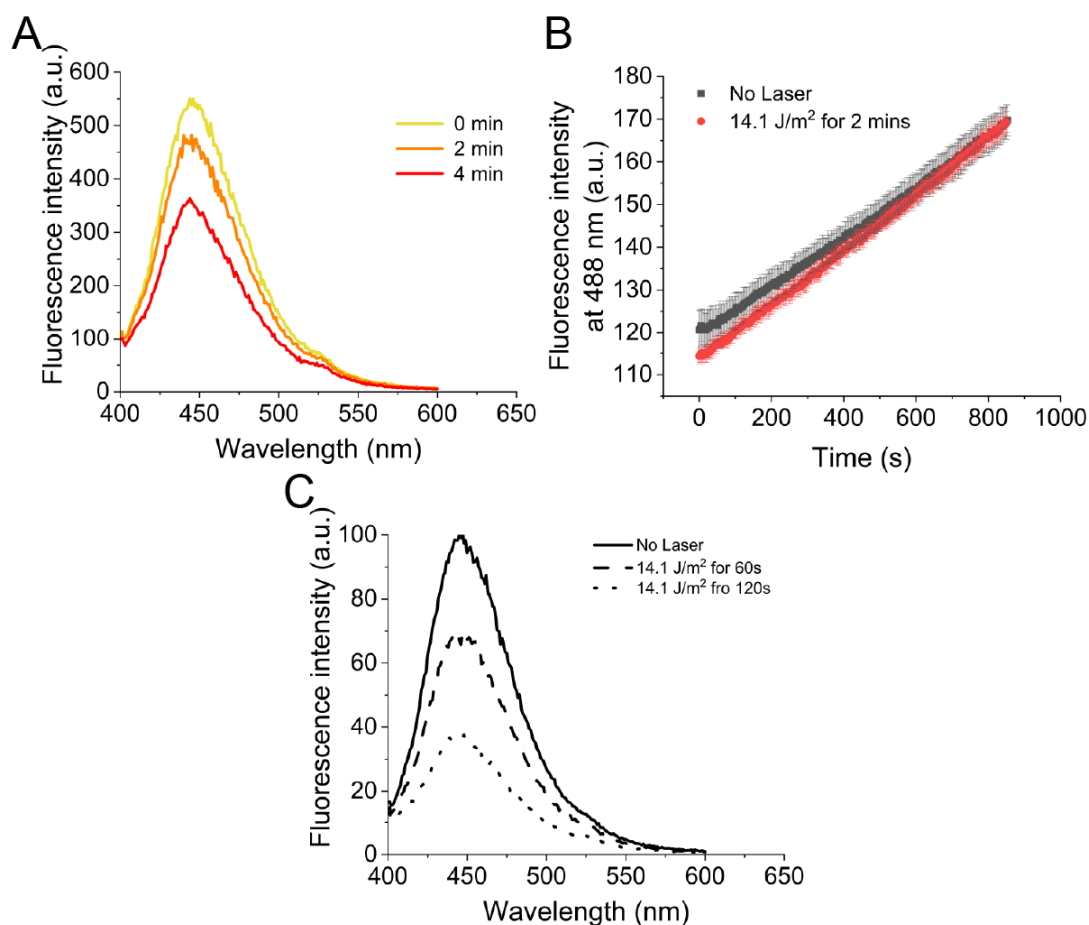


**Figure 5.4:** A) MU production by AP-AuNP during irradiation at 7.1 J/m<sup>2</sup>. All samples were run for 5 mins total with either 0, 2, or 4 mins of laser exposure. B) Initial rate of AP-AuNP with and without laser exposure at 14.1 J/m<sup>2</sup> for 2 mins. After irradiation, 10  $\mu$ M MUP was added to a sample and the activity was recorded. C) Predigested MUP (*i.e.*, MU) irradiated at 14.1 J/m<sup>2</sup> for 0 s, 60 s, or 120 s.

a terminal His<sub>6</sub>, we used the same TA-NTA-Ni<sup>2+</sup> conjugation strategy used for AP. To monitor trypsin activity, we ordered a custom fluorogenic peptide substrate (ANASPEC<sup>TM</sup>). Unfortunately, we again observed photobleaching of the substrate/product in this system. Currently, we are in the process of identifying

potential substrates for both AP and trypsin that are not damaged by the laser pulses at 387.5 nm.

### *5.2.3 Fs laser pulse irradiation of AP displayed on gold nanorods*

In the previous section and Chapters, the laser system utilized a BBO crystal to frequency double the pulse and generate a working excitation wavelength of 387.5 nm as this wavelength was capable of exciting spherical AuNPs. The use of spherical AuNPs allowed for a more thorough analysis of the temperature profiles (due to symmetry) after fs laser pulse excitation and were chosen for this reason. Yet, the use of the 387.5 nm excitation wavelength is incompatible with the fluorogenic substrates examined here. To avoid potential substrate damage, we decided to try and utilize the fundamental wavelength of the Ti:Sapphire laser system at 775 nm. As the 55 nm AuNPs utilized in the previous sections do not absorb light here, we switched to gold nanorods (AuNRs) with a length of 45 nm and diameter of 10 nm. The AuNRs were purchased from NanoPartz<sup>TM</sup> and have a localized plasmonic resonance peak at 844 nm (Figure 5.5A). AuNRs were functionalized with the same 50-50 ratio of TA and TA-NTA ligands used for enzyme attachment. AP attachment was performed as described for the AuNP system.

Using Eq. 1.3, we determined the initial theoretical temperature increase of the AuNR at a pulse radiant exposure of  $14.1 \text{ J/m}^2$ . The initial temperature increase of the AuNR was over 400 °C. It is important to note that this value represents an upper limit as it assumes an interface conductivity value of zero. For comparison, the initial theoretical temperature increase for the 55 nm diameter AuNPs is ~330 °C, yet this

value is reduced to  $\sim 200$  °C when calculated with an interface conductivity value of  $300 \times 10^6$  W/m<sup>2</sup>K. Due to the asymmetrical nature of AuNRs, we are unable to perform this calculation with them.

First, we verified the colloidal stability of the AP-AuNR during irradiation at a pulse radiant exposure of  $14.1$  J/m<sup>2</sup> for 2 mins (Figure 5.5A). The absorbance of AP-

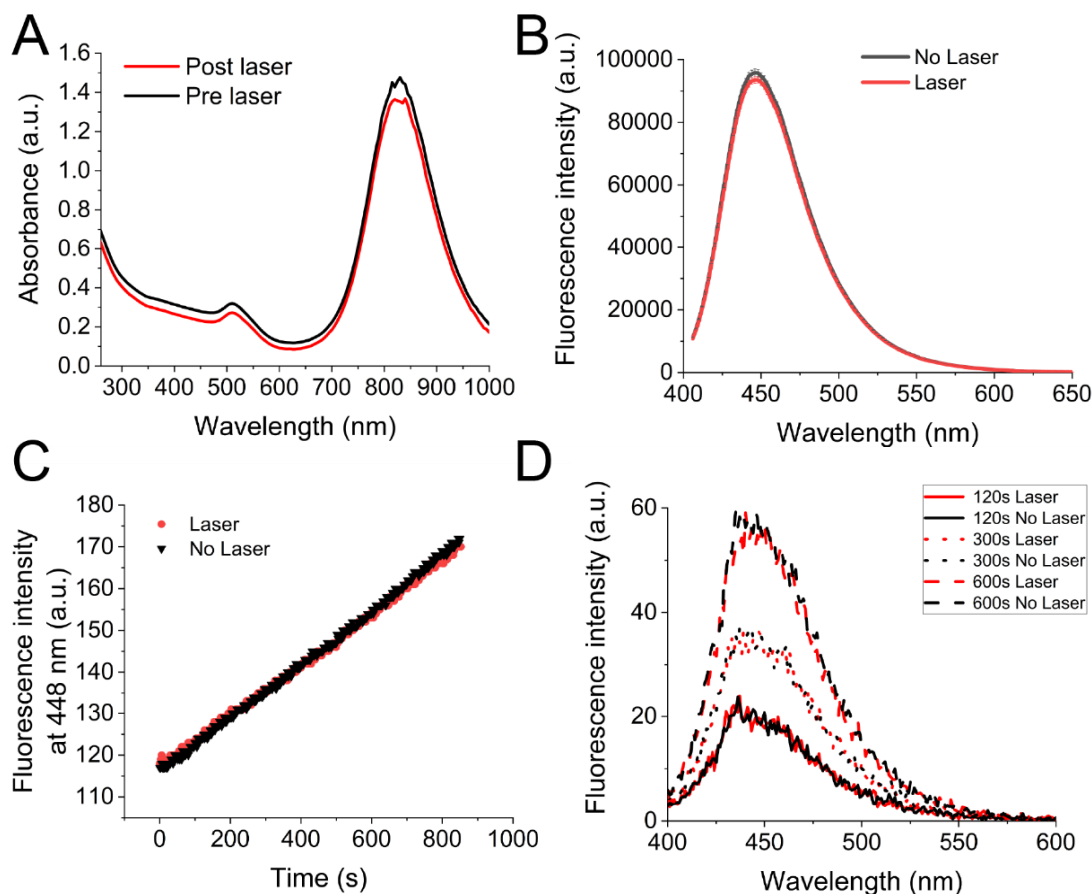


**Figure 5.5:** AP-AuNR system with 775 nm excitation. A) AP-AuNR stability after irradiation at a pulse radiant exposure of  $14.1$  J/m<sup>2</sup> for 2 mins. B) MU photostability during irradiation at  $14.1$  J/m<sup>2</sup> for 4 mins. C) Initial velocity of AP-AuNR with  $10$   $\mu$ M MUP. Laser sample (red) was irradiated at  $14.1$  J/m<sup>2</sup> for 2 mins before being added to MUP. D) AP-AuNR activity during optical heating. Sample temperature was set to  $12$  °C so that the AP activity would be minimal in between laser pulses. Samples were irradiated at  $14.1$  J/m<sup>2</sup> for either 120, 300 or 600 s (red) and compared to samples held at  $12$  °C without irradiation (black).

AuNR was measured before irradiation (black) and after irradiation (red). We observed no change in the AuNR, indicating they were colloidal stable after irradiation. Secondly, we verified the MU was not photobleached during irradiation (Figure 5.5B). 10  $\mu$ M MU was irradiated at 14.1 J/m<sup>2</sup> for 4 mins and compared to a 10  $\mu$ M MU control sample (no laser). We report no photobleaching of MU from irradiation at 775 nm. Finally, we tested for AP denaturation during irradiation at 14.1 J/m<sup>2</sup> for 2 mins (Figure 5.5C). In this experiment no MUP was present during irradiation. After irradiation, the sample of AP-AuNR was introduced to 10  $\mu$ M MUP and the initial velocity was compared to a control sample of AP-AuNR (no laser). We observed no change in the AP activity from irradiation. After confirming laser compatibility with the AP-AuNR system, we tested if the AP activity could be enhanced from optical heating. To do this, we placed samples in temperature-controlled cuvette and lowered the temperature to 12 °C so that the AP activity would be minimal in between laser pulses. Samples were irradiated at 14.1 J/m<sup>2</sup> for either 120, 300 or 600 s and compared to samples held at 12 °C without irradiation. We observed no increase of AP activity during irradiation (Figure 5.5D).

### ***5.3 Expected enzyme enhancement during fs laser pulse heating of AuNPs***

As we were unable to demonstrate enzyme enhancement with the systems described above, we decided to mathematically investigate enzyme enhancement through fs laser pulse heating of AuNP in an attempted to understand and rationalize our observed experimental results.

We first assume that there will always be enzyme activity occurring in between heating pulses. This assumption holds even when the solution temperature is chilled to 12 °C, as seen in the control samples (black) in Figure 5.5D. During non-heating or cooling periods, the enzyme production formation ( $P_c$ ) can be represented as:

$$P_c = V_c t_c \quad (\text{Eq. 5.4})$$

where  $V_c$  is the product formation rate during cooling and  $t_c$  is the total cooling time. During heating times the enzyme production formation ( $P_H$ ) can be represented as:

$$P_H = V_H t_H \quad (\text{Eq. 5.5})$$

where  $V_H$  is the product formation rate during heating and  $t_H$  is the total heating time. The total heating time  $t_H$  is dependent on the laser repetition rate ( $f$ ), total assay time ( $t$ ) and the duration of the temperature increase after a single pulse ( $t_p$ ). As such  $t_H$  can be expressed as:

$$t_H = t_p f t \quad (\text{Eq. 5.6})$$

Subsequently, the total cooling time  $t_c$  can be expressed as:

$$t_c = t - t_H = t(1 - t_p f) \quad (\text{Eq. 5.7})$$

We then rewrite the product formation during cooling ( $P_c$ ) and production formation during heating ( $P_H$ ) as:

$$P_c = V_c t(1 - t_p f) \quad (\text{Eq. 5.8})$$

$$P_H = V_H t_p f t \quad (\text{Eq. 5.9})$$

Combining Eq. 5.8 and 5.9 we can express the total product formation during laser pulsed heating ( $P_T$ ) as:

$$P_T = P_C + P_H = [V_C t(1 - t_p f)] + [V_H t_p f t] \quad (\text{Eq. 5.10})$$

When no laser irradiation is present (*i.e.*, a control sample) the product formation  $P_N$  can be expressed as:

$$P_N = V_C t. \quad (\text{Eq. 5.11})$$

Then we can express the % increase in production formation from laser pulsed heating (with respect to the control sample) as:

$$\% \text{ increase} = 100 * \frac{P_T - P_N}{P_N} = 100 * t_p f \left( \frac{V_H}{V_C} - 1 \right) \quad (\text{Eq. 5.12})$$

In Chapter 3, the duration of the temperature increase after a single pulse ( $t_p$ ) was determined to be 5 ns. In Figure 5.6, the % increase in production formation is displayed graphically for various laser repetition rates and a  $t_p$  value of 5 ns (excluding the dashed lines). The ratio of  $V_H$  to  $V_C$  is displayed on the x-axis. For our system (1 kHz repetition rate), almost no % increase in product formation can occur even for high ratios of  $V_H$  to  $V_C$ . This is because the total heating time is extremely small (5  $\mu$ s of heating during 1 second of assay time). This explains why we observe no enhancement during irradiation in our system. Clearly, as the repetition rate increases, the amount of heating time increases, giving rise to a larger increase in product formation. Yet, the choice of laser repetition rate is highly application dependent as the degree of spatial confinement (Eq. 1.7, Chapter 1) and temporal confinement decrease with an increase in the laser repetition rate.

The dashed traces in Figure 5.6 represent systems with a  $t_p$  value of 20 ns (100 kHz and 500 kHz). Comparing these traces to the corresponding traces with  $t_p$  values of 5 ns, it is evident that an increase in the single pulse heating duration corresponds to

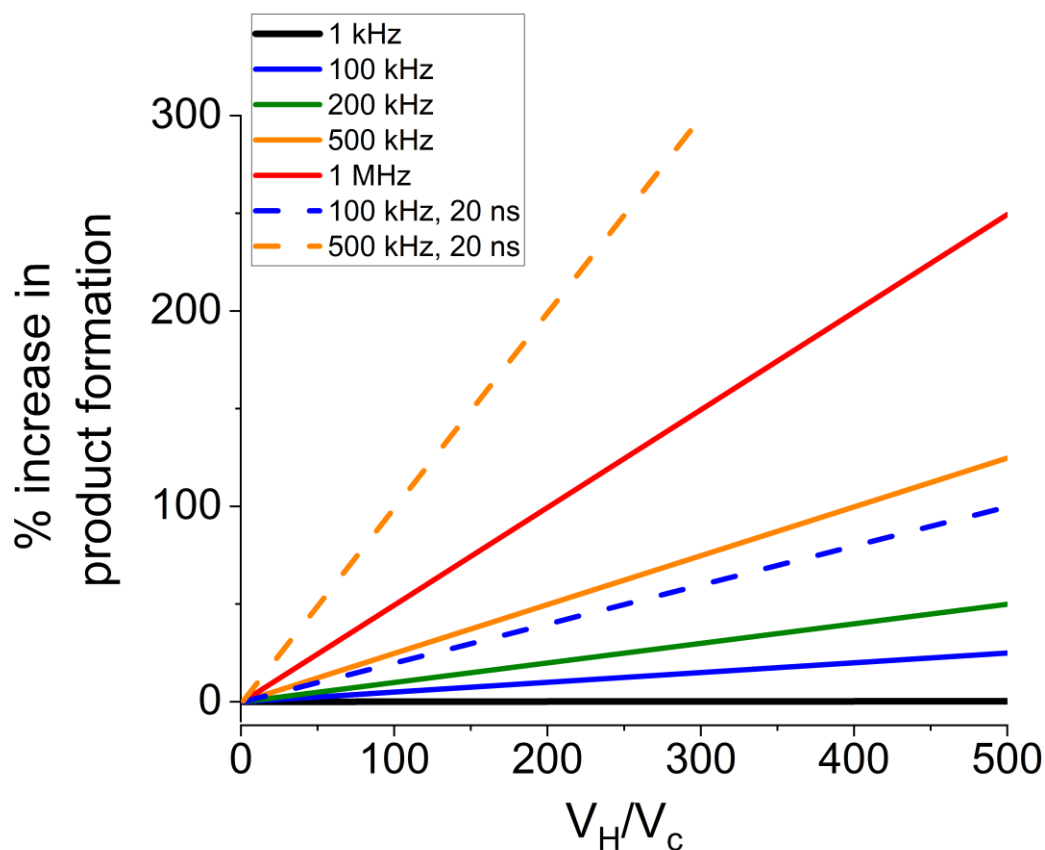


**Figure 5.6:** Percent increase in product formation during ultrafast laser pulse photothermal heating of AuNPs. Traces based off of Eq. 5.12. All traces assume a single pulse heating duration of 5 ns, except for when a single pulse heating duration of 20 ns is noted in the legend.

a large increase in the percent product formation. This indicates that the interface conductance value of AuNPs could be engineered to increase the heating duration after a single pulse. This could potentially be done through ligand choice, polymer

encapsulation, or even the use of composite NPs. Additionally, the use of a ns laser pulse would increase the single pulse heating duration.

From Figure 5.6, we observe a clear linear relationship between the ratio of  $V_H$  to  $V_C$  and the % increase in product formation. While the value of  $V_C$  is easily obtained from steady state analysis, it is not yet understood how enzymes react to the confined and short temperature increases generated through this type of heating, making  $V_H$  hard to estimate. From Chapters 3 and 4 we found that the high temperatures near the AuNP surface caused the DNA to denature faster than predicted theoretically, so we can make a general hypothesis that the average temperature around the enzyme would be a good predictor for a lower bound of  $V_H$ .

For typical mesophilic enzymes, increasing the temperature from 20 °C to 60 °C will increase the reaction rate by ~20 fold (assuming the enzyme does not denature at 60 °C).<sup>136</sup> In the context of pulsed heating, we assume that the solution temperature is 20 °C and the 5 ns average temperature around the enzyme during heating is 60 °C. This correlates to a modest ~10 % increase in product production at a 1 MHz repetition rate. If the temperature increase is from 0 °C to 60 °C the reaction rate will typically increase by ~150 fold.<sup>136</sup> This correlates to a ~8 % increase in product production at 100 kHz, a ~37 % increase for 500 kHz and a ~75 % increase for 1 MHz. From this analysis, we conclude that ultrashort laser pulse photothermal heating of enzymes is best suited to enhance enzymatic activity in low temperature environments.

Thermophilic enzymes are of interest for ultrashort laser pulse photothermal heating as locally heating them to their optimum temperatures could enable their



integration into multienzyme cascades containing mesophilic enzymes. For thermophilic enzymes, an increase in the temperature from 0 °C to 80 °C can increase the reaction rate by up to ~2900 fold and from 20 °C to 80 °C by ~400 fold.<sup>136</sup> This would correlate to a 145 % and 20 % increase in production formation at a 100 kHz repetition rate, respectively, indicating that even at relatively low repetition rates thermophilic enzymes are a prime candidate for ultrashort laser pulse photothermal heating.

#### ***5.4 Conclusions***

We investigated the possibility of enzyme enchantment through fs laser pulse excitation of AuNPs using two enzymes (AP and trypsin). We found that our excitation wavelength of 387.5 nm photobleached both fluorogenic products for AP and trypsin, making activity detection unfeasible. We then utilized an excitation wavelength of 775 nm to irradiate AuNRs displaying AP. Here, we observed no kinetic enhancement, which lead us to mathematically determine the theoretical enhancement in our system. In doing so, we put forth an equation (5.12) that allows for the calculation of the theoretical % increase in product formation during laser pulse heating. This equation is dependent on the laser repetition rate, the single pulse heating duration and the ratio of  $V_H$  to  $V_C$ . We found that using our 1 kHz repetition rate laser system with mesophilic enzymes would only provide a 1 % increase in product production, explaining the lack of enhancement observed in our experimental system. It is also evident from our analysis that laser systems should be operated at a repetition rates of 100 kHz or higher if a significant enhancement in enzyme production is desired. Unfortunately, we do not have access to a system that can achieve these repetition rates and provide a high

enough pulse radiant exposure to generate a sufficient temperature local increase. We also propose that thermophilic enzymes are a prime candidate for this technique and as such are the focus of our future work. While we were unable to demonstrate enzyme enhancement, the work performed here provides key insights that should contribute to the design of these systems in the future.

## **Chapter 6: Peptide nucleic acids as a selective and highly efficient alternative for conjugating quantum dots to DNA nanostructures\***

\*Reprinted (adapted) with permission from Christopher M. Green<sup>#</sup>, David A. Hastman<sup>#</sup>, Divita Mathur, Kimihiro Susumu, Eunkeu Oh, Igor L. Medintz, and Sebastián A. Díaz, Direct and Efficient Conjugation of Quantum Dots to DNA Nanostructures with Peptide-PNA, *ACS Nano*, 2021. Copyright 2021 American Chemical Society.

<sup>#</sup> Authors contributed equally. The initial idea for this work was proposed by myself (David Hastman). At the start of the project, a significant effort was made by myself utilizing a DNA origami triangle rather than the breadboard structure utilized in the manuscript. While we were able to demonstrate the feasibility of this technique using the DNA origami triangle, a collaboration with Dr. Christopher Green enabled us to greatly improve the quality of our work and our understanding of the system. As such, much of the initial work performed by myself was not included in the manuscript. The work presented in this Chapter was led by Dr. Green and he performed a majority of the experimental assays and data analysis. As I came up with the concept of the system, performed a majority of the initial experiments, and assisted with the work presented in here, I decided to include it in my dissertation.

### **6.1 Introduction**

While the primary focus of this dissertation is the confined photothermal heating of NP displayed biomaterials, equipment limitations and significant COVID19 restrictions shifted our efforts towards other research projects. One of these efforts, was focused on a novel class of biomaterials known as peptide nucleic acids (PNA). PNAs are a synthetic DNA alternative where the sugar-phosphate backbones are replaced by *N*-(2-aminoethyl)glycine-based polyamide moieties.<sup>137</sup> This synthetic approach, first described in the early 90s by Nielsen *et al.*,<sup>138</sup> combines the properties of peptides and DNA. The resulting PNA have increased chemical and enzymatic stability and demonstrate higher affinity to complementary nucleic acids than DNA, all while still

maintaining base-pairing rules.<sup>139-141</sup> The higher affinity leads to an increased duplex melting temperature (up to tens of °C for small 14 bp strands) for both PNA-PNA duplexes and PNA-DNA duplexes. Because of the increased stability and affinity to DNA, PNAs have been utilized in DNA nanostructures as a means of increasing stability,<sup>142-143</sup> integrating peptides,<sup>144-145</sup> and enhancing antigen display.<sup>146</sup> Here, we look to build upon this work by utilizing PNA-DNA hybridization as a method to efficiently and specifically capture NPs on the surface of a DNA nanostructure.

DNA nanostructures have grown into a powerful tool capable of creating virtually any 2- and 3-D shape through a variety of design strategies. Utilizing novel synthetic scaffolds beyond the classical M13mp18<sup>147</sup> or exploiting the DNA brick methodology pioneered by Ke *et al.*<sup>148</sup>, the size of feasible structures has increased to many hundreds of nanometers.<sup>149</sup> Similarly, the application of these nanostructures has expanded to multiple fields such as drug delivery, biosensors, theranostics, molecular computing, and light harvesting among others.<sup>68, 150-151</sup> The conjugation of inorganic NPs onto DNA nanostructures is a crucial component of many of these technologies, as DNA alone does not possess the distinctive physical properties (plasmonic, photonic, electrochemical, magnetic, etc.) that various NPs possess.<sup>7</sup> Rather, DNA nanostructures have functionality as scaffolds for arranging NPs, enabling the assembly of a rapidly expanding variety of discrete NP devices. Some of the more common NPs conjugated to DNA nanostructures include metals [Au, Ag, Al, Cu, Pd, Pt],<sup>152-153</sup> Si and SiO<sub>2</sub>,<sup>154</sup> iron oxides,<sup>155</sup> semiconductor quantum dots (QDs),<sup>156</sup> and carbon nanostructures.<sup>157</sup> DNA nanotechnology can place multiple NPs with orientation and separation that approach single nm precision, on par with current state-of-the-art

lithography at the level of individual devices, and this capability spans from discrete nanostructures up to NP superstructures.<sup>158</sup>

As discussed in Chapter 2, the most common NP-DNA combination is the use of AuNPs conjugated by thiolated DNA. Applications of DNA-AuNPs have become popular because they possess a unique combination of desirable properties, such as chemical inertness, biocompatibility, strong localized surface plasmon resonance, local photothermal heating, and extensive size and shape variability.<sup>114, 159-160</sup> Yet, not all NPs are readily modified with DNA, in some cases requiring costly (both in time and cost) chemical modifications of the DNA for the NP conjugation. Furthermore, the increased chemical, enzymatic, and thermal stability of PNA could be leveraged for biosensor design or even photothermal heating applications.

In the past our group and others have utilized a DNA-peptide hybrid to conjugate QDs to DNA nanostructures.<sup>161-163</sup> The peptide was composed of a linker section along with His<sub>6</sub>-tag, which self-assembles on the QD surface through metal coordination to the Zn<sup>2+</sup> ions on the QD surface.<sup>7</sup> Despite the efficacy of this strategy and the specificity of placement that it enables on DNA nanostructures, hybrid DNA-peptides are hard to synthesize and economically limiting. In comparison, PNAs are also significantly more amenable to direct synthesis with a peptide portion than DNA and as a result cost significantly less.

In this Chapter, we demonstrate that peptide-PNA hybrids can be designed to self-assemble to CdSe/CdS/ZnS QDs of varying sizes and promote site specific binding of QDs to ssDNA tethers on a DNA origami breadboard. With this technique, we achieved

labeling efficiencies greater than 90 %, rivaling QD-conjugation techniques of significantly greater complexity and/or ligand bulk. Labeling efficiency was quantified through atomic force microscopy (AFM), transmission electron microscopy (TEM), and Förster resonance energy transfer (FRET). We further investigated the effects of PNA conjugation density, net charge of peptide-PNAs, and ratio of QDs to capture sites on labeling efficiency, and we used the results to enable efficient, site-specific capture of QDs with varied diameters on the same DNA template.

## **6.2 Results and discussion**

### *6.2.1 Peptide-PNAs and QD conjugation*

Peptide-PNA strands were obtained from commercial sources (PNA-Bio Inc., Thousand Oaks, CA) with 4 variations of peptide and 2 unique PNA sequences as detailed in Table 6.1 and Figure 6.1. Two peptide-PNAs were purchased initially, and additional variations of the peptide were acquired later to investigate the role of peptide charge on QD stability and capture efficiency of QDs on a DNA origami. Herein, peptide-PNAs will be notated as  $PX^Y$ , where X indicates the PNA sequence, and Y indicates the net charge of the peptide-PNA at pH 7.5. A peptide-DNA was also used for comparison and is indicated as DX, where X indicates the DNA sequence. Each peptide-PNA has three functionally distinct domains - (1) the His<sub>6</sub>-tag, a 6 residue terminal domain of the peptide consisting of 6 histidines which facilitates conjugation to QDs, (2) a 6 residue spacer domain that could be modified to introduce functionally active peptides (e.g., arginine or lysine for enzymatic cleavage by trypsin) and also plays a role in presentation of the PNA, and lastly (3) a 14 nucleotide (nt) PNA which

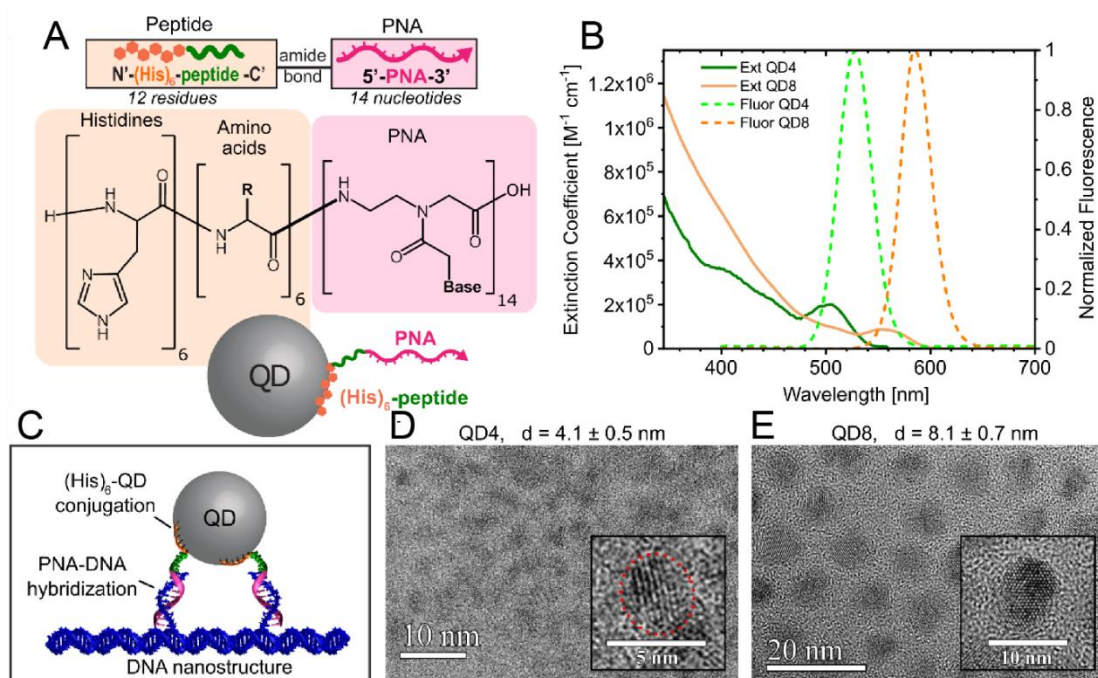


**Figure 6.1:** Peptide-PNA conjugation to QDs. A) Chemical formula of peptide-PNA and depiction of peptide-PNA conjugation to a QD. The peptide-PNA consists of three unique domains - the His<sub>6</sub>-tag (orange), the interior peptide spacer (green), and the PNA (pink). The PNA is bound to the spacer peptide by an amide bond and has a length of 14 nt. B) Extinction coefficient and normalized fluorescence spectra of QD4 (green) and QD8 (orange) in 50 mM HEPES at pH 7.5. Emission peaks occurred at 527 nm and 585 nm, respectively. Both QDs were excited at 350 nm for fluorescence measurements. C) Depiction of a QD bound to a DNA nanostructure by PNA-DNA hybridization. TEM images of D) QD4 and E) QD8 with enlarged inset images showing a representative QD. QD4 is outlined in red to aid visualization due to the low contrast of the image.

facilitates highly specific interactions with DNA breadboards through PNA-DNA hybridization (Figure 6.1). Specific QD-peptide-PNA constructs will be later referenced as QDz:PX<sup>Y</sup>, where QDz identifies the QD used and PX<sup>Y</sup> the peptide-PNA. All QDs (CdSe/CdS/ZnS) were synthesized in-house with protocols reported previously and had diameters of  $4.1 \pm 0.5$  nm (QD4) and  $8.1 \pm 0.7$  nm (QD8) prior to

the addition of capping ligands (Figure 6.1) as determined by TEM analysis.<sup>164</sup> Absorbance and emission spectra for QD4 and QD8 are provided in Figure 6.1C. The QDs had emission maxima of 527 nm and 585 nm, respectively. The QDs were made colloiddally stable by surface functionalization with the short CL4 zwitterionic surface ligand which has been previously shown to provide optimal stability and accessibility for the His<sub>6</sub>-tags on the peptides.<sup>164</sup> The His<sub>6</sub>-tag conjugation has also been demonstrated to be compatible with other QD surface ligands, including PEGylated systems.<sup>165</sup>

Name	Sequence	Approx. Charge	MW	Cost
	N-C, 5'-3'	e (pH 7.5)	Da	\$/nmole
P1 <sup>3+</sup>	HHHHHHAGSRRC:TATGATTTGTCTAG	+3	5285	11.64
P1 <sup>1+</sup>	HHHHHHAGSGGC:TATGATTTGTCTAG	+1	5087	11.64
P1 <sup>1-</sup>	HHHHHHADSRED:TATGATTTGTCTAG	-1	5328	11.64
P1 <sup>3-</sup>	HHHHHHEDDRED:TATGATTTGTCTAG	-3	5414	11.64
P2 <sup>1+</sup>	HHHHHHAGSGGC:TCTACTATCTCATC	+1	4952	11.64
D4	HHHHHHAGSRRC:AATGCCATGGATCG*	-12	6100	107.14

**Table 6.1:** Peptide-PNA and Peptide-DNA properties. \*DNA sequence

Prior to immobilization on DNA origami, we characterized the interaction of QD-peptide-PNA constructs to ensure that peptide-PNA conjugation of QDs occurs readily and at desired surface densities. Dynamic light scattering (DLS), agarose gel electrophoresis (AGE), and zeta potential characterization were used to confirm conjugation of the peptide-PNAs to the QD surface. For DLS, QD4 and QD8 were conjugated with P1<sup>3+</sup> or P1<sup>3-</sup> at molar ratios of 10:1 PNA:QD and characterized at 50 nM QD in 25 mM HEPES at pH 7.5. Averaged DLS spectra, provided in Figure



6.2A,B, show that the hydrodynamic diameter of QD4 increased from  $6 \pm 2$  nm to  $11 \pm 3$  nm with conjugation of  $P1^{3+}$  and to  $9 \pm 4$  nm for  $P1^{3-}$ . Similarly, the hydrodynamic diameter of QD8 increased from  $9 \pm 2$  nm to  $17 \pm 5$  nm upon conjugation with  $P1^{3+}$  and to  $11 \pm 3$  nm for  $P1^{3-}$ . The significant difference in the hydrodynamic diameters of QD8: $P1^{3+}$  and QD8: $P1^{3-}$ , in addition to the elongated tail of the number distribution for QD8: $P1^{3+}$ , suggests that conjugation with  $P1^{3+}$  may have induced the formation of small aggregates of QD8, though this speculation was not confirmed by any direct measurements. Zeta potential spectra were obtained for the same sample set characterized by DLS and performed under identical buffer conditions. In all cases, it was found that the QD:peptide-PNAs remained negatively charged at 10:1 PNA:QD; zeta potential values are provided in Table 6.2. Conjugation with  $P1^{3+}$  resulted in a decrease of approximately 40 % in the zeta potential magnitude of both QD4 and QD8, while conjugation with  $P1^{3-}$  increased the zeta potential magnitude of QD8 by approximately 60 % (a similar effect is expected for QD4). For AGE, QD4 and QD8 were conjugated with each peptide-PNA at molar ratios ranging from 1 to 20 and run in a 1 % agarose gel with 1x TBE running buffer (89 mM Tris, 89 mM boric acid, 2 mM EDTA, pH 8.3). For all cases, QD mobility decreased significantly as the molar ratio of PNA:QD increased (Figure 6.2C). The effects of peptide-PNA charge on mobility were less pronounced, though it was observed that the variation in mobility between samples controlled for QD diameter and PNA:QD molar ratio correlated with both the predicted charges of the peptide-PNAs and the zeta potential measurements. In the case of the most positively charged peptide- PNA,  $P1^{3+}$ , both QD4 and QD8 were impeded from leaving the wells at 20:1 PNA:QD. This effect was also observed for

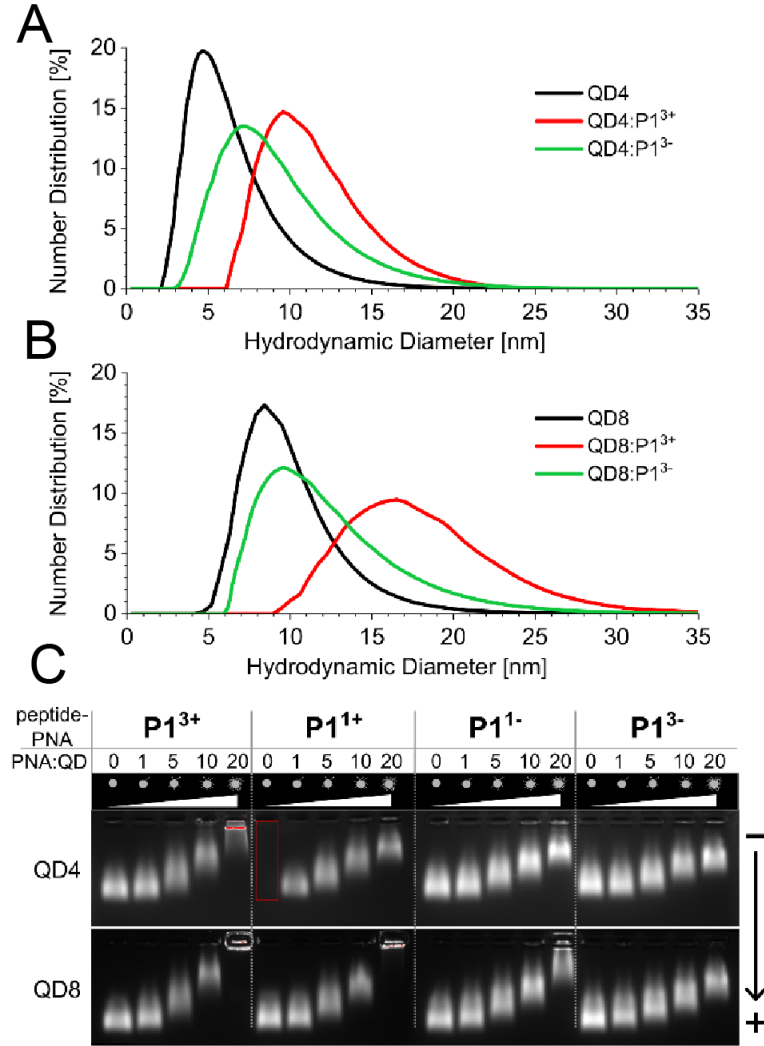


**Figure 6.2:** Effects of conjugation on physical properties of QDs. A) DLS plots of the hydrodynamic diameters of QD4 without any modifications and with peptide-PNAs P1<sup>3+</sup> and P1<sup>3-</sup> at PNA to QD ratios of 10:1. B) DLS plots of the hydrodynamic diameters of QD8 in the same conditions as previous. C) Agarose gel electrophoresis assay of QDs with varying peptide-PNA to QD ratios in 1 % agarose in 1x TBE at pH of 8.3. Each well was loaded with 2 pmole of QD and ran at 8.5 V/cm for 40 minutes prior to imaging. QD mobility was found to decrease significantly as the ratio of peptide-PNA to QD increased, indicating successful conjugation to the QD surface. Peptide-PNA conjugation was observed to impede QDs from leaving the wells at 20:1 for some peptide-PNAs, increasing for more positive peptide-PNAs and larger QDs. One sample was excluded from the gel (red), though this was a redundant sample.

P1<sup>1+</sup> at 20:1 PNA:QD for QD8. In combination, the results of DLS, zeta potential, and AGE suggest that QD conjugation with high molar ratios of positively charged peptide-PNAs may induce aggregation of QDs in solution, and this effect appears to be more pronounced for QD8.

Sample	Hydrodynamic diameter [nm]	Zeta potential [mV]
QD4	6 ± 2	-30 ± 6
QD4:P1 <sup>3+</sup> (1:10)	11 ± 3	-18 ± 3
QD4:P1 <sup>3-</sup> (1:10)	9 ± 4	--
QD8	9 ± 2	-23 ± 5
QD8:P1 <sup>3+</sup> (1:10)	17 ± 5	-13 ± 5
QD8:P1 <sup>3-</sup> (1:10)	11 ± 4	-38 ± 6

**Table 6.2:** DLS and zeta potential of QD:peptide-PNA conjugates.

### 6.2.2 QD-peptide-PNA binding to DNA origami

For immobilization of QDs on to DNA origami, we adapted a twist-corrected form of the 24-helix rectangular DNA origami (Figure 6.3), herein referred to as the DNA breadboard.<sup>166-168</sup> This design was modified such that all staple strands terminate on the same side of the structure, providing a high density of highly-ordered sites from which ssDNA tethers can be extended. For immobilization of QDs on the breadboard, four QD capture sites were chosen in an asymmetric arrangement, each consisting of three 12 nt ssDNA tethers complementary to a specific PNA sequence and three 18 nt tethers complementary to Cy3- or Cy5-labeled ssDNAs (Figure 6.3A). With this design, three Cy3 or Cy5 dyes could be immobilized around the QD tethers, enabling FRET between captured QDs and cyanine dyes for qualitative analysis of QD capture in solution. Though the FRET methodology was used for multiple experiments, it will be expanded upon further when discussing the effect of peptide-PNA charge on QD capture on DNA origami. Both the QD and dye tethers were arranged to minimize the distance of each

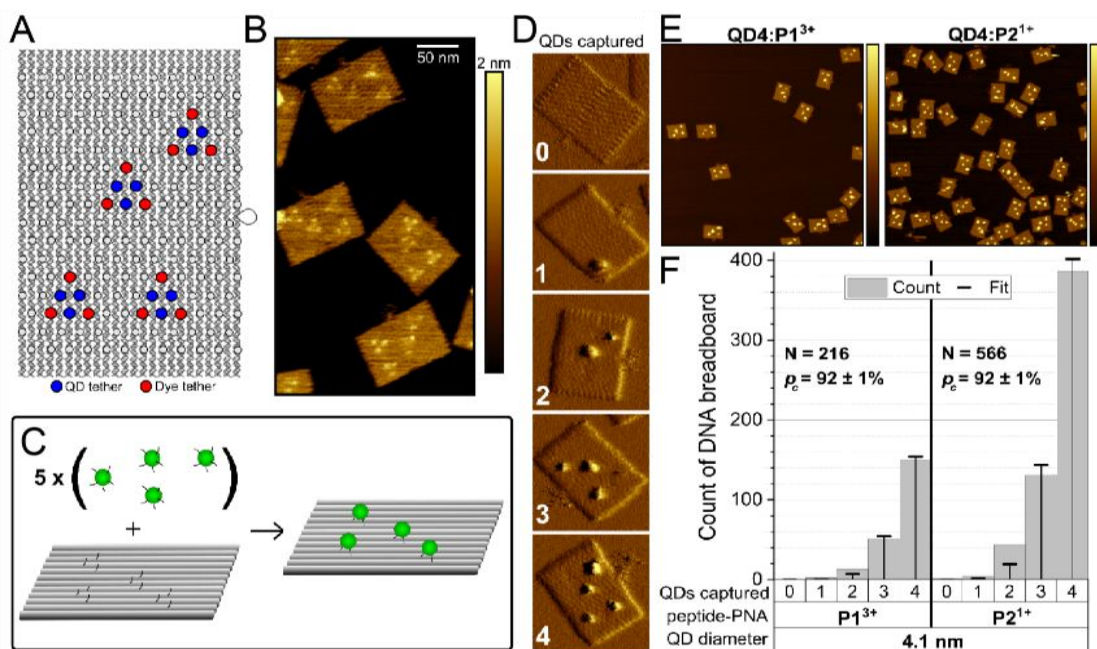


**Figure 6.3:** DNA breadboard design and QD immobilization. A) Molecular model of the DNA breadboard with QD tethers (blue), dye tethers (red), and sites lacking tethers (grey). Individual tether sites are separated by approximately 6 nm from neighboring sites. QD capture sites consist of three QD tethers and are enclosed by three dye tether sites. B) High-resolution AFM topography image of the DNA breadboard, in which dye tethers, hybridized to dye-labeled DNA, could be distinguished at the red locations indicated in A). C) Schematic depicting the immobilization of QDs on DNA breadboards at QD tether sites. Peptide-PNA-conjugated QDs were mixed with DNA breadboards in excess to the number of available capture sites, in this case depicted at a molar ratio of 5:1 QDs to capture sites. D) AFM lock-in amplitude images of DNA breadboards with 0 to 4 QDs captured, indicated in the bottom left of each image. Each image is 125 nm per side. E) AFM topography images (1 by 1  $\mu\text{m}^2$ ) of QD4:P1<sup>3+</sup> (left) and QD4:P2<sup>1+</sup> (right) immobilized on a DNA breadboard with four QD capture sites. QDs and DNA breadboards were mixed at a molar ratio of 5:1 QDs to capture sites and incubated for 12 h at room temperature prior to AFM imaging. AFM height scale bar, 4 nm. F) Counting results and fitted binomial distribution for each sample. The count corresponds to the number of DNA breadboards observed for each of the cases shown in D). Both peptide-PNAs enabled a QD capture efficiency ( $p_c$ ) of  $92 \pm 1\%$  per site for QD4 on the DNA breadboard. Sample size is indicated by N.

tether to the center of the site grouping, with each QD tether located ~3 nm from the center and dye tethers ~6 nm (Figure 6.3A,B). DNA breadboards were assembled from M13mp18 scaffold and 216 unique staple strands<sup>169</sup> in 0.5x TBE and 12.5 mM MgCl<sub>2</sub> at pH 8.3 (TBE/Mg buffer) by annealing from 70 °C to 20 °C over 8 h. After annealing, breadboards were purified from excess staple strands by two rounds of PEG precipitation<sup>170</sup> and rehydrated with TBE/Mg buffer. Cy3- or Cy5-labeled strands were added to samples at 5:1 dye:tethers and annealed at 35 °C for 1 h. Breadboards were then purified from excess dye strands by PEG precipitation and rehydrated with 50 mM HEPES and 9 mM MgCl<sub>2</sub> at pH 7.5. Comparison of the dye fluorescence intensity to standards of varying dye concentrations confirmed that approximately all available dye tethers were bound by dye-labeled strands (data not shown).

Initial experiments were performed with QD4, a quantum dot known to have good solubility and stability in high salt concentrations.<sup>164</sup> QD4 was functionalized with either P1<sup>3+</sup> or P2<sup>1+</sup>, two peptide-PNAs unique in peptide charge and PNA sequence, at a molar ratio of 5:1 PNA: QD. The QD-peptide-PNA conjugates were then mixed with DNA breadboards with 1 or 4 capture sites per structure at a molar ratio of 5:1 QDs to capture sites. QD-breadboards were incubated at room temperature for 12 h prior to characterization with fluorescence spectroscopy and AFM. To quantify the QD capture efficiency for each peptide-PNA and varied capture sites per structure, a minimum of 200 DNA breadboards were manually identified in AFM images and classified by the number of QDs observed per structure; the QD capture efficiencies ( $p_c$ ) were found by fitting the counting results with a binomial distribution. Both QD4:P1<sup>3+</sup> and QD4:P2<sup>1+</sup> were found to have a capture efficiency surpassing 90 % per site for every breadboard

design. For breadboards with a single capture site, QD4:P1<sup>3+</sup> and QD4:P2<sup>1+</sup> had QD capture efficiencies of  $93 \pm 1 \%$  and  $95 \pm 1 \%$ , respectively (Figure 6.4). For breadboards with four capture sites (Figure 6.3), both peptide- PNAs

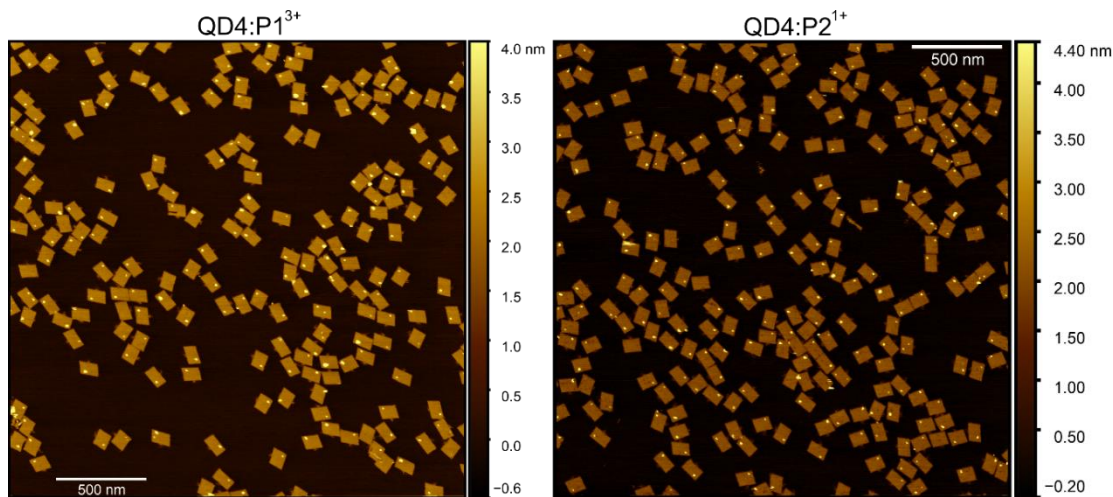


**Figure 6.4:** Capture of a single QD4 on the DNA breadboard. QD4:P1<sup>3+</sup> (left) and QD4:P2<sup>1+</sup> (right) immobilized on the DNA breadboard after mixing at 5:1 QD to capture site. Conjugation with P1<sup>3+</sup> resulted in a capture efficiency of  $93 \pm 1 \%$  (n=1064), and conjugation with P2<sup>1+</sup> resulted in a capture efficiency of  $95 \pm 1 \%$  (n=1115).

resulted in QD capture efficiencies of  $92 \pm 1 \%$  per site. To further quantify the dependence of QD capture on the molar ratio of QDs to capture sites, we mixed QD4:P1<sup>3+</sup> with a DNA breadboard with four capture sites at 1.5:1 and 3:1 QDs to capture sites. The results of AFM counting demonstrated, not surprisingly, that the QD capture efficiency increased for greater excess of QD per site, from  $57 \pm 3 \%$  at 1.5:1, to  $79 \pm 2 \%$  at 3:1, and up to  $92 \pm 1 \%$  at 5:1 (Figure 6.5).

Next, we investigated the effectiveness of peptide-PNA conjugation on QD8, which possesses approximately 4x the surface area of QD4 and was found to be more sensitive to conjugation in the prior experiments. The molar ratios of PNA:QD were limited to

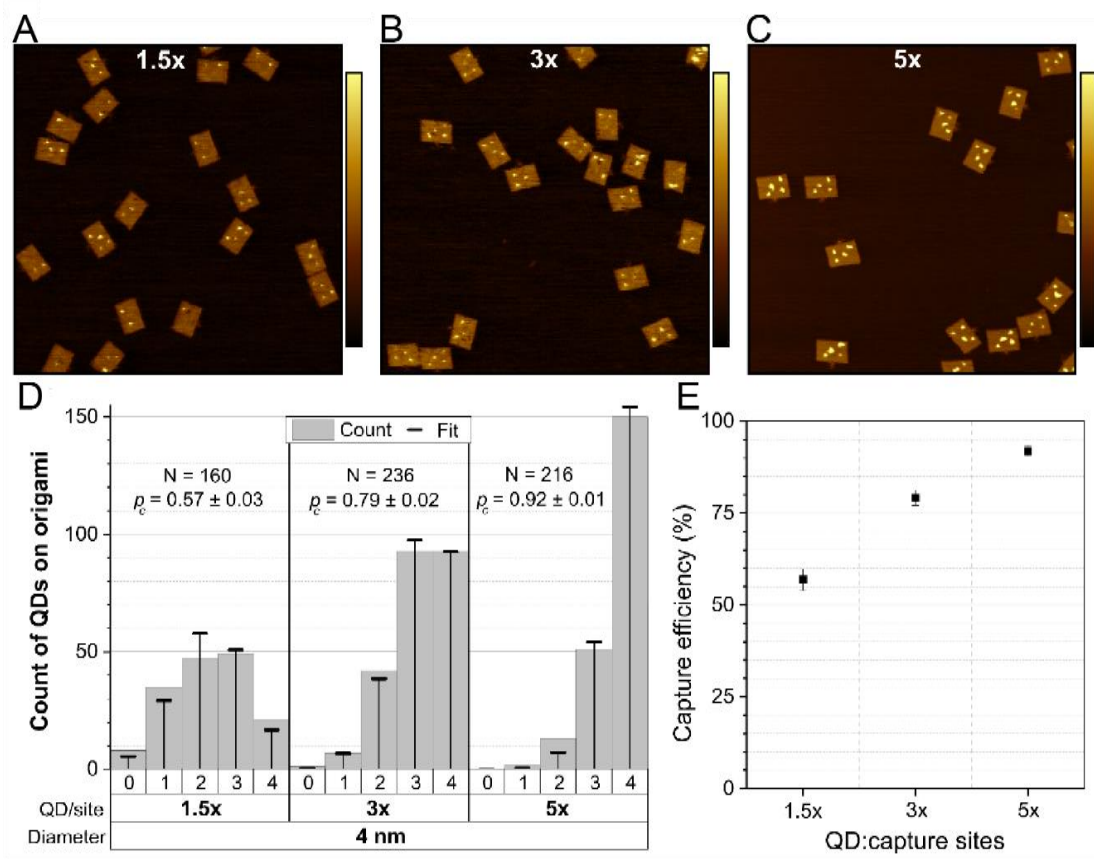


**Figure 6.5:** Effects of QD to capture site ratio on capture efficiency of QD4:P1<sup>3+</sup>. (A-C) Representative AFM topography images (1 x 1  $\mu\text{m}^2$ ) of QD4:P1<sup>3+</sup> immobilized on the DNA breadboard with QD molar excess of (A) 1.5x, (B) 3x, and (C) 5x per capture site. AFM height scale bar, 4 nm. (D) Counting results and fitted binomial distribution for each sample, with sample size (N) of counted structures and probability of QD capture ( $p_c$ ) determined from the binomial fit. (E) Plot of the capture efficiency predicted from AFM counting for 1.5x ( $p_c = 57 \pm 3\%$ , N=160), 3x ( $p_c = 79 \pm 2\%$ , N=236), and 5x ( $p_c = 92 \pm 1\%$ , N=216) QD4:P1<sup>3+</sup> per capture site.

5:1 for all experiments to minimize the effects of peptide-PNA conjugation on QD stability. For an initial test, QD8 was conjugated with either P1<sup>3+</sup> or P2<sup>1+</sup> at 5:1 PNA:QD, then QD-peptide-PNA conjugates were mixed with DNA breadboards with one capture site at 5:1 QDs to capture site and incubated at room temperature overnight.



Contrary to the results observed for QD4, it was found that the capture efficiency of QD8 was strongly dependent on the choice of peptide-PNA; conjugation of QD8 with P1<sup>3+</sup> resulted in a capture efficiency of  $53 \pm 4$  %, while conjugation with P2<sup>1+</sup> resulted in a capture efficiency of  $94 \pm 1$  % (Figure 6.6). While it was expected that QD capture efficiency would be lower for QD8 than QD4 due to a lower surface density of peptide-PNAs, the large variation between peptide-PNAs for QD8 was unexpected given the nearly identical performance of the same peptide-PNAs on QD4. We assumed that the difference in PNA sequence did not contribute significantly to this difference, as issues associated with poor sequence design, such as nonspecific hybridization and secondary structure formation are predictable for short domains and were accounted for in the design of the capture sequences. Rather, we suspected that the difference in peptide sequence had a significant effect on the QD capture efficiency.

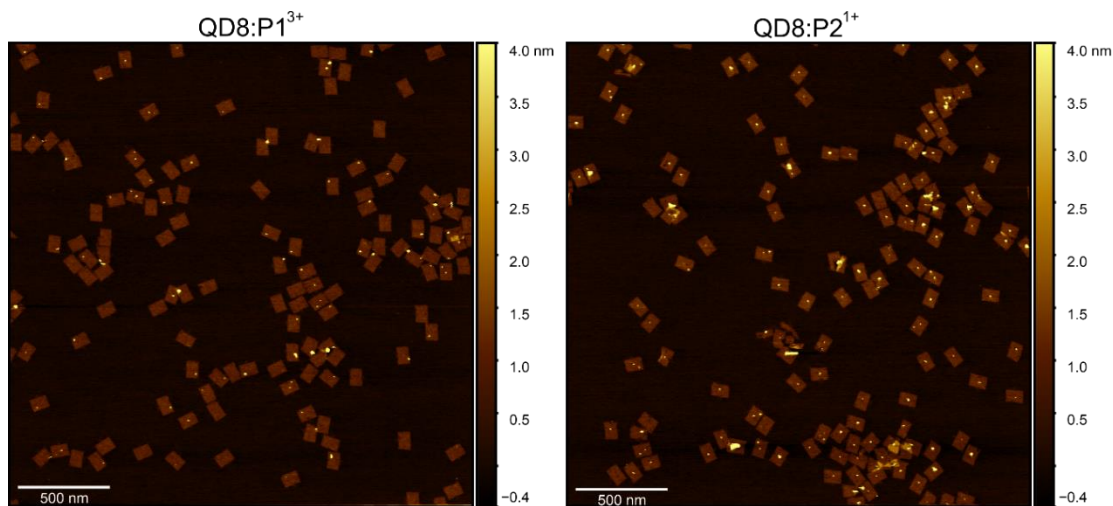


**Figure 6.6:** Capture of a single QD8 on the DNA breadboard. QD8:P1<sup>3+</sup> (left) and QD8:P2<sup>1+</sup> (right) immobilized on the DNA breadboard after mixing at 5:1 QD to capture site. Conjugation with P1<sup>3+</sup> resulted in a capture efficiency of  $53 \pm 4$  % ( $n = 499$ ), and conjugation with P2<sup>1+</sup> resulted in a capture efficiency of  $94 \pm 1$  % ( $n = 296$ ).



To isolate the effects of the peptide on QD capture efficiency, QD8 was conjugated with each of the four peptide-PNAs with identical PNA sequence ( $P1^{3+}$ ,  $P1^{1+}$ ,  $P1^{1-}$ , or  $P1^{3-}$ ) at a ratio of 5:1 peptide-PNAs to QD and mixed with DNA breadboards containing four QD capture sites. In this assay, we reduced the molar ratio of QDs to capture sites down to 1.5:1. At this lower excess of QDs, we expected to observe larger relative variations in the capture efficiency between peptide-PNAs, allowing us to better isolate the effects of the peptides on capture efficiency. Additionally, the lower excess of QDs in solution allowed for a higher signal to noise ratio for FRET determinations. An expanded explanation of the FRET assays is provided in the Materials and methods section. The results of AFM and FRET determinations of QD capture efficiency for each peptide-PNA are provided in Figure 6.7. A distinct trend was observed between peptide net charge and QD capture efficiency in the results of AFM characterization; the QD capture efficiency increased for more negatively charged peptide-PNAs, from  $20 \pm 1$  % for  $P1^{3+}$ ,  $31 \pm 2$  % for  $P1^{1+}$ ,  $41 \pm 3$  % for  $P1^{1-}$ , up to  $48 \pm 3$  % for  $P1^{3-}$ . This trend was not observed in the FRET-determined capture efficiencies, though these values possessed significantly greater uncertainty than AFM-determined values due to variations in fluorescence intensity between identical control samples. Additionally, the average donor-acceptor distances may vary between peptides due to interactions with the negatively charged CL4 ligands, and this is not accounted for in the FRET determinations of capture efficiency. Notably, while the effects of peptide charge on capture efficiency were apparent for QD8 as determined by AFM, the peptide charge did not seem to have a significant effect on QD4; the worst performing peptide-PNA on QD8,  $P1^{3+}$ , still enabled  $57 \pm 3$  % capture efficiency for

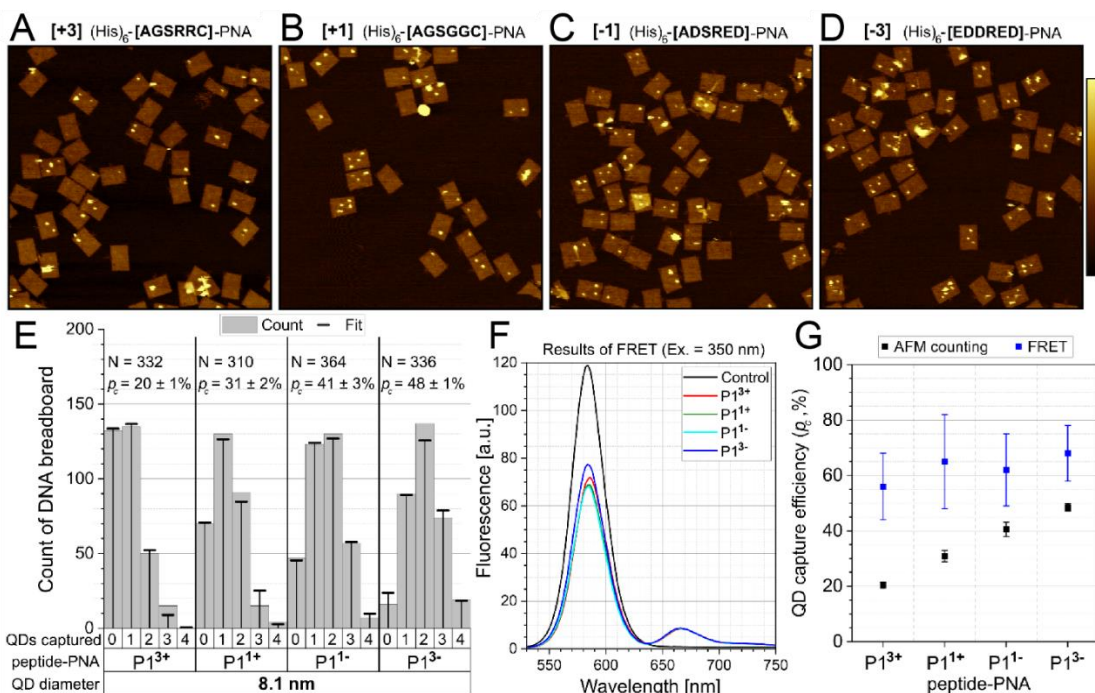


**Figure 6.7:** Effects of peptide charge on capture efficiency of QD8. (A-D) Representative AFM topography images ( $1 \times 1 \mu\text{m}^2$ ) of (a) QD8:P1<sup>3+</sup>, (b) QD8:P1<sup>1+</sup>, (c) QD8:P1<sup>1-</sup>, and (d) QD8:P1<sup>3-</sup> on a DNA breadboard with four capture sites, mixed at a ratio of 1.5x QDs to capture sites to amplify the effects of peptide charge on capture efficiency. The interior 6-residue peptide domain, varying between peptide-PNAs of different net charge, is provided above each image along with the associated net charge at pH 7.5. The PNA sequence did not vary between samples. AFM height scale bar, 5 nm. E) Counting results and fitted binomial distribution for each sample, with sample size (N) of counted structures and probability of QD capture ( $p_c$ ) determined from the binomial fit. F) Plot of the fluorescence spectra for each QD-breadboard sample, demonstrating FRET between QD8 and Cy5 upon excitation at 350 nm. The control sample was generated by passivating QDs with complementary ssDNA at 100x excess prior to mixing with the DNA breadboard. QD quenching and sensitized emission was observed for each sample, confirming precise immobilization of QDs and Cy5 on the DNA breadboard. (g) Plot of QD capture efficiencies for each sample as determined by AFM counting (black) and FRET (blue).

QD4 at the same molar ratio. We speculated that this was due to several factors favoring the smaller diameter of QD4, namely higher surface density of peptide-PNA, improved

presentation of PNA due to greater surface curvature,<sup>171-172</sup> and greater colloidal stability than QD8, increasing the accessibility even if the positively charged peptide has a negative impact on PNA orientation with respect to the QD surface. Much like any NP-biological conjugate, the size and stability of the NP plays a large role in functionality of the attached biological material, and here we have shown that by increasing the negative charge of the peptide, the capture efficiency of QD8 can be increased without increasing the peptide-PNA to QD or QD to breadboard ratios.

For a comparison to peptide-DNA conjugation, we replaced the peptide-PNAs with peptide-DNAs, commercially synthesized (Bio-Synthesis Inc.) at about 10 times the cost of peptide-PNAs. The peptide-DNAs were added to QD4 and QD8 at a ratio of 5 peptide-DNAs to QD using the same protocol as peptide-PNAs. QD4:D4 and QD8:D4 were then added to a DNA-breadboard at 5:1 and 1.5:1 QD per capture site, respectively. Both samples were characterized by AFM, and the QD8-breadboard constructs were additionally characterized with fluorescence spectroscopy for FRET analysis. Peptide-DNAs resulted in a lower capture efficiency for QD4 than peptide-PNAs in identical conditions,  $81 \pm 2 \%$  vs  $92 \pm 1 \%$  at 5:1 QD4 to capture sites (Figure 6.8). Interestingly, the case was reversed for QD8 - peptide-DNAs resulted in a capture efficiency of  $55 \pm 3 \%$  at 1.5:1 QD8 to capture sites, slightly higher than the best performing peptide-PNA, P1<sup>3-</sup>, at  $48 \pm 3 \%$ . The FRET-determined capture efficiency showed a similar trend and was approximately equivalent to the best performing peptide-PNA for QD8 when accounting for the additional length of the linker. Overall, the performance of peptide-DNA was comparable to the best performing peptide-PNA.

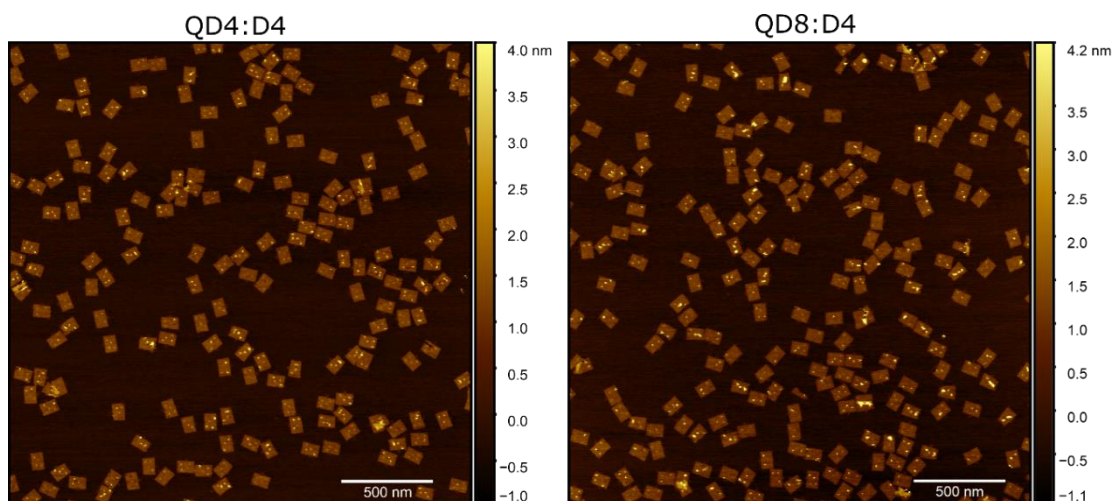


**Figure 6.8:** Peptide-DNA immobilization of QDs on a DNA breadboard with four capture sites. QD4:D4 mixed at 5:1 QDs to capture sites (left) and QD8:D4 mixed at 1.5:1 QDs to capture sites (right) on the DNA. QD4:D4 at 5:1 had a capture efficiency of  $81 \pm 2 \%$  ( $n=340$ ), and QD8:D4 at 1.5:1 had a capture efficiency of  $55 \pm 3 \%$  ( $n=325$ ).

As a final experiment, we synthesized DNA breadboards to capture QD4 and QD8 at separate locations in a one pot mixture (Figure 6.9A). QD4 and QD8 were conjugated with  $P2^{1+}$  and  $P1^{3-}$ , respectively, at 5:1 peptide-PNA to QD, then both QDs were mixed with the DNA breadboard at a molar ratio of 5:1 QDs to capture sites. Samples were incubated overnight at room temperature and characterized by AFM and TEM. AFM topography height profiles of QDs on a DNA breadboard are provided in Figure 6.9B, and the difference in height profiles for QD4 and QD8 provides evidence that immobilization of each QD occurred at the intended locations. As with DNA, the use of orthogonal PNA sequences on different QDs enabled site-selective immobilization of each QD to capture sites with complementary DNA tethers. While common challenges associated with colloidal QDs still persist, overall these results demonstrate

that peptide-PNAs provide a precise and efficient means of QD conjugation and immobilization on DNA nanostructures.

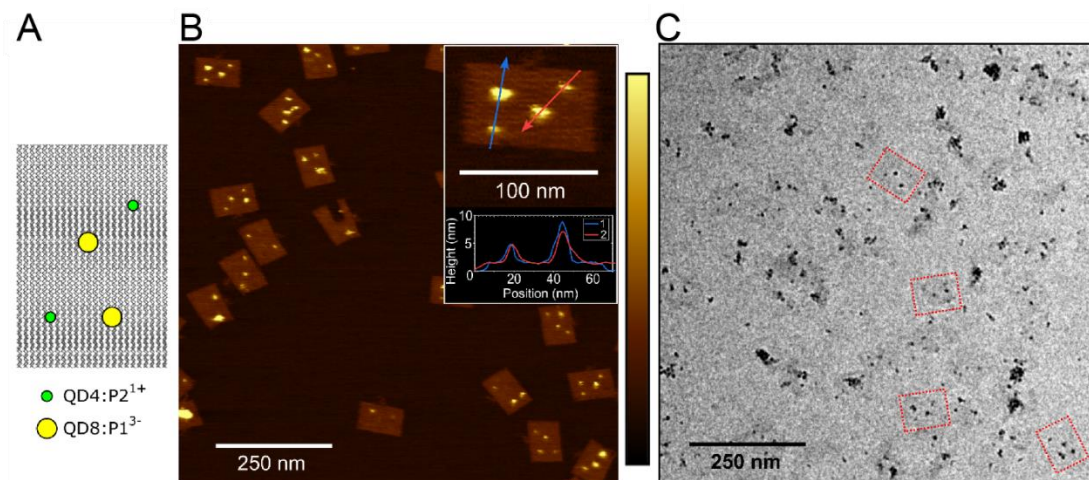


**Figure 6.9:** Selective immobilization of QD4 and QD8 on the DNA breadboard. A) Schematic depicting the intended positions of QD4 and QD8 on the DNA breadboard. QD4 was conjugated with P2<sup>1+</sup> and QD8 with P1<sup>3-</sup>, which have orthogonal PNA sequences to prevent nonspecific immobilization of QDs at capture sites. B) AFM topography image of the QD-breadboard constructs corresponding to A). A magnified image of a QD-breadboard demonstrating successful immobilization of all QDs is shown in the inset, along with topography profiles that show the difference in size of neighboring QD4 and QD8. C) TEM image of the QD-breadboard constructs corresponding to A). Several structures are outlined in red to aid visualization. Unlike with mica, excess QDs were not successfully removed from the surface by rinsing, and samples were dried prior to imaging. This resulted in the observed non-specific clustering of QDs.

### 6.3 Conclusions

We have shown that peptide-PNAs provide a simple method to conjugate QDs for site-selective immobilization on DNA nanostructures, enabling greater than 90 % capture efficiency through PNA-DNA hybridization with as little as 5:1 molar excess of QDs to binding sites. This method further enabled highly precise immobilization of

QDs, to within a few nanometers of the location, as indicated by the FRET measurements. Additionally, the high attachment efficiencies demonstrated here have been achieved with a low peptide-PNA surface density, making this an ideal strategy for immobilization of QDs functionalized with other biological materials such as enzymes for enhanced catalysis<sup>173</sup> or dye-labeled peptides for FRET-based biosensing.<sup>174-175</sup> The success of this strategy may allow for additional properties that can be incorporated through PNA conjugations such as improved rigidity, resistance to enzyme degradation and protection from higher temperatures.<sup>142, 145, 176-177</sup> Furthermore, though we have focused on QDs as an example, we hypothesize that other NPs, such as noble metal or carbon based NPs, may also be efficiently conjugated using peptide-PNAs.

## **6.4 Materials and methods**

### *6.4.1 QD conjugation with peptide-PNAs*

Prior to use, colloidal CL4-capped QDs were mixed by ultrasonic agitation for 15 min to ensure full dissolution of QDs, and peptide-PNAs in water were heated at 45°C for 15 min. To conjugate QDs with peptide-PNAs, peptide-PNAs were diluted in buffer, then the QDs were added to the peptide-PNA and buffer solution, vortexed briefly, and allowed to conjugate at room temperature for 1 hour prior to use. Peptide-PNA-conjugated QD solutions were prepared with a final QD concentration of 1.5  $\mu\text{M}$  in 50 mM HEPES at pH 7.5, and peptide-PNA concentrations varied from 1.5  $\mu\text{M}$  to 30  $\mu\text{M}$  depending on the desired peptide-PNA:QD molar ratio. For experiments on QD capture by DNA breadboards, peptide-PNA:QD molar ratios were maintained at 5:1.

#### *6.4.2 DLS and zeta potential characterization*

Dynamic Light Scattering and zeta potential were obtained on a Malvern Zetisizer Ultra of a 50 nM QD concentration with 10 peptide-PNA per QD, either P1<sup>3+</sup> or P1<sup>3-</sup>, in 25 mM HEPES. Prior to measurement, the samples were filtered using a 0.2 µm syringe filter. Reported results are averages of minimum three experiments which each contained 10 runs.

#### *6.4.3 DNA breadboard synthesis*

DNA breadboards were prepared in 0.5x TBE (Tris-borate EDTA) with 12.5 mM MgCl<sub>2</sub>. M13mp18 scaffold was added for a final concentration of 20 nM, and unmodified staple strands were added at 100 nM per strand. Staple strands modified at the 3' end with QD and dye capture sites were added at 200 nM per strand. To assemble the DNA breadboard, the scaffold and staple solution was thermally annealed at 70°C for 15 minutes, then cooled at a rate of 0.1°C/min to 20°C and rapidly cooled to 10°C. The design consisted of 216 staple strands in total, of which 192 were common to every design.<sup>169</sup> For QD and dye capture sites, 24 strands were modified at the 3' end with either two unique sequences complementary to P1 or P2, or with two unique sequences complementary to the Cy3-labeled strand or Cy5-labeled strand.

#### *6.4.4 PEG precipitation of DNA breadboard*

After thermal annealing of the DNA breadboard, origami were separated from excess staple strands by PEG precipitation using the following protocol adapted from Stahl et al.<sup>178</sup>

1. Add an equal volume of 15 % w/v PEG-8000, 5 mM Tris, 1 mM EDTA, 12.5 mM MgCl<sub>2</sub>, and 505 mM NaCl to the DNA breadboard solutions, and agitate lightly to mix.
2. Centrifuge samples at 16,000 rcf for 25 min with samples maintained at room temperature.
3. Carefully extract the supernatant with a pipette to avoid disturbing the precipitated DNA.
4. Rehydrate the precipitated DNA with a volume of 0.5x TBE and 12.5 mM MgCl<sub>2</sub> equal to the volume of PEG solution added in step 1.
5. Agitate solution lightly for 5 minutes.
6. Repeat steps 1-4.
7. Anneal DNA breadboard solution for 1 hr at 30°C to aid dissolution of the precipitated DNA.
8. Allow samples to cool to room temperature, then measure the DNA breadboard concentration with UV absorbance at 260 nm ( $\epsilon \approx 1.11 \times 10^8 \text{ M}^{-1} \text{ cm}^{-1}$ ).

#### *6.4.5 Dye immobilization on DNA breadboard*

Cy3- or Cy5-labeled ssDNAs (100  $\mu\text{M}$  in 1x Tris-EDTA) were added to the PEG-filtered DNA breadboard solution at 5:1 molar ratio to dye tether sites. Cy3-labeled strands were added to structures for FRET with QD4 and Cy5 for QD8. The samples were annealed for 1 hr at 35°C and allowed to cool to room temperature for 15 minutes, then one round of PEG precipitation (steps 1-3, see above) was performed on each



sample. Successful immobilization of dyes on the DNA breadboard was indicated by a brightly colored pellet – this was not observed for samples with mismatched dye-ssDNA/tethers. The precipitant was rehydrated with the desired buffer (50 mM HEPES with 9 mM MgCl<sub>2</sub>) to a final DNA breadboard concentration of 40 nM (assuming 100 % recovery from PEG precipitation). Samples were agitated lightly and stored at room temperature for up to 72 hrs. Prior to use in experiments, DNA breadboard concentrations were determined from UV absorbance at 260 nm on a Nanodrop One system.

#### *6.4.6 QD immobilization on DNA breadboard*

To immobilize peptide-PNA-conjugated QDs on the DNA breadboard, QD-peptide-PNAs were added to a diluted DNA breadboard solution for a resulting solution of 10 nM breadboard in 50 mM HEPES and 9 mM MgCl<sub>2</sub> at pH 7.5, with QD concentrations between 50 nM and 200 nM depending on the number of capture sites present on the breadboard and the desired excess of QDs per capture site. QD-breadboard solutions were then mixed lightly and stored in darkness at room temperature for 12 hours prior to fluorescence and AFM characterization.

#### *6.4.7 QD FRET determination of QD capture on DNA breadboard*

The DNA breadboard was designed with triangular QD and dye tether sections as seen in Figure 6.3A. These tethers are independent of the target QD and of the FRET acceptor dye introduced into the DNA origami. For QD4 a Cy3 dye was utilized as a FRET acceptor and for QD8 a Cy5 dye. Spatial distributions can be estimated from these positions that take into account the length of the tethers. As our measurements

were realized on the ensemble population we assumed that the heterogeneity of capture position would average out, we therefore consider the QD as centrally localized within the triangular capture spot and that the FRET acceptors are equidistant and equivalent acceptors. When considering FRET donor-acceptor distances ( $r_{DA}$ ) for QDs, it is assumed that the point-dipole of QDs is positioned at the center of the QD. Therefore the varying diameters of QD4 and QD8 will result in slightly different distance distributions.

The FRET efficiency,  $E$ , experiments were undertaken by comparing the QD quench (Equation S1a) as well as the sensitized emission (Equation 6.1) of a sample with captured QDs to a similar sample that had excess single stranded DNA added that blocked the PNA on the QD surface.

$$E^{exp} = 1 - \frac{I_{DA}^{QD}}{I_D^{QD}} = \frac{(I_{DA}^{dye} - I_A^{dye})/QY^{dye}}{I_D^{QD}/QY^{QD}} \quad (\text{Eq. 6.1})$$

Where  $I$  is the integrated intensity of either the QD or the dye in the presence of the Donor-acceptor (DA), just acceptor (A), or just donor (D), and QY is the fluorescence QY of either the QD or dye.

Upon the experimental determination of  $E^{exp}$ , the values were corrected by the excess QD in solution that could not bind to any DNA origami as well as change in stability with varying charged peptides. This was done by dividing the  $E^{exp}$  by the inverse of the QD/capture site ratio.

Our intent was to determine the binding efficiency of QDs to DNA origami in solution,  $p_c$ . In Eq. 6.2 we show the comparison of  $E^{\text{exp}}$  to the  $E^{\text{theory}}$  which is defined in Eq. 6.2 and 6.3.

$$E^{\text{exp}} = p_c * E^{\text{theory}} \quad (\text{Eq. 6.2})$$

$$E^{\text{theory}} = \frac{N\left(\frac{R_0}{r_{\text{DA}}}\right)^6}{1+N\left(\frac{R_0}{r_{\text{DA}}}\right)^6} \quad (\text{Eq. 6.3})$$

Where  $N$  is the number of acceptors,  $N = 3$  in this case and  $r_{\text{DA}}$  and  $R_0$  are the values determined above for each QD-dye pair.

An example is presented of the calculation for P1<sup>-3</sup> reported in Figure 6.7. The  $r_{\text{DA}}$  was 7.2 nm, while  $R_0$  was 6.2 nm as detailed above, this results in a  $E^{\text{theory}} = 0.55$ . The graphically determined FRET efficiency using Eq. 6.1, was  $0.25 \pm 0.04$ , correcting for excess QD the resulting  $E^{\text{exp}} = 0.38 \pm 0.05$ . The  $p$  value reported in percentage was therefore 68 % with an upper and lower bound of 78 and 59, respectively.

#### 6.4.8 AFM characterization and counting

AFM characterization was performed in fluid on a JPK Instruments (Germany) fast-scan AFM. Samples were diluted to 1 nM QD-breadboards in 0.2  $\mu\text{M}$ -filtered 0.5x TBE and 8 mM  $\text{MgCl}_2$ . 15  $\mu\text{L}$  of diluted sample was deposited onto freshly cleaved mica and incubated for 5 minutes. 100  $\mu\text{L}$  of filtered buffer was added to the mica, then wicked off the surface with an optics wipe. This was repeated once more, then the sample was transferred to the AFM and 100  $\mu\text{L}$  of filtered buffer was added to the mica. Images of  $2.5 \times 2.5 \mu\text{m}^2$  were captured at a scan rate of 6 Hz and 2000 pts/line.

#### *6.4.9 TEM characterization*

For characterization by TEM, samples were prepared on Ted Pella 01822-F ultrathin carbon, Formvar-backed grids. Grids were precleaned in a PDC-32G Harrick Plasma (Ithaca, NY) by plasma treatment in 300 mTorr of air for 45 seconds. Samples were diluted to 1 nM QD-breadboards in 0.2  $\mu$ M-filtered 0.5x TBE and 8 mM MgCl<sub>2</sub>. 5  $\mu$ L of diluted sample was deposited onto a freshly cleaned TEM grid and incubated for 5 minutes. The sample was wicked off the surface with an optics wipe, then 5  $\mu$ L of water was deposited onto the grid and immediately wicked off. The sample grid was then stored until imaging on a JEOL JEM-2100 LaB6 TEM at 200 keV.

## Chapter 7: Conclusions

This dissertation has focused on expanding our understanding of how biological activity can be thermally controlled through fs laser pulse excitation of AuNPs. We utilized a 55 nm diameter AuNP for our primary heat source and biological scaffold, as AuNPs are efficient light to heat converters and can be readily conjugated to a wide array of biological materials. The use of a spherical AuNP allowed for us to thoroughly examine the theoretical temperature profiles and better assess our experimental results. We designed the AuNP laser system so that: 1) the local temperature around the AuNP would fall in the biological relevant range 5-100 °C, 2) the AuNP would return to baseline temperature before another pulse arrives, and 3) the temperature increase was confined to less than 20 nm from the AuNP surface. As a consequence, the temperature increases only lasted for ~5 ns and a sharp thermal gradient extended from the AuNP surface. We have examined two prototypical biological materials (DNA and enzymes) in these dynamic temperature profiles in order to achieve the following goals: 1) probe the kinetic responses during heating, 2) access the level of precision and control afforded over biological activity, and 3) understand the relationship between the heating profile and the biological response.

In Chapter 3, we examined the dsDNA denaturation rate with different melting temperatures scaffolded on the AuNP surface. We observed an inverse relationship between the denaturation rate and melting temperatures, indicating that the different dsDNAs could be used as a quantitative local nanothermometer. Furthermore, we report that the rate of dsDNA denaturation can be modulated by controlling the laser pulse radiant exposure, and the bulk solution temperature, providing additional control

over DNA release. By controlling the DNA melting temperature, pulse radiant exposure, and bulk solution temperature, we displayed a high level of control over the DNA denaturation rate and demonstrated that the rate could be varied by more than threefold. To better correlate the observed DNA denaturation rates to the theoretical temperature profiles, we present a modified DNA dissociation equation that allowed us to extract a “sensed” temperature parameter. Comparing the sensed temperature with the theoretical temperatures, we hypothesized that the steep temperature gradient near the AuNP surface plays a significant role in the DNA denaturation.

In Chapter 4 we sought to investigate the effect of the steep temperature gradient on DNA denaturation. To do so, we designed a similar dsDNA-AuNP system that allowed us to vary the distance between the dsDNA and AuNP surface by 3.8 nm in total, using intervals of  $\sim 1.1$  nm. We found that the rate of denaturation is increased when the DNA is closer to the AuNP surface and that the rate can be modified by up to  $30 \pm 2$  % through shifting the DNA location by as little as 1.1 nm. Using the modified DNA dissociation equation from Chapter 3, we obtained the sensed temperatures from the DNA release rates and examined them in the context of the theoretical temperature profiles. In doing so, we found that the peak or maximum temperatures near the AuNP surface cause the DNA to release at a rate higher than what is theoretically predicted. To provide further insight on the DNA melting dynamics, we collaborated with Dr. Parth Chaturvedi and Prof. Lela Vuković from the University of Texas El Paso. They performed molecular dynamics (MD) simulations of DNA melting on a gold surface from a ns heat pulse, mimicking the fs laser pulse optical heating in our system. From their MD simulations and our experimental findings we report that DNA

dehybridization in our system likely occurs through a stochastic single-pulse dual-end unzipping mechanism. Additionally, the MD simulations showed that the increased release rate near the AuNP surface was due to increased proximal bp separation, confirming our experimental findings.

In Chapter 5, we investigated the possibility of enzyme enchantment through fs laser pulse excitation of AuNPs. While we were unable to demonstrate enzymatic enhancement, our work has allowed us to identify the key variables that dictate these systems. Furthermore, we derived an equation describing the theoretical % increase in product formation during laser pulse heating. The % increase in product formation is dependent on the laser repetition rate, the single pulse heating duration, and the ratio of  $V_H$  to  $V_c$ . It is also evident from our analysis that laser systems should be operated at repetition rates of 100 kHz or higher if a significant enhancement in enzyme production is desired. We also propose that thermophilic enzymes are a prime candidate for this technique as they can achieve  $V_H$  to  $V_c$  ratios of up to 2000 over a biologically relevant temperature range.

In Chapters 6, due to equipment limitations and COVID19 restrictions, we pivot from confined photothermal heating and investigate the potential of peptide-PNA hybrids as a novel strategy for NP conjugation to DNA nanostructures. Using QDs as a model NP material, we were able to demonstrate over 90% capture efficiency on a DNA breadboard with as little as 5 peptide-PNAs per QD. These results indicate that peptide-PNA hybrids could be used to attach other NPs such as AuNPs to DNA nanostructures. As PNA-DNA and PNA-PNA duplexes have increased thermal stability, one could envision peptide-PNAs being used to precisely place “nanoheaters”


on a DNA structure, allowing for the heating of other materials without denaturing the duplex.






While the work performed here provides a fundamental understanding of how fs laser pulse excitation of AuNPs can be used to modulate biological activity, the vast parameter space innate to these systems leaves much to be explored. We have identified a few key questions that still remain unanswered and as such will be the focus of future work. One of the most critical parameters in these systems is the single pulse heating duration in the NP local environment. For the work performed here, this time is fixed to ~5 ns. From our calculations in Chapter 5, we found that increasing this time to ~20 ns could provide up to a 4-fold enhancement in enzyme activity. This heating duration could be tuned by encapsulating the NPs in a biopolymer, through ligand choice or even changing the NP composition. Systems such as the dsDNA-AuNP “nanothermometer” discussed in Chapters 3 and 4 could be used to probe changes in the heating duration. Additionally, we are interested in testing if high repetition rate laser systems (>100 kHz) can be used to successfully enhance the activity of thermophilic enzymes. If thermophilic enzymes can be locally heated, their fast catalytic rates could be assessed and they could potentially be implemented into multienzyme cascades with mesophilic enzymes. Finally, we look to investigate the denaturation of PNA duplexes during confined photothermal heating. If PNA duplexes are able to withstand moderate pulse radiant exposures, they could be used to precisely position AuNP nanoheaters on a DNA nanostructure, allowing for thermally induced local actuation of the nanostructure while the AuNP stays bound to the desired location.




# Permissions

Figure 1.1A



 Home  Help  Live Chat  Sign in  Create Account



ACS Publications  
More Trusted. More Clear. More Trust.

**Size and Temperature Dependence of the Plasmon Absorption of Colloidal Gold Nanoparticles**  
Author: Stephan Link, Mostafa A. El-Sayed  
Publication: The Journal of Physical Chemistry B  
Publisher: American Chemical Society  
Date: May 1, 1999  
Copyright © 1999, American Chemical Society

**PERMISSION/LICENSE IS GRANTED FOR YOUR ORDER AT NO CHARGE**


This type of permission/license, instead of the standard Terms and Conditions, is sent to you because no fee is being charged for your order. Please note the following:

- Permission is granted for your request in both print and electronic formats, and translations.
- If figures and/or tables were requested, they may be adapted or used in part.
- Please print this page for your records and send a copy of it to your publisher/graduate school.
- Appropriate credit for the requested material should be given as follows: "Reprinted (adapted) with permission from (COMPLETE REFERENCE CITATION). Copyright (YEAR) American Chemical Society." Insert appropriate information in place of the capitalized words.
- One-time permission is granted only for the use specified in your RightsLink request. No additional uses are granted (such as derivative works or other editions). For any uses, please submit a new request.

If credit is given to another source for the material you requested from RightsLink, permission must be obtained from that source.

[BACK](#)[CLOSE WINDOW](#)

Figure 1.1B

ACS Publications  
And You're Most Cited Most Read

**Nanoparticle Size Influences Localized Enzymatic Enhancement—A Case Study with Phosphotriesterase**

Author: Joyce C. Breger, Eunkeu Oh, Kimihiro Susumu, et al  
Publication: Bioconjugate Chemistry  
Publisher: American Chemical Society  
Date: Jul 1, 2019  
Copyright © 2019, American Chemical Society

**PERMISSION/LICENSE IS GRANTED FOR YOUR ORDER AT NO CHARGE**


This type of permission/license, instead of the standard Terms and Conditions, is sent to you because no fee is being charged for your order. Please note the following:


- Permission is granted for your request in both print and electronic formats, and translations.
- If figures and/or tables were requested, they may be adapted or used in part.
- Please print this page for your records and send a copy of it to your publisher/graduate school.
- Appropriate credit for the requested material should be given as follows: "Reprinted (adapted) with permission from (COMPLETE REFERENCE CITATION). Copyright (YEAR) American Chemical Society." Insert appropriate information in place of the capitalized words.
- One-time permission is granted only for the use specified in your RightsLink request. No additional uses are granted (such as derivative works or other editions). For any uses, please submit a new request.


If credit is given to another source for the material you requested from RightsLink, permission must be obtained from that source.


[BACK](#)[CLOSE WINDOW](#)


Figure 1.2





 Home

 Help ▾

 Live Chat

 Sign in

 Create Account



ACS Publications  
Most Trusted. Most Cited. Most Read.

**Optical Studies of Dynamics in Noble Metal Nanostructures**  
Author: Gregory V. Hartland  
Publication: Chemical Reviews  
Publisher: American Chemical Society  
Date: Jun 1, 2011  
Copyright © 2011, American Chemical Society

**PERMISSION/LICENSE IS GRANTED FOR YOUR ORDER AT NO CHARGE**

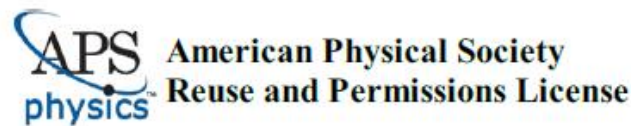
This type of permission/license, instead of the standard Terms and Conditions, is sent to you because no fee is being charged for your order. Please note the following:

- Permission is granted for your request in both print and electronic formats, and translations.
- If figures and/or tables were requested, they may be adapted or used in part.
- Please print this page for your records and send a copy of it to your publisher/graduate school.
- Appropriate credit for the requested material should be given as follows: "Reprinted (adapted) with permission from (COMPLETE REFERENCE CITATION). Copyright (YEAR) American Chemical Society." Insert appropriate information in place of the capitalized words.
- One-time permission is granted only for the use specified in your RightsLink request. No additional uses are granted (such as derivative works or other editions). For any uses, please submit a new request.

If credit is given to another source for the material you requested from RightsLink, permission must be obtained from that source.

[BACK](#)[CLOSE WINDOW](#)

Figure 1.3



09-Nov-2021

This license agreement between the American Physical Society ("APS") and David Hastman ("You") consists of your license details and the terms and conditions provided by the American Physical Society and SciPris.

#### Licensed Content Information

License Number:	RNP/21/NOV/046493
License date:	09-Nov-2021
DOI:	10.1103/PhysRevB.84.035415
Title:	Femtosecond-pulsed optical heating of gold nanoparticles
Author:	Guillaume Baffou and Hervé Rigneault
Publication:	Physical Review B
Publisher:	American Physical Society
Cost:	USD \$ 0.00

#### Request Details

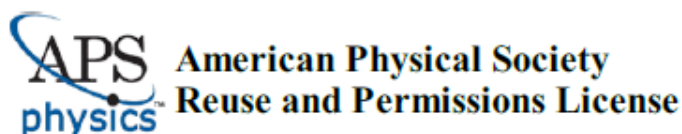
Does your reuse require significant modifications:	No
Specify intended distribution locations:	Worldwide
Reuse Category:	Reuse in a thesis/dissertation
Requestor Type:	Student
Items for Reuse:	Figures/Tables
Number of Figure/Tables:	2
Figure/Tables Details:	Figure 2 and Figure 4
Format for Reuse:	Print and Electronic
Total number of print copies:	Up to 1000

#### Information about New Publication:

University/Publisher:	University of Maryland
Title of dissertation/thesis:	CONFINED PHOTOTHERMAL HEATING OF NANOPARTICLE DISPLAYED BIOMATERIALS
Author(s):	David Hastman
Expected completion date:	Dec. 2021

#### License Requestor Information

Name:	David Hastman
Affiliation:	Individual
Email Id:	dhastman@terpmail.umd.edu
Country:	United States





## TERMS AND CONDITIONS


The American Physical Society (APS) is pleased to grant the Requestor of this license a non-exclusive, non-transferable permission, limited to Print and Electronic format, provided all criteria outlined below are followed.


1. You must also obtain permission from at least one of the lead authors for each separate work, if you haven't done so already. The author's name and affiliation can be found on the first page of the published Article.
2. For electronic format permissions, Requestor agrees to provide a hyperlink from the reprinted APS material using the source material's DOI on the web page where the work appears. The hyperlink should use the standard DOI resolution URL, <http://dx.doi.org/{DOI}>. The hyperlink may be embedded in the copyright credit line.
3. For print format permissions, Requestor agrees to print the required copyright credit line on the first page where the material appears: "Reprinted (abstract/excerpt/figure) with permission from [(FULL REFERENCE CITATION) as follows: Author's Names, APS Journal Title, Volume Number, Page Number and Year of Publication.] Copyright (YEAR) by the American Physical Society."
4. Permission granted in this license is for a one-time use and does not include permission for any future editions, updates, databases, formats or other matters. Permission must be sought for any additional use.
5. Use of the material does not and must not imply any endorsement by APS.
6. APS does not imply, purport or intend to grant permission to reuse materials to which it does not hold copyright. It is the requestor's sole responsibility to ensure the licensed material is original to APS and does not contain the copyright of another entity, and that the copyright notice of the figure, photograph, cover or table does not indicate it was reprinted by APS with permission from another source.
7. The permission granted herein is personal to the Requestor for the use specified and is not transferable or assignable without express written permission of APS. This license may not be amended except in writing by APS.
8. You may not alter, edit or modify the material in any manner.
9. You may translate the materials only when translation rights have been granted.
10. APS is not responsible for any errors or omissions due to translation.
11. You may not use the material for promotional, sales, advertising or marketing purposes.
12. The foregoing license shall not take effect unless and until APS or its agent, Aptara, receives payment in full in accordance with Aptara Billing and Payment Terms and Conditions, which are incorporated herein by reference.
13. Should the terms of this license be violated at any time, APS or Aptara may revoke the license with no refund to you and seek relief to the fullest extent of the laws of the USA. Official written notice will be made using the contact information provided with the permission request. Failure to receive such notice will not nullify revocation of the permission.
14. APS reserves all rights not specifically granted herein.
15. This document, including the Aptara Billing and Payment Terms and Conditions, shall be the entire agreement between the parties relating to the subject matter hereof.


Figure 2.3




 Home

 Help

 Live Chat

 Sign in

 Create Account



ACS Publications  
More Titled, More Cited, More Read.

**Ultrafast Cooling of Photoexcited Electrons in Gold Nanoparticle–Thiolated DNA Conjugates Involves the Dissociation of the Gold–Thiol Bond**

Author: Prashant K. Jain, Wei Qian, Mostafa A. El-Sayed  
Publication: Journal of the American Chemical Society  
Publisher: American Chemical Society  
Date: Feb 1, 2006  
Copyright © 2006, American Chemical Society

**PERMISSION/LICENSE IS GRANTED FOR YOUR ORDER AT NO CHARGE**


This type of permission/license, instead of the standard Terms and Conditions, is sent to you because no fee is being charged for your order. Please note the following:


- Permission is granted for your request in both print and electronic formats, and translations.
- If figures and/or tables were requested, they may be adapted or used in part.
- Please print this page for your records and send a copy of it to your publisher/graduate school.
- Appropriate credit for the requested material should be given as follows: "Reprinted (adapted) with permission from (COMPLETE REFERENCE CITATION). Copyright (YEAR) American Chemical Society." Insert appropriate information in place of the capitalized words.
- One-time permission is granted only for the use specified in your RightsLink request. No additional uses are granted (such as derivative works or other editions). For any uses, please submit a new request.


If credit is given to another source for the material you requested from RightsLink, permission must be obtained from that source.


[BACK](#)[CLOSE WINDOW](#)


Figure 2.4





 Home

 Help ▾

 Live Chat

 Sign In

 Create Account



ACS Publications  
Most Trusted. Most Cited. Most Read.

**Understanding Resonant Light-Triggered DNA Release from Plasmonic Nanoparticles**

Author: Amanda M. Goodman, Nathaniel J. Hogan, Samuel Gottheim, et al

Publication: ACS Nano

Publisher: American Chemical Society

Date: Jan 1, 2017

Copyright © 2017, American Chemical Society

**PERMISSION/LICENSE IS GRANTED FOR YOUR ORDER AT NO CHARGE**

This type of permission/license, instead of the standard Terms and Conditions, is sent to you because no fee is being charged for your order. Please note the following:

- Permission is granted for your request in both print and electronic formats, and translations.
- If figures and/or tables were requested, they may be adapted or used in part.
- Please print this page for your records and send a copy of it to your publisher/graduate school.
- Appropriate credit for the requested material should be given as follows: "Reprinted (adapted) with permission from (COMPLETE REFERENCE CITATION). Copyright (YEAR) American Chemical Society." Insert appropriate information in place of the capitalized words.
- One-time permission is granted only for the use specified in your RightsLink request. No additional uses are granted (such as derivative works or other editions). For any uses, please submit a new request.

If credit is given to another source for the material you requested from RightsLink, permission must be obtained from that source.

[BACK](#)[CLOSE WINDOW](#)

Figure 5.1

11/10/21, 2:55 PM

RightsLink Printable License

JOHN WILEY AND SONS LICENSE  
TERMS AND CONDITIONS

Nov 10, 2021

---

This Agreement between David A Hastman ("You") and John Wiley and Sons ("John Wiley and Sons") consists of your license details and the terms and conditions provided by John Wiley and Sons and Copyright Clearance Center.

License Number 5185520278658

License date Nov 10, 2021

Licensed Content  
Publisher John Wiley and Sons

Licensed Content  
Publication Small

Licensed Content  
Title Molecular Hyperthermia: Spatiotemporal Protein Unfolding and  
Inactivation by Nanosecond Plasmonic Heating

Licensed Content  
Author Peiyuan Kang, Zhuo Chen, Steven O. Nielsen, et al

Licensed Content  
Date Jul 11, 2017

<https://w100.copyright.com/AppDispatchServlet>

1/8



Licensed Content 13  
Volume

Licensed Content 36  
Issue

Licensed Content 7  
Pages

Type of use Dissertation/Thesis

Requestor type University/Academic

Format Print and electronic

Portion Figure/table

Number of 2  
figures/tables

Will you be 2  
translating? No

Title CONFINED PHOTOTHERMAL HEATING OF NANOPARTICLE  
DISPLAYED BIOMATERIALS

Institution name University of Maryland

Expected Nov 2021  
presentation date

<https://wiley100.copyright.com/AppDispatchServlet>

2/8

Portions Figure 1A, Figure 2C

David A Hastman  
4555 Overlook Ave SW

Requestor  
Location WASHINGTON, DC 20375  
United States  
Attn: David A Hastman

Publisher Tax ID EU826007151

Total 0.00 USD

Terms and Conditions

### TERMS AND CONDITIONS

This copyrighted material is owned by or exclusively licensed to John Wiley & Sons, Inc. or one of its group companies (each a "Wiley Company") or handled on behalf of a society with which a Wiley Company has exclusive publishing rights in relation to a particular work (collectively "WILEY"). By clicking "accept" in connection with completing this licensing transaction, you agree that the following terms and conditions apply to this transaction (along with the billing and payment terms and conditions established by the Copyright Clearance Center Inc., ("CCC's Billing and Payment terms and conditions"), at the time that you opened your RightsLink account (these are available at any time at <http://myaccount.copyright.com>).

#### Terms and Conditions

- The materials you have requested permission to reproduce or reuse (the "Wiley Materials") are protected by copyright.

<https://wiley100.copyright.com/AppDispatchServlet>

3/8

- You are hereby granted a personal, non-exclusive, non-sub licensable (on a stand-alone basis), non-transferable, worldwide, limited license to reproduce the Wiley Materials for the purpose specified in the licensing process. This license, and any CONTENT (PDF or image file) purchased as part of your order, is for a one-time use only and limited to any maximum distribution number specified in the license. The first instance of republication or reuse granted by this license must be completed within two years of the date of the grant of this license (although copies prepared before the end date may be distributed thereafter). The Wiley Materials shall not be used in any other manner or for any other purpose, beyond what is granted in the license. Permission is granted subject to an appropriate acknowledgement given to the author, title of the material/book/journal and the publisher. You shall also duplicate the copyright notice that appears in the Wiley publication in your use of the Wiley Material. Permission is also granted on the understanding that nowhere in the text is a previously published source acknowledged for all or part of this Wiley Material. Any third party content is expressly excluded from this permission.
- With respect to the Wiley Materials, all rights are reserved. Except as expressly granted by the terms of the license, no part of the Wiley Materials may be copied, modified, adapted (except for minor reformatting required by the new Publication), translated, reproduced, transferred or distributed, in any form or by any means, and no derivative works may be made based on the Wiley Materials without the prior permission of the respective copyright owner. For STM Signatory Publishers clearing permission under the terms of the [STM Permissions Guidelines](#) only, the terms of the license are extended to include subsequent editions and for editions in other languages, provided such editions are for the work as a whole in situ and does not involve the separate exploitation of the permitted figures or extracts. You may not alter, remove or suppress in any manner any copyright, trademark or other notices displayed by the Wiley Materials. You may not license, rent, sell, loan, lease, pledge, offer as security, transfer or assign the Wiley Materials on a stand-alone basis, or any of the rights granted to you hereunder to any other person.
- The Wiley Materials and all of the intellectual property rights therein shall at all times remain the exclusive property of John Wiley & Sons Inc, the Wiley Companies, or their respective licensors, and your interest therein is only that of having possession of and the right to reproduce the Wiley Materials pursuant to Section 2 herein during the continuance of this Agreement. You agree that you own no right, title or interest in or to the Wiley Materials or any of the intellectual property rights therein. You shall have no rights hereunder other than the license as provided for above in Section 2. No right, license or interest to any trademark, trade name, service mark or other branding ("Marks") of WILEY or its licensors is granted hereunder, and you agree that you

shall not assert any such right, license or interest with respect thereto

- NEITHER WILEY NOR ITS LICENSORS MAKES ANY WARRANTY OR REPRESENTATION OF ANY KIND TO YOU OR ANY THIRD PARTY, EXPRESS, IMPLIED OR STATUTORY, WITH RESPECT TO THE MATERIALS OR THE ACCURACY OF ANY INFORMATION CONTAINED IN THE MATERIALS, INCLUDING, WITHOUT LIMITATION, ANY IMPLIED WARRANTY OF MERCHANTABILITY, ACCURACY, SATISFACTORY QUALITY, FITNESS FOR A PARTICULAR PURPOSE, USABILITY, INTEGRATION OR NON-INFRINGEMENT AND ALL SUCH WARRANTIES ARE HEREBY EXCLUDED BY WILEY AND ITS LICENSORS AND WAIVED BY YOU.
- WILEY shall have the right to terminate this Agreement immediately upon breach of this Agreement by you.
- You shall indemnify, defend and hold harmless WILEY, its Licensors and their respective directors, officers, agents and employees, from and against any actual or threatened claims, demands, causes of action or proceedings arising from any breach of this Agreement by you.
- IN NO EVENT SHALL WILEY OR ITS LICENSORS BE LIABLE TO YOU OR ANY OTHER PARTY OR ANY OTHER PERSON OR ENTITY FOR ANY SPECIAL, CONSEQUENTIAL, INCIDENTAL, INDIRECT, EXEMPLARY OR PUNITIVE DAMAGES, HOWEVER CAUSED, ARISING OUT OF OR IN CONNECTION WITH THE DOWNLOADING, PROVISIONING, VIEWING OR USE OF THE MATERIALS REGARDLESS OF THE FORM OF ACTION, WHETHER FOR BREACH OF CONTRACT, BREACH OF WARRANTY, TORT, NEGLIGENCE, INFRINGEMENT OR OTHERWISE (INCLUDING, WITHOUT LIMITATION, DAMAGES BASED ON LOSS OF PROFITS, DATA, FILES, USE, BUSINESS OPPORTUNITY OR CLAIMS OF THIRD PARTIES), AND WHETHER OR NOT THE PARTY HAS BEEN ADVISED OF THE POSSIBILITY OF SUCH DAMAGES. THIS LIMITATION SHALL APPLY NOTWITHSTANDING ANY FAILURE OF ESSENTIAL PURPOSE OF ANY LIMITED REMEDY PROVIDED HEREIN.
- Should any provision of this Agreement be held by a court of competent jurisdiction to be illegal, invalid, or unenforceable, that provision shall be deemed amended to achieve as nearly as possible the same economic effect as the original provision, and the legality, validity and enforceability of the remaining provisions of this Agreement

hereby consents and submits to the personal jurisdiction of such court, waives any objection to venue in such court and consents to service of process by registered or certified mail, return receipt requested, at the last known address of such party.

#### WILEY OPEN ACCESS TERMS AND CONDITIONS

Wiley Publishes Open Access Articles in fully Open Access Journals and in Subscription journals offering Online Open. Although most of the fully Open Access journals publish open access articles under the terms of the Creative Commons Attribution (CC BY) License only, the subscription journals and a few of the Open Access Journals offer a choice of Creative Commons Licenses. The license type is clearly identified on the article.

##### The Creative Commons Attribution License

The [Creative Commons Attribution License \(CC-BY\)](#) allows users to copy, distribute and transmit an article, adapt the article and make commercial use of the article. The CC-BY license permits commercial and non-

##### Creative Commons Attribution Non-Commercial License

The [Creative Commons Attribution Non-Commercial \(CC-BY-NC\) License](#) permits use, distribution and reproduction in any medium, provided the original work is properly cited and is not used for commercial purposes.(see below)

##### Creative Commons Attribution-Non-Commercial-NoDerivs License

The [Creative Commons Attribution Non-Commercial-NoDerivs License](#) (CC-BY-NC-ND) permits use, distribution and reproduction in any medium, provided the original work is properly cited, is not used for commercial purposes and no modifications or adaptations are made. (see below)

##### Use by commercial "for-profit" organizations

Use of Wiley Open Access articles for commercial, promotional, or marketing purposes requires further explicit permission from Wiley and will be subject to a fee.

Further details can be found on Wiley Online Library  
<http://olabout.wiley.com/WileyCDA/Section/id-410895.html>

#### Other Terms and Conditions:

v1.10 Last updated September 2015

Questions? [customer care@copyright.com](mailto:customer care@copyright.com) or +1-855-239-3415 (toll free in the US) or +1-978-646-2777.

Figure 5.2

11/10/21, 3:06 PM

RightsLink Printable License

ELSEVIER LICENSE  
TERMS AND CONDITIONS

Nov 10, 2021

---

This Agreement between David A Hastman ("You") and Elsevier ("Elsevier") consists of your license details and the terms and conditions provided by Elsevier and Copyright Clearance Center.

License Number 5185520976474

License date Nov 10, 2021

Licensed Content  
Publisher Elsevier

Licensed Content  
Publication Journal of Molecular Biology

Licensed Content Title Reaction mechanism of alkaline phosphatase based on crystal structures Two-metal ion catalysis

Licensed Content Author Eunice E. Kim, Harold W. Wyckoff

Licensed Content Date Mar 20, 1991

Licensed Content Volume 218

<https://s100.copyright.com/AppDispatchServlet>

1/10

Licensed Content Issue	2
Licensed Content Pages	16
Start Page	449
End Page	464
Type of Use	reuse in a thesis/dissertation
Portion	figures/tables/illustrations
Number of figures/tables/illustrations	1
Format	both print and electronic
Are you the author of this Elsevier article?	No
Will you be translating?	No
Title	CONFINED PHOTOTHERMAL HEATING OF NANOPARTICLE DISPLAYED BIOMATERIALS
Institution name	University of Maryland

Expected presentation date Nov 2021

Portions AP structure

David A Hastman  
4555 Overlook Ave SW

Requestor Location

WASHINGTON, DC 20375  
United States  
Attn: David A Hastman

Publisher Tax ID 98-0397604

Total 0.00 USD

Terms and Conditions

#### INTRODUCTION

1. The publisher for this copyrighted material is Elsevier. By clicking "accept" in connection with completing this licensing transaction, you agree that the following terms and conditions apply to this transaction (along with the Billing and Payment terms and conditions established by Copyright Clearance Center, Inc. ("CCC"), at the time that you opened your Rightslink account and that are available at any time at <http://myaccount.copyright.com>).

#### GENERAL TERMS

2. Elsevier hereby grants you permission to reproduce the aforementioned material subject to the terms and conditions indicated.

3. Acknowledgement: If any part of the material to be used (for example, figures) has appeared in our publication with credit or acknowledgement to another source, permission must also be sought from that source. If such permission is not obtained then that material may not be included in your publication/copies. Suitable acknowledgement to the source

must be made, either as a footnote or in a reference list at the end of your publication, as follows:

"Reprinted from Publication title, Vol /edition number, Author(s), Title of article / title of chapter, Pages No., Copyright (Year), with permission from Elsevier [OR APPLICABLE SOCIETY COPYRIGHT OWNER]." Also Lancet special credit - "Reprinted from The Lancet, Vol. number, Author(s), Title of article, Pages No., Copyright (Year), with permission from Elsevier."

4. Reproduction of this material is confined to the purpose and/or media for which permission is hereby given.

5. Altering/Modifying Material: Not Permitted. However figures and illustrations may be altered/adapted minimally to serve your work. Any other abbreviations, additions, deletions and/or any other alterations shall be made only with prior written authorization of Elsevier Ltd. (Please contact Elsevier's permissions helpdesk [here](#)). No modifications can be made to any Lancet figures/tables and they must be reproduced in full.

6. If the permission fee for the requested use of our material is waived in this instance, please be advised that your future requests for Elsevier materials may attract a fee.

7. Reservation of Rights: Publisher reserves all rights not specifically granted in the combination of (i) the license details provided by you and accepted in the course of this licensing transaction, (ii) these terms and conditions and (iii) CCC's Billing and Payment terms and conditions.

8. License Contingent Upon Payment: While you may exercise the rights licensed immediately upon issuance of the license at the end of the licensing process for the transaction, provided that you have disclosed complete and accurate details of your proposed use, no license is finally effective unless and until full payment is received from you (either by publisher or by CCC) as provided in CCC's Billing and Payment terms and conditions. If full payment is not received on a timely basis, then any license preliminarily granted shall be deemed automatically revoked and shall be void as if never granted. Further, in the event that you breach any of these terms and conditions or any of CCC's Billing and Payment terms and conditions, the license is automatically revoked and shall be void as if never granted. Use of materials as described in a revoked license, as well as any use of the materials beyond the scope of an unrevoked license, may constitute copyright infringement and publisher reserves the right to take any and all action to protect its copyright in the materials.



9. **Warranties:** Publisher makes no representations or warranties with respect to the licensed material.

10. **Indemnity:** You hereby indemnify and agree to hold harmless publisher and CCC, and their respective officers, directors, employees and agents, from and against any and all claims arising out of your use of the licensed material other than as specifically authorized pursuant to this license.

11. **No Transfer of License:** This license is personal to you and may not be sublicensed, assigned, or transferred by you to any other person without publisher's written permission.

12. **No Amendment Except in Writing:** This license may not be amended except in a writing signed by both parties (or, in the case of publisher, by CCC on publisher's behalf).

13. **Objection to Contrary Terms:** Publisher hereby objects to any terms contained in any purchase order, acknowledgment, check endorsement or other writing prepared by you, which terms are inconsistent with these terms and conditions or CCC's Billing and Payment terms and conditions. These terms and conditions, together with CCC's Billing and Payment terms and conditions (which are incorporated herein), comprise the entire agreement between you and publisher (and CCC) concerning this licensing transaction. In the event of any conflict between your obligations established by these terms and conditions and those established by CCC's Billing and Payment terms and conditions, these terms and conditions shall control.

14. **Revocation:** Elsevier or Copyright Clearance Center may deny the permissions described in this License at their sole discretion, for any reason or no reason, with a full refund payable to you. Notice of such denial will be made using the contact information provided by you. Failure to receive such notice will not alter or invalidate the denial. In no event will Elsevier or Copyright Clearance Center be responsible or liable for any costs, expenses or damage incurred by you as a result of a denial of your permission request, other than a refund of the amount(s) paid by you to Elsevier and/or Copyright Clearance Center for denied permissions.

#### LIMITED LICENSE

The following terms and conditions apply only to specific license types:

15. **Translation:** This permission is granted for non-exclusive world **English** rights only unless your license was granted for translation rights. If you licensed translation rights you may only translate this content into the languages you requested. A professional translator must perform all translations and reproduce the content word for word preserving the integrity of the article.

**16. Posting licensed content on any Website:** The following terms and conditions apply as follows: Licensing material from an Elsevier journal: All content posted to the web site must maintain the copyright information line on the bottom of each image; A hyper-text must be included to the Homepage of the journal from which you are licensing at <http://www.sciencedirect.com/science/journal/xxxxx> or the Elsevier homepage for books at <http://www.elsevier.com>; Central Storage: This license does not include permission for a scanned version of the material to be stored in a central repository such as that provided by Heron/XanEdu.

Licensing material from an Elsevier book: A hyper-text link must be included to the Elsevier homepage at <http://www.elsevier.com>. All content posted to the web site must maintain the copyright information line on the bottom of each image.

**Posting licensed content on Electronic reserve:** In addition to the above the following clauses are applicable: The web site must be password-protected and made available only to bona fide students registered on a relevant course. This permission is granted for 1 year only. You may obtain a new license for future website posting.

**17. For journal authors:** the following clauses are applicable in addition to the above:

**Preprints:**

A preprint is an author's own write-up of research results and analysis, it has not been peer-reviewed, nor has it had any other value added to it by a publisher (such as formatting, copyright, technical enhancement etc.).

Authors can share their preprints anywhere at any time. Preprints should not be added to or enhanced in any way in order to appear more like, or to substitute for, the final versions of articles however authors can update their preprints on arXiv or RePEc with their Accepted Author Manuscript (see below).

If accepted for publication, we encourage authors to link from the preprint to their formal publication via its DOI. Millions of researchers have access to the formal publications on ScienceDirect, and so links will help users to find, access, cite and use the best available version. Please note that Cell Press, The Lancet and some society-owned have different preprint policies. Information on these policies is available on the journal homepage.

**Accepted Author Manuscripts:** An accepted author manuscript is the manuscript of an article that has been accepted for publication and which typically includes author-incorporated changes suggested during submission, peer review and editor-author communications.

Authors can share their accepted author manuscript:

- immediately
  - via their non-commercial person homepage or blog
  - by updating a preprint in arXiv or RePEc with the accepted manuscript
  - via their research institute or institutional repository for internal institutional uses or as part of an invitation-only research collaboration work-group
  - directly by providing copies to their students or to research collaborators for their personal use
  - for private scholarly sharing as part of an invitation-only work group on commercial sites with which Elsevier has an agreement
- After the embargo period
  - via non-commercial hosting platforms such as their institutional repository
  - via commercial sites with which Elsevier has an agreement

In all cases accepted manuscripts should:

- link to the formal publication via its DOI
- bear a CC-BY-NC-ND license - this is easy to do
- if aggregated with other manuscripts, for example in a repository or other site, be shared in alignment with our hosting policy not be added to or enhanced in any way to appear more like, or to substitute for, the published journal article.

**Published journal article (JPA):** A published journal article (PJA) is the definitive final record of published research that appears or will appear in the journal and embodies all value-adding publishing activities including peer review co-ordination, copy-editing, formatting, (if relevant) pagination and online enrichment.

Policies for sharing publishing journal articles differ for subscription and gold open access articles:

**Subscription Articles:** If you are an author, please share a link to your article rather than the full-text. Millions of researchers have access to the formal publications on ScienceDirect, and so links will help your users to find, access, cite, and use the best available version.

Theses and dissertations which contain embedded PJAs as part of the formal submission can be posted publicly by the awarding institution with DOI links back to the formal publications on ScienceDirect.

If you are affiliated with a library that subscribes to ScienceDirect you have additional private sharing rights for others' research accessed under that agreement. This includes use

for classroom teaching and internal training at the institution (including use in course packs and courseware programs), and inclusion of the article for grant funding purposes.

**Gold Open Access Articles:** May be shared according to the author-selected end-user license and should contain a [CrossMark logo](#), the end user license, and a DOI link to the formal publication on ScienceDirect.

Please refer to Elsevier's [posting policy](#) for further information.

**18. For book authors** the following clauses are applicable in addition to the above: Authors are permitted to place a brief summary of their work online only. You are not allowed to download and post the published electronic version of your chapter, nor may you scan the printed edition to create an electronic version. **Posting to a repository:** Authors are permitted to post a summary of their chapter only in their institution's repository.

**19. Thesis/Dissertation:** If your license is for use in a thesis/dissertation your thesis may be submitted to your institution in either print or electronic form. Should your thesis be published commercially, please reapply for permission. These requirements include permission for the Library and Archives of Canada to supply single copies, on demand, of the complete thesis and include permission for Proquest/UMI to supply single copies, on demand, of the complete thesis. Should your thesis be published commercially, please reapply for permission. Theses and dissertations which contain embedded PJAs as part of the formal submission can be posted publicly by the awarding institution with DOI links back to the formal publications on ScienceDirect.

#### **Elsevier Open Access Terms and Conditions**

You can publish open access with Elsevier in hundreds of open access journals or in nearly 2000 established subscription journals that support open access publishing. Permitted third party re-use of these open access articles is defined by the author's choice of Creative Commons user license. See our [open access license policy](#) for more information.

#### **Terms & Conditions applicable to all Open Access articles published with Elsevier:**

Any reuse of the article must not represent the author as endorsing the adaptation of the article nor should the article be modified in such a way as to damage the author's honour or reputation. If any changes have been made, such changes must be clearly indicated.

The author(s) must be appropriately credited and we ask that you include the end user license and a DOI link to the formal publication on ScienceDirect.

If any part of the material to be used (for example, figures) has appeared in our publication with credit or acknowledgement to another source it is the responsibility of the user to ensure their reuse complies with the terms and conditions determined by the rights holder.

**Additional Terms & Conditions applicable to each Creative Commons user license:**

**CC BY:** The CC-BY license allows users to copy, to create extracts, abstracts and new works from the Article, to alter and revise the Article and to make commercial use of the Article (including reuse and/or resale of the Article by commercial entities), provided the user gives appropriate credit (with a link to the formal publication through the relevant DOI), provides a link to the license, indicates if changes were made and the licensor is not represented as endorsing the use made of the work. The full details of the license are available at <http://creativecommons.org/licenses/by/4.0>.

**CC BY-NC-SA:** The CC BY-NC-SA license allows users to copy, to create extracts, abstracts and new works from the Article, to alter and revise the Article, provided this is not done for commercial purposes, and that the user gives appropriate credit (with a link to the formal publication through the relevant DOI), provides a link to the license, indicates if changes were made and the licensor is not represented as endorsing the use made of the work. Further, any new works must be made available on the same conditions. The full details of the license are available at <http://creativecommons.org/licenses/by-nc-sa/4.0>.

**CC BY-NC-ND:** The CC BY-NC-ND license allows users to copy and distribute the Article, provided this is not done for commercial purposes and further does not permit distribution of the Article if it is changed or edited in any way, and provided the user gives appropriate credit (with a link to the formal publication through the relevant DOI), provides a link to the license, and that the licensor is not represented as endorsing the use made of the work. The full details of the license are available at <http://creativecommons.org/licenses/by-nc-nd/4.0>. Any commercial reuse of Open Access articles published with a CC BY-NC-SA or CC BY-NC-ND license requires permission from Elsevier and will be subject to a fee.

Commercial reuse includes:

- Associating advertising with the full text of the Article
- Charging fees for document delivery or access
- Article aggregation
- Systematic distribution via e-mail lists or share buttons

Posting or linking by commercial companies for use by customers of those companies.

<https://is100.copyright.com/AppDispatchServlet>

9/10

11/10/21, 3:05 PM

RightsLink Printable License

**20. Other Conditions:**

v1.10

Questions? [customer@copyright.com](mailto:customer@copyright.com) or +1-855-239-3415 (toll free in the US) or +1-978-646-2777.

## Bibliography

1. Samanta, A.; Medintz, I. L., Nanoparticles and DNA – A Powerful and Growing Functional Combination in Bionanotechnology. *Nanoscale* **2016**, 8 (17), 9037-9095.
2. Medintz, I. L.; Uyeda, H. T.; Goldman, E. R.; Mattoussi, H., Quantum Dot Bioconjugates for Imaging, Labelling and Sensing. *Nature materials* **2005**, 4 (6), 435-46.
3. Hartland, G. V., Optical Studies of Dynamics in Noble Metal Nanostructures. *Chemical Reviews* **2011**, 111 (6), 3858-3887.
4. Mahmoudi, M.; Sant, S.; Wang, B.; Laurent, S.; Sen, T., Superparamagnetic Iron Oxide Nanoparticles (SPIONs): Development, Surface Modification and Applications in Chemotherapy. *Advanced Drug Delivery Reviews* **2011**, 63 (1), 24-46.
5. Medintz, I. L.; Stewart, M. H.; Trammell, S. A.; Susumu, K.; Delehanty, J. B.; Mei, B. C.; Melinger, J. S.; Blanco-Canosa, J. B.; Dawson, P. E.; Mattoussi, H., Quantum-Dot/Dopamine Bioconjugates Function as Redox Coupled Assemblies for In Vitro and Intracellular pH Sensing. *Nature Materials* **2010**, 9 (8), 676-84.
6. Brown III, C. W.; Oh, E.; Hastman, D. A.; Walper, S. A.; Susumu, K.; Stewart, M. H.; Deschamps, J. R.; Medintz, I. L., Kinetic Enhancement of the Diffusion-limited Enzyme Beta-galactosidase when Displayed with Quantum Dots. *RSC Advances* **2015**, 5 (113), 93089-93094.
7. Sapsford, K. E.; Algar, W. R.; Berti, L.; Gemmill, K. B.; Casey, B. J.; Oh, E.; Stewart, M. H.; Medintz, I. L., Functionalizing Nanoparticles with Biological Molecules: Developing Chemistries that Facilitate Nanotechnology. *Chemical Reviews* **2013**, 113 (3), 1904-2074.
8. Sangtani, A.; Nag, O. K.; Oh, E.; Stewart, M. H.; Delehanty, J. B., Quantum Dot-Enabled Membrane-tethering and Enhanced Photoactivation of Chlorin-e6. *Journal of Nanoparticle Research* **2021**, 23 (8), 159.
9. Mathur, D.; Klein, W. P.; Chiriboga, M.; Bui, H.; Oh, E.; Nita, R.; Naciri, J.; Johns, P.; Fontana, J.; Díaz, S. A.; Medintz, I. L., Analyzing Fidelity and Reproducibility of DNA Templated Plasmonic Nanostructures. *Nanoscale* **2019**, 11 (43), 20693-20706.
10. Wu, R.; Peng, H.; Zhu, J.-J.; Jiang, L.-P.; Liu, J., Attaching DNA to Gold Nanoparticles With a Protein Corona. *Frontiers in Chemistry* **2020**, 8 (121).
11. Sangtani, A.; Nag, O. K.; Field, L. D.; Breger, J. C.; Delehanty, J. B., Multifunctional Nanoparticle Composites: Progress in the use of Soft and Hard

Nanoparticles for Drug Delivery and Imaging. *WIREs Nanomedicine and Nanobiotechnology* **2017**, 9 (6), e1466.

12. Goodman, A. M.; Hogan, N. J.; Gottheim, S.; Li, C.; Clare, S. E.; Halas, N. J., Understanding Resonant Light-Triggered DNA Release from Plasmonic Nanoparticles. *ACS Nano* **2017**, 11 (1), 171-179.

13. Schwaminger, S. P.; Fraga-García, P.; Eigenfeld, M.; Becker, T. M.; Berensmeier, S., Magnetic Separation in Bioprocessing Beyond the Analytical Scale: From Biotechnology to the Food Industry. *Frontiers in Bioengineering and Biotechnology* **2019**, 7 (233).

14. Nel, A. E.; Mädler, L.; Velegol, D.; Xia, T.; Hoek, E. M. V.; Somasundaran, P.; Klaessig, F.; Castranova, V.; Thompson, M., Understanding Biophysicochemical Interactions at the Nano–Bio Interface. *Nature Materials* **2009**, 8 (7), 543-557.

15. Breger, J. C.; Oh, E.; Susumu, K.; Klein, W. P.; Walper, S. A.; Ancona, M. G.; Medintz, I. L., Nanoparticle Size Influences Localized Enzymatic Enhancement—A Case Study with Phosphotriesterase. *Bioconjugate Chemistry* **2019**, 30 (7), 2060-2074.

16. Chen, C.; Wang, W.; Ge, J.; Zhao, X. S., Kinetics and Thermodynamics of DNA Hybridization on Gold Nanoparticles. *Nucleic Acids Research* **2009**, 37 (11), 3756-3765.

17. Giljohann, D. A.; Seferos, D. S.; Daniel, W. L.; Massich, M. D.; Patel, P. C.; Mirkin, C. A., Gold Nanoparticles for Biology and Medicine. *Angewandte Chemie International Edition* **2010**, 49 (19), 3280-3294.

18. Kimling, J.; Maier, M.; Okenve, B.; Kotaidis, V.; Ballot, H.; Plech, A., Turkevich Method for Gold Nanoparticle Synthesis Revisited. *The Journal of Physical Chemistry B* **2006**, 110 (32), 15700-15707.

19. Hostetler, M. J.; Wingate, J. E.; Zhong, C.-J.; Harris, J. E.; Vachet, R. W.; Clark, M. R.; Londono, J. D.; Green, S. J.; Stokes, J. J.; Wignall, G. D.; Glish, G. L.; Porter, M. D.; Evans, N. D.; Murray, R. W., Alkanethiolate Gold Cluster Molecules with Core Diameters from 1.5 to 5.2 nm: Core and Monolayer Properties as a Function of Core Size. *Langmuir* **1998**, 14 (1), 17-30.

20. Jauffred, L.; Samadi, A.; Klingberg, H.; Bendix, P. M.; Oddershede, L. B., Plasmonic Heating of Nanostructures. *Chemical Reviews* **2019**, 119 (13), 8087-8130.

21. Perrault, S. D.; Chan, W. C., Synthesis and Surface Modification of Highly Monodispersed, Spherical Gold Nanoparticles of 50-200 nm. *J. Am. Chem. Soc.* **2009**, 131 (47), 17042-3.

22. Carvalho-de-Souza, J. A.; Nag, O. K.; oh, E.; Huston, A. J.; Vurgaftman, I.; Pepperberg, D.; Bezanilla, F.; Delehanty, J. B., Cholesterol Functionalization of Gold Nanoparticles Enables Neural Photo-Activation. *Biophysical Journal* **2019**, *116* (3), 276a.
23. Han, G.; Ghosh, P.; Rotello, V. M., Functionalized Gold Nanoparticles for Drug Delivery. *Nanomedicine (London, England)* **2007**, *2* (1), 113-123.
24. Huang, X.; El-Sayed, M. A., Gold Nanoparticles: Optical Properties and Implementations in Cancer Diagnosis and Photothermal Therapy. *Journal of Advanced Research* **2010**, *1* (1), 13-28.
25. Huang, X.; Jain, P. K.; El-Sayed, I. H.; El-Sayed, M. A., Plasmonic Photothermal Therapy (PPTT) using Gold Nanoparticles. *Lasers in Medical Science* **2008**, *23* (3), 217.
26. Amendola, V.; Pilot, R.; Frasconi, M.; Marago, O. M.; Iati, M. A., Surface Plasmon Resonance in Gold Nanoparticles: A Review. *Journal of Physics: Condensed Matter* **2017**, *29* (20), 203002.
27. Baffou, G., *Thermoplasmonics*. World Scientific: 2017.
28. Maier, S. A., *Plasmonics: Fundamentals and Applications*. Springer Science & Business Media: 2007.
29. Magnozzi, M.; Proietti Zaccaria, R.; Catone, D.; O'Keeffe, P.; Paladini, A.; Toschi, F.; Alabastri, A.; Canepa, M.; Bisio, F., Interband Transitions Are More Efficient Than Plasmonic Excitation in the Ultrafast Melting of Electromagnetically Coupled Au Nanoparticles. *The Journal of Physical Chemistry C* **2019**, *123* (27), 16943-16950.
30. Kang, P.; Chen, Z.; Nielsen, S. O.; Hoyt, K.; D'Arcy, S.; Gassensmith, J. J.; Qin, Z., Molecular Hyperthermia: Spatiotemporal Protein Unfolding and Inactivation by Nanosecond Plasmonic Heating. *Small* **2017**, *13* (36), 1700841.
31. Barhoumi, A.; Huschka, R.; Bardhan, R.; Knight, M. W.; Halas, N. J., Light-Induced Release of DNA from Plasmon-Resonant Nanoparticles: Towards Light-Controlled Gene Therapy. *Chemical Physics Letters* **2009**, *482* (4), 171-179.
32. Song, J.; Yang, X.; Jacobson, O.; Lin, L.; Huang, P.; Niu, G.; Ma, Q.; Chen, X., Sequential Drug Release and Enhanced Photothermal and Photoacoustic Effect of Hybrid Reduced Graphene Oxide-Loaded Ultrasmall Gold Nanorod Vesicles for Cancer Therapy. *ACS Nano* **2015**, *9* (9), 9199-9209.
33. Boyd, D. A.; Greengard, L.; Brongersma, M.; El-Naggar, M. Y.; Goodwin, D. G., Plasmon-Assisted Chemical Vapor Deposition. *Nano Letters* **2006**, *6* (11), 2592-



2597.

34. Lasne, D.; Blab, G. A.; Berciaud, S.; Heine, M.; Groc, L.; Choquet, D.; Cognet, L.; Lounis, B., Single Nanoparticle Photothermal Tracking (SNaPT) of 5-nm Gold Beads in Live Cells. *Biophysical Journal* **2006**, *91* (12), 4598-4604.
35. Urban, A. S.; Pfeiffer, T.; Fedoruk, M.; Lutich, A. A.; Feldmann, J., Single-Step Injection of Gold Nanoparticles through Phospholipid Membranes. *ACS Nano* **2011**, *5* (5), 3585-3590.
36. Baffou, G.; Rigneault, H., Femtosecond-Pulsed Optical Heating of Gold Nanoparticles. *Physical Review B* **2011**, *84* (3), 035415.
37. Sliney, D. H., Radiometric Quantities and Units used in Photobiology and Photochemistry: Recommendations of the Commission Internationale de L'Eclairage (International Commission on Illumination). *Photochem. Photobiol.* **2007**, *83* (2), 425-32.
38. Govorov, A. O.; Richardson, H. H., Generating Heat with Metal Nanoparticles. *Nano Today* **2007**, *2* (1), 30-38.
39. Hogan, N. J.; Urban, A. S.; Ayala-Orozco, C.; Pimpinelli, A.; Nordlander, P.; Halas, N. J., Nanoparticles Heat through Light Localization. *Nano Letters* **2014**, *14* (8), 4640-4645.
40. Bretschneider, J. C.; Reismann, M.; von Plessen, G.; Simon, U., Photothermal Control of the Activity of HRP-Functionalized Gold Nanoparticles. *Small* **2009**, *5* (22), 2549-2553.
41. Wang, X.; Ou, G.; Zhou, K.; Wang, X.; Wang, L.; Zhang, X.; Feng, Y.; Bai, Y.; Wu, H.; Xu, Z.; Ge, J., Targeted-Heating Enzyme Systems Based on Photothermal Materials. *ChemBioChem* **2019**, *0* (ja).
42. Inouye, H.; Tanaka, K.; Tanahashi, I.; Hirao, K., Ultrafast Dynamics of Nonequilibrium Electrons in a Gold Nanoparticle system. *Physical Review B* **1998**, *57* (18), 11334-11340.
43. Arbouet, A.; Voisin, C.; Christofilos, D.; Langot, P.; Fatti, N. D.; Vallée, F.; Lermé, J.; Celep, G.; Cottancin, E.; Gaudry, M.; Pellarin, M.; Broyer, M.; Maillard, M.; Pileni, M. P.; Treguer, M., Electron-Phonon Scattering in Metal Clusters. *Physical Review Letters* **2003**, *90* (17), 177401.
44. Metwally, K.; Mensah, S.; Baffou, G., Fluence Threshold for Photothermal Bubble Generation Using Plasmonic Nanoparticles. *The Journal of Physical Chemistry C* **2015**, *119* (51), 28586-28596.

45. Riley, R. S.; Dang, M. N.; Billingsley, M. M.; Abraham, B.; Gundlach, L.; Day, E. S., Evaluating the Mechanisms of Light-Triggered siRNA Release from Nanoshells for Temporal Control Over Gene Regulation. *Nano Letters* **2018**, *18* (6), 3565-3570.
46. Kang, P.; Chen, Z.; Nielsen, S. O.; Hoyt, K.; D'Arcy, S.; Gassensmith, J. J.; Qin, Z., Molecular Hyperthermia: Spatiotemporal Protein Unfolding and Inactivation by Nanosecond Plasmonic Heating. *Small* **2017**, *13* (36).
47. Sarkar, D.; Kang, P.; Nielsen, S. O.; Qin, Z., Non-Arrhenius Reaction-Diffusion Kinetics for Protein Inactivation over a Large Temperature Range. *ACS Nano* **2019**, *13* (8), 8669-8679.
48. Poon, L.; Zandberg, W.; Hsiao, D.; Erno, Z.; Sen, D.; Gates, B. D.; Branda, N. R., Photothermal Release of Single-Stranded DNA from the Surface of Gold Nanoparticles Through Controlled Denaturing and Au–S Bond Breaking. *ACS Nano* **2010**, *4* (11), 6395-6403.
49. Rudnitski, F.; Feineis, S.; Rahmzadeh, R.; Endl, E.; Lutz, J.; Groll, J.; Hüttmann, G., siRNA Release from Gold Nanoparticles by Nanosecond Pulsed Laser Irradiation and Analysis of the Involved Temperature Increase. *Journal of Biophotonics* **2018**, *11* (9), e201700329.
50. Thibaudau, F., Ultrafast Photothermal Release of DNA from Gold Nanoparticles. *The Journal of Physical Chemistry Letters* **2012**, *3* (7), 902-907.
51. Kang, P.; Chen, Z.; Nielsen, S. O.; Hoyt, K.; D'Arcy, S.; Gassensmith, J. J.; Qin, Z., Thermoplasmonics: Molecular Hyperthermia: Spatiotemporal Protein Unfolding and Inactivation by Nanosecond Plasmonic Heating (Small 36/2017). *Small* **2017**, *13* (36).
52. Hill, H. D.; Millstone, J. E.; Banholzer, M. J.; Mirkin, C. A., The Role Radius of Curvature Plays in Thiolated Oligonucleotide Loading on Gold Nanoparticles. *ACS Nano* **2009**, *3* (2), 418-424.
53. Hondred, J. A.; Breger, J. C.; Garland, N. T.; Oh, E.; Susumu, K.; Walper, S. A.; Medintz, I. L.; Claussen, J. C., Enhanced Enzymatic Activity from Phosphotriesterase Trimer Gold Nanoparticle Bioconjugates for Pesticide Detection. *Analyst* **2017**, *142* (17), 3261-3271.
54. Samanta, A.; Breger, J. C.; Susumu, K.; Oh, E.; Walper, S. A.; Bassim, N.; Medintz, I. L., DNA–Nanoparticle Composites Synergistically Enhance Organophosphate Hydrolase Enzymatic Activity. *ACS Applied Nano Materials* **2018**, *1* (7), 3091-3097.

55. Vranish, J. N.; Ancona, M. G.; Oh, E.; Susumu, K.; Lasarte Aragonés, G.; Breger, J. C.; Walper, S. A.; Medintz, I. L., Enhancing Coupled Enzymatic Activity by Colocalization on Nanoparticle Surfaces: Kinetic Evidence for Directed Channeling of Intermediates. *ACS Nano* **2018**, *12* (8), 7911-7926.
56. Crooke, S. T., Molecular Mechanisms of Action of Antisense Drugs. *Biochimica et Biophysica acta* **1999**, *1489* (1), 31-44.
57. Akhtar, S.; Hughes, M. D.; Khan, A.; Bibby, M.; Hussain, M.; Nawaz, Q.; Double, J.; Sayyed, P., The Delivery of Antisense Therapeutics. *Advanced Drug Delivery Reviews* **2000**, *44* (1), 3-21.
58. Stull, R. A.; Szoka, F. C., Jr., Antigene, Ribozyme and Aptamer Nucleic Acid Drugs: Progress and Prospects. *Pharmaceutical Research* **1995**, *12* (4), 465-83.
59. McManus, M. T.; Sharp, P. A., Gene Silencing in Mammals by Small Interfering RNAs. *Nature Reviews Genetics* **2002**, *3* (10), 737-747.
60. Fratila, R. M.; Mitchell, S. G.; del Pino, P.; Grazu, V.; de la Fuente, J. M., Strategies for the Biofunctionalization of Gold and Iron Oxide Nanoparticles. *Langmuir* **2014**, *30* (50), 15057-15071.
61. Giljohann, D. A.; Seferos, D. S.; Daniel, W. L.; Massich, M. D.; Patel, P. C.; Mirkin, C. A., Gold Nanoparticles for Biology and Medicine. *Angew. Chem. Int. Ed. Engl.* **2010**, *49* (19), 3280-3294.
62. Florentsen, C. D.; West, A.-K. V.; Danielsen, H. M. D.; Semsey, S.; Bendix, P. M.; Oddershede, L. B., Quantification of Loading and Laser-Assisted Release of RNA from Single Gold Nanoparticles. *Langmuir* **2018**, *34* (49), 14891-14898.
63. Qin, Z.; Bischof, J. C., Thermophysical and Biological Responses of Gold Nanoparticle Laser Heating. *Chemical Society Reviews* **2012**, *41* (3), 1191-1217.
64. Patil, S. D.; Rhodes, D. G.; Burgess, D. J., DNA-based Therapeutics and DNA Delivery Systems: A Comprehensive Review. *AAPS J* **2005**, *7* (1), E61-E77.
65. Mathur, D.; Medintz, I. L., Analyzing DNA Nanotechnology: A Call to Arms For The Analytical Chemistry Community. *Analytical Chemistry* **2017**, *89* (5), 2646-2663.
66. Bui, H.; Díaz, S. A.; Fontana, J.; Chiriboga, M.; Veneziano, R.; Medintz, I. L., Utilizing the Organizational Power of DNA Scaffolds for New Nanophotonic Applications. *Advanced Optical Materials* **2019**, *7* (18), 1900562.
67. Bui, H.; Brown, C. W., 3rd; Buckhout-White, S.; Díaz, S. A.; Stewart, M. H.; Susumu, K.; Oh, E.; Ancona, M. G.; Goldman, E. R.; Medintz, I. L., Transducing

Protease Activity into DNA Output for Developing Smart Bionanosensors. *Small* **2019**, *15* (14), e1805384.

68. Mathur, D.; Medintz, I. L., The Growing Development of DNA Nanostructures for Potential Healthcare-Related Applications. *Advanced Healthcare Materials* **2019**, *8* (9), 1801546.

69. Demers, L. M.; Mirkin, C. A.; Mucic, R. C.; Reynolds, R. A.; Letsinger, R. L.; Elghanian, R.; Viswanadham, G., A Fluorescence-Based Method for Determining the Surface Coverage and Hybridization Efficiency of Thiol-Capped Oligonucleotides Bound to Gold Thin Films and Nanoparticles. *Analytical Chemistry* **2000**, *72* (22), 5535-5541.

70. Daniel, M.-C.; Astruc, D., Gold Nanoparticles: Assembly, Supramolecular Chemistry, Quantum-Size-Related Properties, and Applications toward Biology, Catalysis, and Nanotechnology. *Chemical Reviews* **2004**, *104* (1), 293-346.

71. Zeng, S.; Yong, K.-T.; Roy, I.; Dinh, X.-Q.; Yu, X.; Luan, F., A Review on Functionalized Gold Nanoparticles for Biosensing Applications. *Plasmonics* **2011**, *6* (3), 491.

72. Li, H.; Rothberg, L., Colorimetric Detection of DNA Sequences based on Electrostatic Interactions with Unmodified Gold Nanoparticles. *Proceedings of the National Academy of Sciences of the United States of America* **2004**, *101* (39), 14036-14039.

73. Nelson, E. M.; Rothberg, L. J., Kinetics and Mechanism of Single-Stranded DNA Adsorption onto Citrate-Stabilized Gold Nanoparticles in Colloidal Solution. *Langmuir* **2011**, *27* (5), 1770-1777.

74. Zhou, W.; Hu, K.; Kwee, S.; Tang, L.; Wang, Z.; Xia, J.; Li, X., Gold Nanoparticle Aggregation-Induced Quantitative Photothermal Biosensing Using a Thermometer: A Simple and Universal Biosensing Platform. *Analytical Chemistry* **2020**, *92* (3), 2739-2747.

75. Reismann, M.; Bretschneider, J. C.; Plessen, G. v.; Simon, U., Reversible Photothermal Melting of DNA in DNA–Gold-Nanoparticle Networks. *Small* **2008**, *4* (5), 607-610.

76. Yamashita, S.; Fukushima, H.; Akiyama, Y.; Niidome, Y.; Mori, T.; Katayama, Y.; Niidome, T., Controlled-Release System of Single-Stranded DNA Triggered by the Photothermal Effect of Gold Nanorods and its In Vivo Application. *Bioorganic & Medicinal Chemistry* **2011**, *19* (7), 2130-2135.

77. Armstrong, R. E.; Riskowski, R. A.; Strouse, G. F., Nanometal Surface Energy Transfer Optical Ruler for Measuring a Human Telomere Structure. *Photochem.*

*Photobiol.* **2015**, *91* (3), 732-738.

78. Breshike, C. J.; Riskowski, R. A.; Strouse, G. F., Leaving Förster Resonance Energy Transfer Behind: Nanometal Surface Energy Transfer Predicts the Size-Enhanced Energy Coupling between a Metal Nanoparticle and an Emitting Dipole. *J. Phys. Chem. C* **2013**, *117* (45), 23942-23949.

79. Carnevale, K. J. F.; Riskowski, R. A.; Strouse, G. F., A Gold Nanoparticle Bio-Optical Transponder to Dynamically Monitor Intracellular pH. *ACS Nano* **2018**, *12* (6), 5956-5968.

80. Jain, P. K.; Qian, W.; El-Sayed, M. A., Ultrafast Cooling of Photoexcited Electrons in Gold Nanoparticle–Thiolated DNA Conjugates Involves the Dissociation of the Gold–Thiol Bond. *Journal of the American Chemical Society* **2006**, *128* (7), 2426-2433.

81. Jain, P. K.; Qian, W.; El-Sayed, M. A., Ultrafast Cooling of Photoexcited Electrons in Gold Nanoparticle–Thiolated DNA Conjugates Involves the Dissociation of the Gold–Thiol Bond. *J. Am. Chem. Soc.* **2006**, *128* (7), 2426-2433.

82. Riley, R. S.; Dang, M. N.; Billingsley, M. M.; Abraham, B.; Gundlach, L.; Day, E. S., Evaluating the Mechanisms of Light-Triggered siRNA Release from Nanoshells for Temporal Control Over Gene Regulation. *Nano Lett.* **2018**, *18* (6), 3565-3570.

83. Rudnitzki, F.; Feineis, S.; Rahmzadeh, R.; Endl, E.; Lutz, J.; Groll, J.; Hüttmann, G., siRNA Release from Gold Nanoparticles by Nanosecond Pulsed Laser Irradiation and Analysis of the Involved Temperature Increase. *J. Biophotonics* **2018**, *11* (9), e201700329.

84. Thibaudau, F., Ultrafast Photothermal Release of DNA from Gold Nanoparticles. *J. Phys. Chem. Lett.* **2012**, *3* (7), 902-907.

85. Metwally, K.; Mensah, S.; Baffou, G., Fluence Threshold for Photothermal Bubble Generation Using Plasmonic Nanoparticles. *J. Phys. Chem. C* **2015**, *119* (51), 28586-28596.

86. Wang, J.; Li, Z.; Yao, C. P.; Xue, F.; Zhang, Z. X.; Hüttmann, G., Brownian Diffusion of Gold Nanoparticles in an Optical Trap Studied by Fluorescence Correlation Spectroscopy. *Laser Physics* **2011**, *21* (1), 130-136.

87. Zadeh, J. N.; Steenberg, C. D.; Bois, J. S.; Wolfe, B. R.; Pierce, M. B.; Khan, A. R.; Dirks, R. M.; Pierce, N. A., NUPACK: Analysis and Design of Nucleic Acid Systems. *J. Comput. Chem.* **2011**, *32* (1), 170-173.

88. Chen, C.; Hildebrandt, N., Resonance Energy Transfer to Gold Nanoparticles: NSET defeats FRET. *Trends Analyt. Chem.* **2020**, *123*, 115748.
89. Hildebrandt, N.; Spillmann, C. M.; Algar, W. R.; Pons, T.; Stewart, M. H.; Oh, E.; Susumu, K.; Díaz, S. A.; Delehanty, J. B.; Medintz, I. L., Energy Transfer with Semiconductor Quantum Dot Bioconjugates: A Versatile Platform for Biosensing, Energy Harvesting, and Other Developing Applications. *Chem. Rev.* **2017**, *117* (2), 536-711.
90. Li, M.; Cushing, S. K.; Wang, Q.; Shi, X.; Hornak, L. A.; Hong, Z.; Wu, N., Size-Dependent Energy Transfer between CdSe/ZnS Quantum Dots and Gold Nanoparticles. *J. Phys. Chem. Lett.* **2011**, *2* (17), 2125-2129.
91. Li, H.; Rothberg, L., Colorimetric Detection of DNA Sequences based on Electrostatic Interactions with Unmodified Gold Nanoparticles. *Proc. Natl. Acad. Sci. U.S.A* **2004**, *101* (39), 14036-14039.
92. Zhou, W.; Hu, K.; Kwee, S.; Tang, L.; Wang, Z.; Xia, J.; Li, X., Gold Nanoparticle Aggregation-Induced Quantitative Photothermal Biosensing Using a Thermometer: A Simple and Universal Biosensing Platform. *Anal. Chem.* **2020**, *92* (3), 2739-2747.
93. Demers, L. M.; Mirkin, C. A.; Mucic, R. C.; Reynolds, R. A.; Letsinger, R. L.; Elghanian, R.; Viswanadham, G., A Fluorescence-Based Method for Determining the Surface Coverage and Hybridization Efficiency of Thiol-Capped Oligonucleotides Bound to Gold Thin Films and Nanoparticles. *Anal. Chem.* **2000**, *72* (22), 5535-5541.
94. Chen, C.; Wang, W.; Ge, J.; Zhao, X. S., Kinetics and Thermodynamics of DNA Hybridization on Gold Nanoparticles. *Nucleic Acids Res.* **2009**, *37* (11), 3756-3765.
95. Algar, W. R.; Hildebrandt, N.; Vogel, S. S.; Medintz, I. L., FRET as a Biomolecular Research Tool — Understanding its Potential while Avoiding Pitfalls. *Nature Methods* **2019**, *16* (9), 815-829.
96. Moreira, B. G.; You, Y.; Behlke, M. A.; Owczarzy, R., Effects of Fluorescent Dyes, Quenchers, and Dangling Ends on DNA Duplex Stability. *Biochem. Biophys. Res. Commun.* **2005**, *327* (2), 473-484.
97. Zhou, J.; Ralston, J.; Sedev, R.; Beattie, D. A., Functionalized Gold Nanoparticles: Synthesis, Structure and Colloid Stability. *J. Colloid Interface Sci.* **2009**, *331* (2), 251-262.
98. Fanget, B.; Devos, O.; Draye, M., Correction of Inner Filter Effect in Mirror Coating Cells for Trace Level Fluorescence Measurements. *Analytical Chemistry* **2003**, *75* (11), 2790-2795.

99. Zhang, F.; Wang, S.; Liu, J., Gold Nanoparticles Adsorb DNA and Aptamer Probes Too Strongly and a Comparison with Graphene Oxide for Biosensing. *Anal. Chem.* **2019**, *91* (22), 14743-14750.
100. Baffou, G.; Berto, P.; Bermúdez Ureña, E.; Quidant, R.; Monneret, S.; Polleux, J.; Rigneault, H., Photoinduced Heating of Nanoparticle Arrays. *ACS Nano* **2013**, *7* (8), 6478-6488.
101. Folta-Stogniew, E.; Russu, I. M., Sequence Dependence of Base-Pair Opening in a DNA Dodecamer Containing the CACA/GTGT Sequence Motif. *Biochemistry* **1994**, *33* (36), 11016-11024.
102. Glasstone, S. L. K. J. E. H., *The Theory of Rate Processes The Kinetics of Chemical Reactions, Viscosity, Diffusion and Electrochemical Phenomena*. McGraw-Hill Book Compagny: New York, N.Y., 1941.
103. Baffou, G.; Rigneault, H., Femtosecond-Pulsed Optical Heating of Gold Nanoparticles. *Phys. Rev. B* **2011**, *84* (3), 035415.
104. Breger, J. C.; Oh, E.; Susumu, K.; Klein, W. P.; Walper, S. A.; Ancona, M. G.; Medintz, I. L., Nanoparticle Size Influences Localized Enzymatic Enhancement—A Case Study with Phosphotriesterase. *Bioconjugate Chem.* **2019**, *30* (7), 2060-2074.
105. Oh, E.; Fatemi, F. K.; Currie, M.; Delehanty, J. B.; Pons, T.; Fragola, A.; Lévesque-Fort, S.; Goswami, R.; Susumu, K.; Huston, A. L.; Medintz, I. L., PEGylated Luminescent Gold Nanoclusters: Synthesis, Characterization, Bioconjugation, and Application to One- and Two-Photon Cellular Imaging. *Part. Part. Syst. Char.* **2013**, *30* (5), 453-466.
106. Gemmill, K. B.; Díaz, S. A.; Blanco-Canosa, J. B.; Deschamps, J. R.; Pons, T.; Liu, H.-W.; Deniz, A.; Melinger, J.; Oh, E.; Susumu, K.; Stewart, M. H.; Hastman, D. A.; North, S. H.; Delehanty, J. B.; Dawson, P. E.; Medintz, I. L., Examining the Polyproline Nanoscopic Ruler in the Context of Quantum Dots. *Chemistry of Materials* **2015**, *27* (18), 6222-6237.
107. Alper, J.; Hamad-Schifferli, K., Effect of Ligands on Thermal Dissipation from Gold Nanorods. *Langmuir* **2010**, *26* (6), 3786-3789.
108. Ge, Z.; Cahill, D. G.; Braun, P. V., Thermal Conductance of Hydrophilic and Hydrophobic Interfaces. *Phys. Rev. Lett.* **2006**, *96* (18), 186101.
109. Schmidt, A. J.; Alper, J. D.; Chiesa, M.; Chen, G.; Das, S. K.; Hamad-Schifferli, K., Probing the Gold Nanorod–Ligand–Solvent Interface by Plasmonic Absorption and Thermal Decay. *J. Phys. Chem. C* **2008**, *112* (35), 13320-13323.

110. Bueren-Calabuig, J. A.; Giraudon, C.; Galmarini, C. M.; Egly, J. M.; Gago, F., Temperature-Induced Melting of Double-Stranded DNA in the Absence and Presence of Covalently Bonded Antitumour Drugs: Insight from Molecular Dynamics Simulations. *Nucleic Acids Research* **2011**, *39* (18), 8248-8257.
111. Qamhie, K.; Wong, K.-Y.; Lynch, G. C.; Pettitt, B. M., The Melting Mechanism of DNA Tethered to a Surface. *Int. J. Numer. Anal. Model.* **2009**, *6* (3), 474-488.
112. Wong, K.-Y.; Pettitt, B. M., The Pathway of Oligomeric DNA Melting Investigated by Molecular Dynamics Simulations. *Biophysical Journal* **2008**, *95* (12), 5618-5626.
113. Guo, J.; Qiu, X.; Mingo, C.; Deschamps, J. R.; Susumu, K.; Medintz, I. L.; Hildebrandt, N., Conformational Details of Quantum Dot-DNA Resolved by Förster Resonance Energy Transfer Lifetime Nanoruler. *ACS Nano* **2019**, *13* (1), 505-514.
114. Hastman, D. A.; Melinger, J. S.; Aragonés, G. L.; Cunningham, P. D.; Chiriboga, M.; Salvato, Z. J.; Salvato, T. M.; Brown, C. W.; Mathur, D.; Medintz, I. L.; Oh, E.; Díaz, S. A., Femtosecond Laser Pulse Excitation of DNA-Labeled Gold Nanoparticles: Establishing a Quantitative Local Nanothermometer for Biological Applications. *ACS Nano* **2020**, *14* (7), 8570-8583.
115. Boulais, É.; Lachaine, R.; Meunier, M., Plasma Mediated off-Resonance Plasmonic Enhanced Ultrafast Laser-Induced Nanocavitation. *Nano Letters* **2012**, *12* (9), 4763-4769.
116. Zhang, F.; Wang, S.; Liu, J., Gold Nanoparticles Adsorb DNA and Aptamer Probes Too Strongly and a Comparison with Graphene Oxide for Biosensing. *Analytical Chemistry* **2019**, *91* (22), 14743-14750.
117. Maleki, A.; Alavi, S.; Najafi, B., Molecular Dynamics Simulation Study of Adsorption and Patterning of DNA Bases on the Au(111) Surface. *The Journal of Physical Chemistry C* **2011**, *115* (45), 22484-22494.
118. Alizadehmojarad, A. A.; Zhou, X.; Beyene, A. G.; Chacon, K. E.; Sung, Y.; Pinals, R. L.; Landry, M. P.; Vuković, L., Binding Affinity and Conformational Preferences Influence Kinetic Stability of Short Oligonucleotides on Carbon Nanotubes. *Advanced Materials Interfaces* **2020**, *7* (15), 2000353.
119. Kelich, P.; Asadinezhad, A., Molecular Simulation Study on Brushes of Poly (2-ethyl-2-oxazoline). *Materials Today Communications* **2019**, *21*, 100681.
120. Nißler, R.; Mann, F. A.; Chaturvedi, P.; Horlebein, J.; Meyer, D.; Vuković, L.; Kruss, S., Quantification of the Number of Adsorbed DNA Molecules on Single-Walled Carbon Nanotubes. *The Journal of Physical Chemistry C* **2019**, *123* (8), 4837-



4847.

121. Izanloo, C., Effect of Gold Nanoparticle on Stability of the DNA Molecule: A Study of Molecular Dynamics Simulation. *Nucleosides, Nucleotides & Nucleic Acids* **2017**, *36* (9), 571-582.

122. Lee, O.-S.; Schatz, G. C., Molecular Dynamics Simulation of DNA-Functionalized Gold Nanoparticles. *The Journal of Physical Chemistry C* **2009**, *113* (6), 2316-2321.

123. Oh, E.; Fatemi, F. K.; Currie, M.; Delehanty, J. B.; Pons, T.; Fragola, A.; L  v  que-Fort, S.; Goswami, R.; Susumu, K.; Huston, A. L.; Medintz, I. L., PEGylated Luminescent Gold Nanoclusters: Synthesis, Characterization, Bioconjugation, and Application to One- and Two-Photon Cellular Imaging. *Particle & Particle Systems Characterization* **2013**, *30* (5), 453-466.

124. Ge, Z.; Cahill, D. G.; Braun, P. V., Thermal Conductance of Hydrophilic and Hydrophobic Interfaces. *Physical Review Letters* **2006**, *96* (18), 186101.

125. Schmidt, A. J.; Alper, J. D.; Chiesa, M.; Chen, G.; Das, S. K.; Hamad-Schifferli, K., Probing the Gold Nanorod–Ligand–Solvent Interface by Plasmonic Absorption and Thermal Decay. *The Journal of Physical Chemistry C* **2008**, *112* (35), 13320-13323.

126. Ding, S.; Cargill, A. A.; Medintz, I. L.; Claussen, J. C., Increasing the Activity of Immobilized Enzymes with Nanoparticle Conjugation. *Current Opinion in Biotechnology* **2015**, *34*, 242-250.

127. Vranish, J. N.; Ancona, M. G.; Walper, S. A.; Medintz, I. L., Pursuing the Promise of Enzymatic Enhancement with Nanoparticle Assemblies. *Langmuir* **2018**, *34* (9), 2901-2925.

128. Blankschien, M. D.; Pretzer, L. A.; Huschka, R.; Halas, N. J.; Gonzalez, R.; Wong, M. S., Light-Triggered Biocatalysis Using Thermophilic Enzyme–Gold Nanoparticle Complexes. *ACS Nano* **2013**, *7* (1), 654-663.

129. de Barros, H. R.; Garc  a, I.; Kuttner, C.; Zeballos, N.; Camargo, P. H. C.; de Torresi, S. I. C.; L  pez-Gallego, F.; Liz-Marz  n, L. M., Mechanistic Insights into the Light-Driven Catalysis of an Immobilized Lipase on Plasmonic Nanomaterials. *ACS Catalysis* **2021**, *11* (1), 414-423.

130. Tadepalli, S.; Yim, J.; Cao, S.; Wang, Z.; Naik, R. R.; Singamaneni, S., Metal–Organic Framework Encapsulation for the Preservation and Photothermal Enhancement of Enzyme Activity. *Small* **2018**, *14* (7), 1702382.

131. Tadepalli, S.; Yim, J.; Madireddi, K.; Luan, J.; Naik, R. R.; Singamaneni, S., Gold Nanorod-Mediated Photothermal Enhancement of the Biocatalytic Activity of a

Polymer-Encapsulated Enzyme. *Chemistry of Materials* **2017**, 29 (15), 6308-6314.

132. Claussen, J. C.; Malanoski, A.; Breger, J. C.; Oh, E.; Walper, S. A.; Susumu, K.; Goswami, R.; Deschamps, J. R.; Medintz, I. L., Probing the Enzymatic Activity of Alkaline Phosphatase within Quantum Dot Bioconjugates. *The Journal of Physical Chemistry C* **2015**, 119 (4), 2208-2221.

133. Fadiloğlu, S.; Erkmen, O.; Şekeroğlu, G., Thermal Inactivation Kinetics of Alkaline Phosphatase in Buffer and Milk. *Journal of Food Processing and Preservation* **2006**, 30 (3), 258-268.

134. Díaz, S. A.; Choo, P.; Oh, E.; Susumu, K.; Klein, W. P.; Walper, S. A.; Hastman, D. A.; Odom, T. W.; Medintz, I. L., Gold Nanoparticle Templating Increases the Catalytic Rate of an Amylase, Maltase, and Glucokinase Multienzyme Cascade through Substrate Channeling Independent of Surface Curvature. *ACS Catalysis* **2020**, 627-638.

135. Puente, X. S.; Sánchez, L. M.; Overall, C. M.; López-Otín, C., Human and Mouse Proteases: A Comparative Genomic Approach. *Nature Reviews Genetics* **2003**, 4 (7), 544-58.

136. Arcus, V. L.; van der Kamp, M. W.; Pudney, C. R.; Mulholland, A. J., Enzyme Evolution and the Temperature Dependence of Enzyme Catalysis. *Current Opinion in Structural Biology* **2020**, 65, 96-101.

137. Hyrup, B.; Nielsen, P. E., Peptide Nucleic Acids (PNA): Synthesis, Properties and Potential Applications. *Bioorg. Med. Chem.* **1996**, 4 (1), 5-23.

138. Nielsen, P. E.; Egholm, M.; Buchardt, O., Peptide nucleic acid (PNA). A DNA Mimic with a Peptide Backbone. *Bioconj. Chem.* **1994**, 5 (1), 3-7.

139. Wittung, P.; Nielsen, P.; Nordén, B., Direct Observation of Strand Invasion by Peptide Nucleic Acid (PNA) into Double-Stranded DNA. *J. Am. Chem. Soc.* **1996**, 118 (30), 7049-7054.

140. Uhlmann, E.; Peyman, A.; Breipohl, G.; Will, D. W., PNA: Synthetic Polyamide Nucleic Acids with Unusual Binding Properties. *Angew. Chem. Int. Ed.* **1998**, 37 (20), 2796-2823.

141. Yamazaki, T.; Aiba, Y.; Yasuda, K.; Sakai, Y.; Yamanaka, Y.; Kuzuya, A.; Ohya, Y.; Komiyama, M., Clear-cut Observation of PNA Invasion Using Nanomechanical DNA Origami Devices. *Chem. Commun.* **2012**, 48 (92), 11361-11363.

142. Zhan, Y.; Zocchi, G., Flexibility of DNA/PNA, DNA/LNA, DNA/RNA Hybrids Measured with a Nanoscale Transducer. *EPL (Europhysics Letters)* **2017**, 119 (4),

48005.

143. Pedersen, R. O.; Kong, J.; Achim, C.; LaBean, T. H., Comparative Incorporation of PNA into DNA Nanostructures. *Molecules* **2015**, *20* (9), 17645-58.

144. Berger, O.; Gazit, E., Molecular Self-Assembly using Peptide Nucleic Acids. *Biopolymers* **2017**, *108* (1).

145. Flory, J. D.; Shinde, S.; Lin, S.; Liu, Y.; Yan, H.; Ghirlanda, G.; Fromme, P., PNA-Peptide Assembly in a 3D DNA Nanocage at Room Temperature. *J. Am. Chem. Soc.* **2013**, *135* (18), 6985-6993.

146. Veneziano, R.; Moyer, T. J.; Stone, M. B.; Wamhoff, E.-C.; Read, B. J.; Mukherjee, S.; Shepherd, T. R.; Das, J.; Schief, W. R.; Irvine, D. J., Role of Nanoscale Antigen Organization on B-cell Activation Probed using DNA Origami. *Nature Nanotechnology* **2020**, *15* (8), 716-723.

147. Bush, J.; Singh, S.; Vargas, M.; Oktay, E.; Hu, C. H.; Veneziano, R., Synthesis of DNA Origami Scaffolds: Current and Emerging Strategies. *Molecules* **2020**, *25* (15).

148. Ke, Y.; Ong, L. L.; Shih, W. M.; Yin, P., Three-Dimensional Structures Self-Assembled from DNA Bricks. *Science* **2012**, *338* (6111), 1177-1183.

149. Ong, L. L.; Hanikel, N.; Yaghi, O. K.; Grun, C.; Strauss, M. T.; Bron, P.; Lai-Kee-Him, J.; Schueder, F.; Wang, B.; Wang, P., Programmable Self-Assembly of Three-Dimensional Nanostructures from 10,000 Unique Components. *Nature* **2017**, *552* (7683), 72-77.

150. Green, C. M.; Mathur, D.; Medintz, I. L., Understanding the Fate of DNA Nanostructures Inside the Cell. *Journal of Materials Chemistry B* **2020**, *8* (29), 6170-6178.

151. Kownacki, M.; Langenegger, S. M.; Liu, S.-X.; Häner, R., Integrating DNA Photonic Wires into Light-Harvesting Supramolecular Polymers. *Angew. Chem. Int. Ed.* **2019**, *58* (3), 751-755.

152. Bayrak, T.; Jagtap, N. S.; Erbe, A., Review of the Electrical Characterization of Metallic Nanowires on DNA Templates. *Int. J. Mol. Sci.* **2018**, *19* (10).

153. Li, N.; Shang, Y.; Xu, R.; Jiang, Q.; Liu, J.; Wang, L.; Cheng, Z.; Ding, B., Precise Organization of Metal and Metal Oxide Nanoclusters into Arbitrary Patterns on DNA Origami. *J. Am. Chem. Soc.* **2019**, *141* (45), 17968-17972.

154. Zhao, Y.; Dai, X.; Wang, F.; Zhang, X.; Fan, C.; Liu, X., Nanofabrication Based on DNA Nanotechnology. *Nano Today* **2019**, *26*, 123-148.
155. Meyer, T. A.; Zhang, C.; Bao, G.; Ke, Y., Programmable Assembly of Iron Oxide Nanoparticles Using DNA Origami. *Nano Lett.* **2020**, *20* (4), 2799-2805.
156. Bui, H.; Onodera, C.; Kidwell, C.; Tan, Y.; Graugnard, E.; Kuang, W.; Lee, J.; Knowlton, W. B.; Yurke, B.; Hughes, W. L., Programmable Periodicity of Quantum Dot Arrays with DNA Origami Nanotubes. *Nano Lett.* **2010**, *10* (9), 3367-72.
157. Maune, H. T.; Han, S.-p.; Barish, R. D.; Bockrath, M.; Goddard III, W. A.; Rothmund, P. W.; Winfree, E., Self-Assembly of Carbon Nanotubes into Two-Dimensional Geometries using DNA Origami Templates. *Nature Nanotechnology* **2010**, *5* (1), 61-66.
158. Samanta, D.; Iscen, A.; Laramy, C. R.; Ebrahimi, S. B.; Bujold, K. E.; Schatz, G. C.; Mirkin, C. A., Multivalent Cation-Induced Actuation of DNA-Mediated Colloidal Superlattices. *J. Am. Chem. Soc.* **2019**, *141* (51), 19973-19977.
159. Jin, R.; Zeng, C.; Zhou, M.; Chen, Y., Atomically Precise Colloidal Metal Nanoclusters and Nanoparticles: Fundamentals and Opportunities. *Chem. Rev.* **2016**, *116* (18), 10346-10413.
160. Jimenez-Ruiz, A.; Perez-Tejeda, P.; Grueso, E.; Castillo, P. M.; Prado-Gotor, R., Nonfunctionalized Gold Nanoparticles: Synthetic Routes and Synthesis Condition Dependence. *Chemistry—A European Journal* **2015**, *21* (27), 9596-9609.
161. Díaz, S. A.; Lasarte Aragonés, G.; Buckhout-White, S.; Qiu, X.; Oh, E.; Susumu, K.; Melinger, J. S.; Huston, A. L.; Hildebrandt, N.; Medintz, I. L., Bridging Lanthanide to Quantum Dot Energy Transfer with a Short-Lifetime Organic Dye. *The Journal of Physical Chemistry Letters* **2017**, *8* (10), 2182-2188.
162. Mathur, D.; Samanta, A.; Oh, E.; Díaz, S. A.; Susumu, K.; Ancona, M. G.; Medintz, I. L., Quantum Dot Encapsulation Using a Peptide-Modified Tetrahedral DNA Cage. *Chem. Mater.* **2017**, *29* (14), 5762-5766.
163. Samanta, A.; Deng, Z.; Liu, Y.; Yan, H., A Perspective on Functionalizing Colloidal Quantum Dots with DNA. *Nano Research* **2013**, *6* (12), 853-870.
164. Susumu, K.; Oh, E.; Delehanty, J. B.; Blanco-Canosa, J. B.; Johnson, B. J.; Jain, V.; Hervey IV, W. J.; Algar, W. R.; Boeneman, K.; Dawson, P. E., Multifunctional Compact Zwitterionic Ligands for Preparing Robust Biocompatible Semiconductor Quantum Dots and Gold Nanoparticles. *J. Am. Chem. Soc.* **2011**, *133* (24), 9480-9496.

165. Díaz, S. A.; Sen, S.; Boeneman Gemmill, K.; Brown, C. W.; Oh, E.; Susumu, K.; Stewart, M. H.; Breger, J. C.; Lasarte Aragonés, G.; Field, L. D.; Deschamps, J. R.; Král, P.; Medintz, I. L., Elucidating Surface Ligand-Dependent Kinetic Enhancement of Proteolytic Activity at Surface-Modified Quantum Dots. *ACS Nano* **2017**, *11* (6), 5884-5896.
166. Rothmund, P. W., Folding DNA to Create Nanoscale Shapes and Patterns. *Nature* **2006**, *440* (7082), 297-302.
167. Aghebat Rafat, A.; Pirzer, T.; Scheible, M. B.; Kostina, A.; Simmel, F. C., Surface-Assisted Large-Scale Ordering of DNA Origami Tiles. *Angew. Chem. Int. Ed.* **2014**, *53* (29), 7665-7668.
168. Strauss, M. T.; Schueder, F.; Haas, D.; Nickels, P. C.; Jungmann, R., Quantifying Absolute Addressability in DNA Origami with Molecular Resolution. *Nature Communications* **2018**, *9* (1), 1-7.
169. Green, C. M.; Hastman, D. A.; Mathur, D.; Susumu, K.; Oh, E.; Medintz, I. L.; Díaz, S. A., Direct and Efficient Conjugation of Quantum Dots to DNA Nanostructures with Peptide-PNA. *ACS Nano* **2021**, *15* (5), 9101-9110.
170. Stahl, E.; Martin, T. G.; Praetorius, F.; Dietz, H., Facile and Scalable Preparation of Pure and Dense DNA Origami Solutions. *Angew. Chem. Int. Ed.* **2014**, *53* (47), 12735-12740.
171. Gonzalez Solveyra, E.; Szleifer, I., What is the Role of Curvature on the Properties of Nanomaterials for Biomedical Applications? *Wiley Interdisciplinary Reviews: Nanomedicine and Nanobiotechnology* **2016**, *8* (3), 334-354.
172. Dennis, A. M.; Delehanty, J. B.; Medintz, I. L., Emerging Physicochemical Phenomena along with New Opportunities at the Biomolecular–Nanoparticle Interface. *The Journal of Physical Chemistry Letters* **2016**, *7* (11), 2139-2150.
173. Ellis, G. A.; Dean, S. N.; Walper, S. A.; Medintz, I. L., Quantum Dots and Gold Nanoparticles as Scaffolds for Enzymatic Enhancement: Recent Advances and the Influence of Nanoparticle Size. *Catalysts* **2020**, *10* (1), 83.
174. Palomo, V.; Díaz, S. A.; Stewart, M. H.; Susumu, K.; Medintz, I. L.; Dawson, P. E., 3, 4-Dihydroxyphenylalanine Peptides as Nonperturbative Quantum Dot Sensors of Aminopeptidase. *ACS Nano* **2016**, *10* (6), 6090-6099.
175. Breger, J. C.; Susumu, K.; Lasarte-Aragonés, G.; Díaz, S. A.; Brask, J.; Medintz, I. L., Quantum Dot Lipase Biosensor Utilizing a Custom-Synthesized Peptidyl-Ester Substrate. *ACS Sensors* **2020**, *5* (5), 1295-1304.
176. Saarbach, J.; Sabale, P. M.; Winssinger, N., Peptide Nucleic Acid (PNA) and its Applications in Chemical Biology, Diagnostics, and Therapeutics. *Curr. Opin. Chem.*

*Biol.* **2019**, *52*, 112-124.

177. Karkare, S.; Bhatnagar, D., Promising Nucleic Acid Analogs and Mimics: Characteristic Features and Applications of PNA, LNA, and Morpholino. *Appl. Microbiol. Biotechnol.* **2006**, *71* (5), 575-586.

178. Stahl, E.; Martin, T. G.; Praetorius, F.; Dietz, H., Facile and Scalable Preparation of Pure and Dense DNA Origami Solutions. *Angewandte Chemie* **2014**, *126* (47), 12949-12954.